

---

# Guided Matter-Wave Interferometry

---

*Author:*  
Saurabh Pandey

*Thesis Supervisors:*  
Wolf von Klitzing  
Dimitris Papazolgou  
Pavlos Savvidis

Department of Materials Science and Technology  
University of Crete

IESL-FORTH

July 24, 2019





*“Love is a better teacher than a sense of duty.”*

*“I am enough of the artist to draw freely upon my imagination. Imagination is more important than knowledge. Knowledge is limited. Imagination encircles the world.”*

Albert Einstein



## *Acknowledgements*

It is very hard to find words to express my feelings of gratitude towards Wolf von Klitzing, my thesis supervisor. If I may list some, his enormous patience, the freedom he gives to learn and explore, immense knowledge, and his anytime (even 2 am) availability to students, are some of his traits which left me astonished. He did not only open my eyes to see the physics but taught lessons which made me a better person, hopefully for the rest of my life. Here is one of his quotes, *data talks and frequency rocks*, which tells one should really try to know what to look at and think discrete. I can not imagine a better supervisor, mentor, lab, and place (the Crete) for my PhD.

I would like to thank Dimitris Papazoglou, without you I could not have started my PhD. I will not forget your support to get me enrolled in the department. Your guidance throughout this journey has made me able to reach this point.

A heartfelt thanks to Hector Mas, with whom I spent almost a life in the laboratory, worked and grew up together, and had great fun listening his everyday lunch stories, e.g., why to kill all the cats.

Georgios Vasilakis, postdoc on the experiment, thank you for giving a deep insight on several topics, and teaching how to teach. Thanks to Giannis Drougakis for taking over the experiment, fun we had, and allowing me to have extreme fun in your graduation ceremony.

I want to thank other and past postdocs of the Cretan Matter Waves lab, Vasiliki Bolapsi, Kostas Poullos, and Ivan Alonso, for their encouragement and help. I enjoyed very much working late at night with Ivan (though he was in a different experiment).

The arrival of Premjith Thekkepatt to the lab was fun, had exciting discussions (only physics) over a lot of coffee.

Prabhat Tripathi, a friend from undergraduate days, I thank you for being a friend and giving strength at low times in this journey. Udbhav Ojha, a senior and friend from IIT Dhanbad, thanks for all the help and guidance from the day

one I stepped into the college.

Love and big thanks to my parents, Vinod Kumar Pandey and Manju Pandey, who right from my school days have given me the freedom, courage, and unconditional support to do what I really liked.



## Abstract

Coherent guiding and manipulation of matter-waves is of utmost importance in the development of practical atomtronic sensors and devices. In this thesis, I present excitationless guiding of Bose-Einstein condensates (BECs) at hypersonic speeds in magnetic time-averaged adiabatic potential (TAAP) rings traps and waveguides. For the first time, matter-waves are transported for a record distance of 40 cm at hypersonic speeds without detecting any extra excitation when compared to the static case. To realize a rotation sensor utilizing the clock transition of Rubidium 87 ( $^{87}\text{Rb}$ ), I present trapping and manipulation of the spin states of  $^{87}\text{Rb}$ , in two arms of a ring trap. The extreme smoothness of TAAP rings is demonstrated via the propagation of BECs in the ring waveguide, measured smoothness is below 200 pK. In a different interferometer configuration, using optical beam splitters and guided matter-waves in a horizontal ring waveguide, I implemented delta-kick cooling technique to achieve compact atomic wave-packet guiding for seconds. The one-dimensional effective BEC temperature is lowered by a factor of 30, down to a few nanoKelvin. These demonstrations now provide a platform to realize highly sensitive, compact atomic rotation sensors, and investigate fundamental questions, e.g., superfluidity of BECs much above their critical velocity.





## List of publications

### Included in this thesis

1. **S Pandey**, H Mas, G Drougakis, P Thekkeppatt, v Bolpasi, G Vasilakis, K Poullos, and W von Klitzing, Hypersonic Bose-Einstein Condensates in Accelerator Rings, *Nature* 570, 205-209 (2019).
2. **S Pandey**, H Mas, G Vasilakis, and W von Klitzing, Atom Optics with Bose-Einstein Condensates in Ring-Shaped Waveguides, in preparation (2019).
3. **S Pandey**, W von Klitzing, Precision Calibration of Time Orbiting Potential traps, in preparation (2019).
4. P Navez, **S Pandey**, H Mas, K Poullos, T Fernholz and W von Klitzing, Matter-wave Interferometers using TAAP Rings, *New J. Phys.* 18 075014 (2016).
5. T Fernholz, R Stevenson, M R Hush, I W Lesanovsky, T Bishop, F Gentile, S Jammi, T Pyragius, M G Bason, H Mas, **S Pandey**, G Vasilakis, K Poullos and W von Klitzing, Towards rotation sensing with a single atomic clock, *Proc. of SPIE Vol. 9900 990007-1* (2016).

### Additional publications

6. G A Sinuco-Leon, B M Garraway, H Mas, **S Pandey**, G Vasilakis, V Bolpasi, W von Klitzing, B Foxon, S. Jammi, K. Poullos, and T Fernholz, Microwave spectroscopy of radio-frequency dressed  $^{87}\text{Rb}$ , submitted to *Phys. Rev. A*, arXiv:1904.12073v1, <https://arxiv.org/abs/1904.12073> (2019).
7. H Mas, **S Pandey**, G Vasilakis, and W von Klitzing, Bi-chromatic adiabatic potentials for atom interferometry, in preparation (2019).
8. I Drougakis, K G Mavrakis, **S Pandey**, G Vasilakis, K Poullos, D G Papazoglou, and W von Klitzing, Precise and robust optical beam steering for space optical instrumentation, submitted to *CEAS Space Journal* (2019).

9. **S Pandey**, H Mas, G Drougakis, K G Mavrakis, M Mylonakis, G Vasilakis, V Bolpasi, and W von Klitzing, Antireflection Coated Semiconductor Laser Amplifier for Bose-Einstein Condensation Experiments, *AIP Advances* 8, 095020 (2018).
10. M Mylonakis, **S Pandey**, K G Mavrakis, G Drougakis, G Vasilakis, D G Papazoglou, and W von Klitzing, Simple Precision Measurements of Optical Beam Sizes, *Appl. Opt.*, 57 (33), 9863-9867 (2018).



# Contents

<b>1</b>	<b>Introduction</b>	<b>1</b>
1.1	Wave particle duality . . . . .	1
1.2	Cooling and trapping of neutral atoms . . . . .	2
1.3	Birth of Bose-Einstein condensate . . . . .	4
1.4	This thesis . . . . .	6
<b>2</b>	<b>Theory</b>	<b>10</b>
2.1	Magneto-optical trap . . . . .	10
2.1.1	Laser cooling . . . . .	11
2.1.2	Magnetic trapping . . . . .	14
2.1.3	A combination: magneto-optical trap . . . . .	17
2.2	A hybrid trap – dipole plus magnetic . . . . .	19
2.3	Magnetic traps of this thesis . . . . .	22
2.3.1	Time-orbiting potential trap . . . . .	22
2.3.2	RF dressed adiabatic potentials . . . . .	25
2.3.3	TAAP rings . . . . .	28
2.4	Bose-Einstein condensation . . . . .	31
<b>3</b>	<b>Experimental Setup</b>	<b>35</b>

3.1	Lasers . . . . .	35
3.1.1	Injection-locked slave laser . . . . .	35
3.1.2	AOM distribution board . . . . .	36
3.1.3	Tapered amplifier . . . . .	38
3.1.4	MOT setup . . . . .	39
	2D-MOT . . . . .	40
	3D-MOT . . . . .	41
3.2	Coils for the magnetic trapping . . . . .	41
3.2.1	Quadrupole coils . . . . .	41
3.2.2	Modulation field coils . . . . .	42
3.2.3	RF generation . . . . .	43
3.2.4	Compensation coils . . . . .	45
3.3	Optical dipole trap . . . . .	46
3.3.1	Setup . . . . .	46
3.3.2	Dipole beams alignment and characterization . . . . .	47
3.3.3	Dipole laser safety interlock . . . . .	50
3.4	Imaging system . . . . .	53
<b>4</b>	<b>BEC production</b>	<b>55</b>
4.1	TOP trap . . . . .	55
4.1.1	Trap characterization . . . . .	56
4.1.2	BEC production . . . . .	59
4.2	Crossed dipole trap . . . . .	60
4.2.1	Sequence optimization . . . . .	61

4.2.2	BEC production . . . . .	62
	BEC number stability . . . . .	65
<b>5</b>	<b>Ring trap loading, characterization, and arbitrary traps</b>	<b>66</b>
5.1	Ring loading results . . . . .	67
5.2	Ring trap characterization . . . . .	69
5.2.1	Trapping frequencies . . . . .	69
5.2.2	Ring waveguide radius . . . . .	70
5.2.3	Lifetime and heating rate . . . . .	74
5.3	Flattening the ring waveguide . . . . .	75
5.4	Arbitrary ring traps . . . . .	76
5.4.1	State-insensitive: modulation tilt . . . . .	77
5.4.2	State-sensitive: rf polarization tilt . . . . .	77
5.4.3	Simultaneous independent traps for two spin states . . . . .	78
<b>6</b>	<b>Acceleration and hypersonic transport of BECs</b>	<b>80</b>
6.1	Bang-bang control . . . . .	80
6.2	BEC acceleration . . . . .	82
6.2.1	Waveguide deformation due to the angular motion . . . . .	82
6.3	Hypersonic transport of trapped BECs . . . . .	84
6.3.1	Phase jump optimization . . . . .	84
6.3.2	Transport Results . . . . .	84
6.3.3	The term <i>hypersonic</i> . . . . .	86
6.3.4	Micromotion of BECs . . . . .	87

6.3.5	Lifetime measurements . . . . .	88
6.3.6	Heating rate measurements . . . . .	89
6.3.7	Shape oscillations . . . . .	90
6.3.8	Ring radius . . . . .	92
6.4	Ring flatness with circulating atoms . . . . .	92
6.5	The radius of circulating atoms in ToF . . . . .	94
<b>7</b>	<b>Atom optics in the ring waveguide</b>	<b>96</b>
7.1	BEC launch into the ring waveguide . . . . .	97
7.2	The azimuthal lens . . . . .	98
7.3	Experimental sequence . . . . .	100
7.4	Atom optics with ultracold thermal atoms . . . . .	100
7.5	Atom optics with Bose-condensed atoms . . . . .	101
7.5.1	Collimation of the guided matterwaves . . . . .	101
7.5.2	Focusing the guided matterwaves . . . . .	103
	Angular speed after the lens . . . . .	105
7.6	A beam splitter for BECs in the ring waveguide . . . . .	105
<b>8</b>	<b>Conclusions and future work</b>	<b>108</b>



# Chapter 1

## Introduction

### 1.1 Wave particle duality

In 1801, Thomas Young performed an experiment in which sunlight passing through two narrow slits produced an interference pattern onto a screen behind. This was the first demonstration which showed that light behaves like a wave. In the late 19th century, Hertz observed that a charged body loses more easily its charge when illuminated by light. This experiment showed, for the first time, that light can push or eject electrons from a material when its frequency is above a certain threshold value, called photoelectric effect. Einstein's explanation of the photoelectric effect, in 1905, started the journey of quantum mechanics. Nearly after a century of belief that light behaves like a wave, the particle nature of light was established by the fact that it is composed of multiples of light particle, called photons, together with the Planck's postulate that energy of the electromagnetic radiation is quantized. The extension of wave mechanics to matter was done by Louis de Broglie. He made a hypothesis that every moving particle also has a wave-like nature. He proposed that the wavelength associated with a particle is,  $\lambda = h/p$ , where  $h$  is Planck's constant and  $p$  its momentum. Since  $h$  is a very small number, about  $6 \times 10^{-34}$ , for the quantum wavelength of objects to become macroscopic either the mass or velocity has to become extremely small.

Wave-particle duality is at the very heart of quantum mechanics. It means that every particle has a wave nature and vice versa. In our daily life, we see objects whose motion can be well described using the classical physics equations, and they move in a well define trajectory. However, in the quantum

world, waves/particles do not just move in a particular direction but their position and momentum has some uncertainty. In other words, waves (matter waves) are not well localized in space unlike massive objects, and they whizz all around us. At first, it is rather difficult to embrace but the theory has successfully passed all the checks so far. In order to test the quantum-ness of matter, many experiments have successfully shown wave-like nature of particles, e.g., electrons, neutrons, atoms and even heavy molecules these days. The wave nature of these particles are demonstrated via the key wave phenomena such as diffraction and interference.

Atoms are highly suitable objects to study the wave-nature of matter, because they are universal and have a well-defined level structure which can be used for their manipulation with light. Neutral atoms can now be cooled down to extremely low temperatures using lasers and magnetic fields reaching the picoKelvin regime. At such low temperatures close to absolute zero, wave-like character of atoms are hugely enhanced with their de Broglie wavelength becoming of the order of micrometers. These macroscopic atomic matter waves are now routinely prepared, manipulated, and observed in tabletop experiments. In the sections below, I give a brief history of the cooling and trapping of neutral atoms, first observation of Bose-Einstein condensate in dilute atomic gases, and the relevance of this thesis to quantum metrology.

## 1.2 Cooling and trapping of neutral atoms

The idea that light can exert pressure on an object was first speculated by Kepler, in the 17th century, that it is the solar radiation due to which the comet tails are aligned away from the light source. Frisch, in 1933[1], showed for the first time that radiation pressure can have significant effect onto the atoms, a collimated Na atomic beam was deflected from its path in the presence of resonant light. The mechanical effect of light was considered to be very small and did not attract much attention, mainly due to the broad spectrum of then available light sources. This was changed by the invention of lasers which brought the motivation that an intense, directional, and narrow linewidth light beam can be used to address strong optical atomic transitions. The idea of radiation pressure to trap and manipulate micron-sized particles, using a

focused laser beam, was first implemented by Ashkin, in 1970 [2]. At the same time, he also suggested that scattering force exerted onto the atoms by an intense monochromatic light beam can be used for the isotope separation, velocity analysis and atom trapping [3].

In 1975, Hansch and Schawlow [4] first proposed that the radiation pressure can be used to reduce the kinetic energy of atoms, i.e., laser cooling. The idea behind the laser cooling is simply the conservation of energy and momentum while the atoms interact with resonant laser beams. It was the first suggestion for the cooling of atoms using laser beams whose frequency is set slightly below the atomic resonance – compensation for the Doppler shift. Ashkin, in 1978 [5], extended his proposal of microparticle trapping to cooling and trapping of atoms by using a resonant tightly focused laser beam. In the beginning, these experiments were done with Na atoms because of its clean level structure, then available suitable wavelength dye lasers and the easy production of thermal Na atomic beams. The first report on the cooling of atoms was by Phillips and Metcalf, in 1982 [6]. A two counter-propagating resonant laser beams together with a spatially varying magnetic field lowered the atomic velocities by about 40%. The varying Zeeman shift compensated for the Doppler shift as the atomic velocity reduced by the continuous absorption-emission of photons. The limiting factor for the temperature achieved in this experiment was the small value of the magnetic gradient in the central region of the deceleration path.

After a few years, in 1985, the experiment by Chu and colleagues [7] demonstrated the first three-dimensional (3D) cooling and pseudo confinement of Na atoms. They used three pairs of mutually orthogonal counter-propagating red-detuned laser beams to cool Na atoms down to  $240 \mu\text{K}$ , named it *optical molasses*. There was no use of magnetic field to keep the atoms resonant with the light but the frequency of the laser was swept as the atomic velocity reduced. The reported temperature,  $240 \mu\text{K}$ , was in agreement with the Doppler cooling limit. This temperature was measured by monitoring the atomic fluorescence after a variable switch off time of the laser beams. Another landmark observation, in 1988, was by Lett and colleagues [8] where they measured temperature of Na atom cloud in an optical molasses to be less than the Doppler limit, about  $40 \mu\text{K}$ . This time the temperature was measured by releasing the atoms from the molasses and looking at the ballistic expansion, and verified via

four independent methods. The measured sub-Doppler temperature brought a huge surprise to the community and later explained that it is due to the spatial variation in polarization of the light field interacting with multilevel atoms. The phenomenon was called *polarization gradient cooling* or *Sisyphus cooling* [9].

In all the experiments above, there was no spatial confinement of neutral atoms shown and mainly the momentum spread manipulation. Theoretical studies related to the neutral atom trapping using magnetic fields started in the 1960's, by Heer and others [10]. The basic idea behind the magnetic trapping was the interaction of atomic magnetic dipole moment with a spatially varying magnetic field having a minimum. The main obstacle in trapping atoms with magnetic field was the high temperature of then prepared cold atoms or the low magnetic trap depth. After the remarkable development of laser cooling technique, atomic samples were prepared having temperatures of the order of magnetic trap depth. The first report on the neutral atom magnetic trapping came in 1985, by Migdall and others [11], a decelerating Na atomic beam was stopped and atoms were captured in a magnetic quadrupole trap. A problem still existed in achieving high energy depth traps and atoms went out of resonance as their velocity reduced near the center of optical molasses.

A very important step in the field of cold atoms was the merge of optical molasses and magnetic trapping scheme, resulted in a trap which could both cool and trap atoms. This idea was first suggested by Jean Dalibard. In 1987, Raab and others [12], demonstrated the first magneto-optical trap (MOT) which used six laser beams along all the Cartesian axes and a magnetic quadrupole field. The reported trap depth was 0.4 K, atomic density reached up to  $10^{-11}$  atoms  $cm^{-3}$ , and atoms were stored for as long as two minutes. From here on, other cooling techniques were developed, such as forced evaporation, to achieve higher phase space densities which finally led to the discovery of Bose-Einstein condensate (BEC). Below, I give a short overview of the journey towards the groundbreaking realization of BEC in dilute atomic gases.

### 1.3 Birth of Bose-Einstein condensate

The aim behind increasing the phase space density in atomic gases was to reach the state of quantum degeneracy. To do that, two things were needed, lower

temperatures and higher atomic densities. It is when the mean separation between the particles becomes of the order of their de Broglie wavelength, phase space density approaches unity or higher and quantum degeneracy is achieved. In this regime, all the atoms occupy the lowest energy state of the system, and they begin to move in unison resulting in a giant quantum wave. In the experiments mentioned so far, the use of near-resonant laser beams did not allow for the cooling of atoms below a certain threshold and the subsequent absorption of the rescattered photons gave an upper limit on the density. In 1993, Ketterle and others [13] reported almost an order improvement in the atomic density by trapping atoms in a dark magneto-optical trap. However, still the presence of near-resonant light did not allow to go further up in the phase space density, of the order of  $10^{-4}$  in a dark MOT. An alternative approach was to switch off all the resonant laser beams and transfer a cold dense atom cloud into a magnetic or far-detuned optical trap. Further, the use of established forced evaporative cooling technique (in the case of spin-polarized hydrogen [14]) advanced the field dramatically.

The implementation of neutral atom magnetic trapping was already demonstrated in 1985 [11]. A quadrupole magnetic trap has zero field amplitude at the center and as a result atoms transit to other spin states and become untrapped or antitrapped as they pass through the center, called Majorana spin flip loss. Since colder atoms reside near the trap center and have higher probability of leaving the trap, this loss mechanism turned out to be detrimental. To circumvent the issue, new trapping schemes were proposed and implemented based on the magnetic and optical dipole force. The first one, called time orbiting potential (TOP) trap, the magnetic zero was displaced away from the atoms and rotated in a circle [15] by using a rotating bias field. The amplitude of this bias field was set such that the zero field trajectory is outside the cloud. The rotation frequency was set slow compared to the Larmor frequency such that the spins remain polarized, and fast compared to the eventual trapping frequency. Due to the time-averaging, the scheme results in a harmonic trap. Radio-frequency (rf) induced forced evaporation in this trap resulted in the first observation of BEC [16]. A different scheme, using both the magnetic and optical force was an optical plug, i.e., far blue-detuned laser beam aligned at the center of the magnetic quadrupole. By the use of rf evaporation, BEC was realized in this hybrid magnetic-optical trap [17].

## 1.4 This thesis

Atomtronics is a sub-field of ultracold atomic physics with the aim to realize sensors and devices with neutral atoms, analogous to electrons in an electronic circuit. The major directions in cold and ultracold atomic systems are the study of superfluidity in BEC [18], quantum simulation and computation [19], atom interferometry [20], and atomic clocks [21, 22]. One of the important configuration is an atom interferometer [23, 24], applications include observation of inertial effects [25, 26], geophysical measurements [27], and fundamental studies [28, 29, 30, 31, 32]. Ultra-cold atoms have been used to devise and perform electronic equivalent operations such as battery [33, 34], transistor [35] and an atomtronic SQUID [36, 37]. An essential requirement for the optimal performance of atom circuits is the coherent and dynamic manipulation of matterwaves. Dipole potentials have been used to guide [38, 39] and transport Bose-Einstein condensate (BEC) in a linear waveguide [40], and thermal atoms were guided through a hollow-core fiber [41, 42]. Magnetic waveguides have been used to study the propagation of matterwaves in a micro-fabricated chip setup [43, 44, 45] but so far restricted to linear propagation [45, 46, 47]. The presence of inhomogeneities in the micro-fabricated wires and thus in the guiding potential offers serious limitations on the coherent guiding over long distances [45]. Optimal control and inverse engineering methods have been used to design protocols for adiabatic transport [48, 49, 50] and acceleration [51, 52] of matterwaves. However, so far they have failed to enable the coherent transport of matter waves over macroscopic distances.

Realization of atomtronic circuits demand versatile atom trapping schemes [53, 54, 55, 56]. Among many neutral atom trapping geometries, ring-shaped atom circuits can be used to construct a guided matterwave Sagnac interferometer [57, 25]. Ring-shaped traps are also central in fundamental studies, e.g. understanding similarities between superfluidity and Bose-Einstein condensation [18], first detection of hysteresis in a ring atomtronic circuit [58]. A number of ring trapping schemes have been implemented based on the magnetic [59, 60, 61] and optical dipole trapping [62, 63]. The work presented here is based on the time-averaged adiabatic potential (TAAP) [53] ring traps and waveguides. This thesis mainly deals with the production of BECs in

optical dipole traps, adiabatically loading BECs into the ring potential, and then guiding them decoherence-free for long distances in TAAP rings.

In the following chapters of this thesis, I describe the relevant theoretical formulations, setup and experiment results. Chapter 2 deals with the theory of laser cooling and magnetic trapping of neutral atoms. It begins by explaining the idea behind the magneto-optical trap (MOT), magnetic trapping in a quadrupole trap, time orbiting potential (TOP) trap, and radio-frequency (rf) dressed adiabatic trap, and time-averaged adiabatic potential traps. The next section of this chapter describes the trapping of neutral atoms in an optical dipole trap, associated trapping frequencies, trap depth and more. Next, I briefly describe the principle of evaporative cooling in the TOP and optical dipole trap. Chapter 2 ends with the formulation for Bose-Einstein condensate (BEC).

In chapter 3, I explain different sections of the BEC experimental setup. It begins with the laser section of the BEC machine where details are provided about injection-locked slave laser, tapered amplifier, AOM distribution board, 2D-MOT and 3D-MOT setup. In the second section of this chapter, design and calibration of different magnetic coils are given, for the generation of magnetic quadrupole field, dc bias fields, audio-frequency fields, and the radio-frequency fields. Third section is about the optical dipole trap setup where I explain different elements of the dipole setup, alignment of the two dipole beams, and description of a home built safety interlock system. The chapter ends with an explanation of our absorption imaging system and the experiment control program.

Chapter 4 is about BEC production in the TOP and crossed-beam optical dipole traps. I begin by giving results related to the characterization of the TOP trap, i.e. correction of audio-frequency field amplitudes, phase, and circularity of the rotating bias field. Right after the characterization, the experimental sequence for the BEC production in a TOP trap, and results are provided. Second, BEC production in a crossed dipole trap is described together with the results.

After the production of BECs in optical crossed dipole traps, I describe the adiabatic loading of BECs from the dipole trap into a tilted ring trap, in chapter 5. First, I give the details of the ring loading sequence. Second,

characterization of the tilted ring traps and waveguides are presented, i.e., ring radius, trapping frequencies, cloud lifetime, dependence of ring radius on the magnetic gradient, audio-frequency and radio-frequency field amplitudes, and stability of the ring parameters over time. The last section of this chapter contains information about the flatness of our ring waveguide – with and without correcting the azimuthal modulation of the ring potential with static atoms. A Sagnac interferometer based on atom clock states will require an independent control of the two spin states of  $^{87}\text{Rb}$  in the ring potential. To that end, elliptic radio-frequency fields are used to create two wells in two opposite arms of the ring which gives trapping for the two spin states. In order to move the two trapping minima in a circle for the two states, an state independent tilt is added by using audio-frequency fields (gravity creates a trap in the azimuthal direction), which combined with the radio-frequency tilt gives an arbitrary control of the two azimuthal minimum. I give results for all the components, i.e., ultracold atoms in state dependent, independent, and the combined trap.

Chapter 6 is about the coherent acceleration and transport of BECs in tilted TAAP ring traps. In a interferometric sequence, it is important that atoms travel many round trips before the two atomic wave packets are combined and the signal is read. This will ensure the high sensitivity of the atom interferometer. The transport of BECs in the ring trap is done under the bang-bang scheme of optimal control theory, the chapter begins with the theoretical formulation of that. In the next section, the experiment results are presented related to the acceleration and transport sequence characterization, e.g., dependence of transport efficiency on the trap jump amplitude, circularity of the transport trajectory and centrifugal deformation of the ring trap due to the high angular speeds of atoms. Next, the transport results are described – angular position, deviation from the programmed trajectory, lifetime, stability of the cloud radius during the transport sequence.

The last chapter of this thesis, chapter 7 deals with the compact guiding of BECs and ultracold thermal atoms in a horizontal ring waveguide. This study is related to the atom interferometry using optical beam splitters (Bragg or Raman) and dynamic manipulation of momentum spread of the matter waves. Using the acceleration techniques of chapter 6, BECs are launched into the ring waveguide, and after a long free propagation, an azimuthal lens (tilted waveguide) potential is switched on for a very short duration (compared to the



---

lens trapping frequency) which either collimates or focuses travelling ultracold atomic beams. I give results for the BEC collimation and focusing in the TAAP ring waveguide. In the last section, I present splitting of BECs in a combined trap of ring and single beam dipole trap. In the end, chapter 8 summarizes the findings of this thesis and plans for the future work is given.

## Chapter 2

# Theory

### 2.1 Magneto-optical trap

#### Basic Idea

The magneto-optical trap (MOT), as the name suggests, is a combination of optical and magnetic field for both the cooling and trapping of neutral atoms. The two fields interact with the atomic energy levels to confine the atoms both in the real and momentum space. In order to implement the idea, three pairs of counter-propagating resonant laser beams and a magnetic quadrupole field are required. The three counter-propagating beam pairs are set orthogonal to each other to compensate for any three-dimensional atomic momentum vector. The frequency of the MOT laser beams is slightly red detuned with respect to the atomic transition frequency. It is done to make the atoms resonant with the light due to their Doppler shift. In other words, an atom with a finite velocity, moving towards the light source experiences a blue shift with respect to the source frequency and thus a red-detuned laser beam will make the light resonant with the atoms. If an atom absorbs a photon, due to the momentum conservation, it experiences a momentum kick away from the source. Therefore, an atom goes through a unit momentum loss with each photon absorption. A momentum kick due to the absorption is directional and it is set by the direction of the source. On the other hand, spontaneous emission has no preferred direction and its net effect averages out to zero. The final outcome is that the total loss (gain) in the momentum for atoms is governed by the absorption. However, due to the successive loss of momentum, atoms will no longer be

resonant with the light. This can be avoided two ways: either the laser beams have spatially varying frequency (detuning with respect to the atomic transition) or by adding a nonuniform magnetic field – lifts the degeneracy in magnetic sublevels. It is much more practical to implement the latter, e.g., a magnetic quadrupole field is added such that it overlaps with the laser beams intersection volume. A magnetic quadrupole field, around the center, is a linearly varying magnetic field, and as a result energy splitting between the magnetic sublevels increases linearly. In the presence of both the six near-resonant laser beams and magnetic quadrupole field, atoms keep going through the absorption-emission cycle, and a dense cold atomic ensemble can be trapped.

Below I describe the laser cooling mechanism, first, in its simplest form. Second, laser cooling is explained in the case of  $^{87}\text{Rb}$  atoms. Then the interaction of a magnetic dipole moment with an external dc magnetic field is described. Finally, this section ends with an explanation of the working of magneto-optical trap.

### 2.1.1 Laser cooling

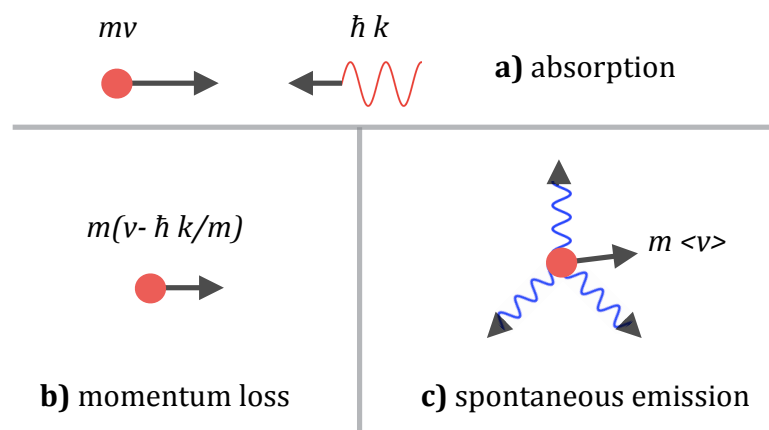


Figure 2.1: A simple scheme showing the laser cooling process in three steps. a) The atom absorbs a photon, b) due to the absorption the atomic momentum reduces, and c) the atom emits photons in random directions, with the net momentum due to the emission equal to zero.

Let us begin with a simple picture, consider a two level atom of mass  $m$ , and moving with velocity  $v$  (see Fig. 2.1). A resonant laser beam is shone such that the

beam propagation direction is opposite to that of the atomic momentum. If the frequency of the laser beam is red-detuned by an amount equal to the Doppler shift of the atomic transition, i.e.  $v \times 2\pi/\lambda = kv$ , the atom will become resonant with the light and absorb a photon. It is the momentum conservation that the atomic momentum goes down by  $\hbar k/m$ , given the momentum of the photon is  $\hbar k$ . The atom will decay to the ground state after a time set by the linewidth of the excited state. By the radiative decay process, atom returns to the ground state and a photon is emitted in a random direction. After many of this absorption emission cycle, net loss in the atomic momentum is given by the absorption and momentum change due to the emission averages to zero. The force on an atom due to the photon scattering, is:

$$\mathbf{F} = m \frac{d\mathbf{v}}{dt} = \hbar \mathbf{k} \gamma \quad (2.1)$$

where  $\hbar k$  is the photon momentum,  $m$  is the atomic mass, and  $v$  is the atomic velocity. The scattering rate is given by the equation,

$$\gamma = \frac{\Gamma}{2} \frac{s}{1 + s + (\frac{\delta}{\Gamma/2})^2} \quad (2.2)$$

where  $s$  is saturation parameter, equal to  $s = I/I_s$ , i.e. ratio of the laser beam intensity  $I$  to the saturation intensity  $I_s$ ,  $\delta$  is detuning from the atomic transition, and  $\Gamma$  is the natural linewidth. The scattering force on the atoms, using Eq.2.2, is:

$$\mathbf{F} = \hbar \mathbf{k} \frac{\Gamma}{2} \frac{s}{1 + s + (\frac{\delta}{\Gamma/2})^2} \quad (2.3)$$

The maximum scattering force is exerted on the atoms when they absorb emit maximum number of photons, i.e. at a very high laser intensity or  $s \gg 1$ . This is when the excited level is saturated, and the population in both the levels becomes  $1/2$ . The maximum scattering force on the atom is then,  $\mathbf{F} = \hbar \mathbf{k} \frac{\Gamma}{2}$ .

To give an estimate for  $^{87}\text{Rb}$  atoms, a 780 nm laser (resonant with atomic transition) will reduce the velocity by about 6 mm/s after each absorption. At room temperature atoms move around with a velocity of about 300 m/s. It will take about 50,000 photons to be absorbed by an atom for it to completely come at rest. The time it will take to remove all the kinetic energy from the atom will

depend on the number of absorption-emission cycle per unit time, or decay rate of the excited state. Again, for a  $^{87}\text{Rb}$  atom, it can be brought at rest only in 1 ms. However, as the atomic velocity reduces atoms are no longer resonant with the light. The solution to keep the atoms in this radiative cycle is a magneto-optical trap, described below. This principle was used in the first laser cooling experiment, where thermal atoms of Na were decelerated.

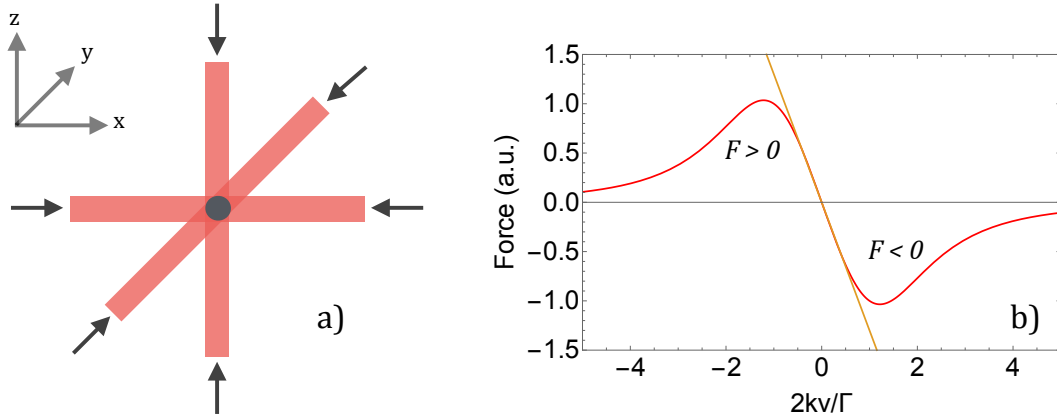


Figure 2.2: a) 3D optical molasses configuration. b) The scattering force on an atom in the presence of two counterpropagating near-resonant laser beams – 1D optical molasses.

Now let us switch to the standard optical molasses setting, i.e. 3D cooling of atoms using three pairs of mutually orthogonal resonant laser beams, see the scheme in Fig. 2.2. This case can be simplified by looking at the average force on an atom in the presence of two counter-propagating red-detuned laser beams. Eq. 2.3 gives the scattering force due to a single beam and for two beams the average force would be the sum of the force, can be written as:

$$\begin{aligned}
 \mathbf{F}_{\text{av}} &= \mathbf{F}_{\text{left}} + \mathbf{F}_{\text{right}} \\
 &= \hbar \mathbf{k} \frac{\Gamma}{2} \left[ \frac{s}{1 + s + (\frac{\Delta - kv}{\Gamma/2})^2} - \frac{s}{1 + s + (\frac{\Delta + kv}{\Gamma/2})^2} \right] \\
 &= \hbar \mathbf{k} \frac{\Gamma skv}{2 \Gamma} \frac{16\Delta/\Gamma}{1 + \frac{8}{\Gamma^2}(\Delta^2 + k^2v^2) + \frac{16}{\Gamma^2}(\Delta^2 - k^2v^2)^2}
 \end{aligned} \tag{2.4}$$

where  $\mathbf{F}_{\text{left}}$  and  $\mathbf{F}_{\text{right}}$  are the scattering force from two the two beams, frequency

detuning  $\delta$  is written in terms of Doppler shift  $kv$  for the two directions. The resultant force is plotted in Fig. 2.2b), very clear that the sign of the force reverses as the direction of the atomic velocity changes. There is a region around  $v = 0$  where this force is linearly proportional to the atomic velocity and acts as a friction force on a moving body in a viscous medium. This force is maximum when the detuning  $\delta = \Gamma/2$ , and corresponds to the maximum reduction in the kinetic energy of the atoms, called Doppler cooling limit. The minimum temperature set by the Doppler limit can be obtained by equation,  $k_B T = \hbar\Gamma/2$ . For  $^{87}\text{Rb}$  atoms, the Doppler limited temperature is  $146 \mu\text{k}$ . A point to note is that there is no restoring force on the atoms in an optical molasses or it is not a trap and the effect is purely on the atomic momentum spread. Another problem, apart from cooling limit due to the Doppler shift, is the atoms falling to a dark state, and they go out of the radiative cycle.

Below I give the  $^{87}\text{Rb}$  energy level diagram, levels involved in the laser cooling and optical pumping (will refer to as *repumper* at later stages). Fig. 2.3 shows the hyperfine levels of  $^{87}\text{Rb}$  for the ground-state  $5^2\text{S}_{1/2}$  and excited-state  $5^2\text{P}_{3/2}$  [64]. The cooling line shown in the figure addresses a cycling transition of linewidth  $2\pi 5.89 \text{ MHz}$ , and requires a narrow linewidth laser at a wavelength of  $780.24 \text{ nm}$ . The frequency of the cooling laser is red-detuned ( $\delta_{\text{MOT}}$ ) from the atomic transition, typically by a few times the natural linewidth ( $\Gamma$ ). The population which falls back to  $F = 1$  in the ground state (because some atoms are excited to  $F = 2$  in  $5^2\text{P}_{3/2}$  and decays to  $F = 1$ ), is pumped back with a repumper laser. The frequency of the repumper laser is about  $6.8 \text{ GHz}$  higher than that of the cooling laser. The repumper laser is kept resonant with the transition as shown in the Fig. 2.3.

## 2.1.2 Magnetic trapping

The idea of magnetic trapping of neutral atoms has its roots in the Stern-Gerlach effect [65]. A magnetic dipole experiences a force when placed in an external nonuniform magnetic field. If the field is spatially homogeneous, the magnetic force is zero. If the  $\mathbf{B}$  field amplitude is spatially varying, the derivative of the interaction potential energy  $V(\mathbf{r}) = -\boldsymbol{\mu} \cdot \mathbf{B}$  is,  $\mathbf{F} = \boldsymbol{\mu} \cdot \Delta\mathbf{B}$ , is the force exerted on the atom by an external magnetic field. The atoms carrying an unpaired electron in its outermost shell has a magnetic moment, given by,  $\boldsymbol{\mu} = m_F g_F \mu_B$  where  $m_F$

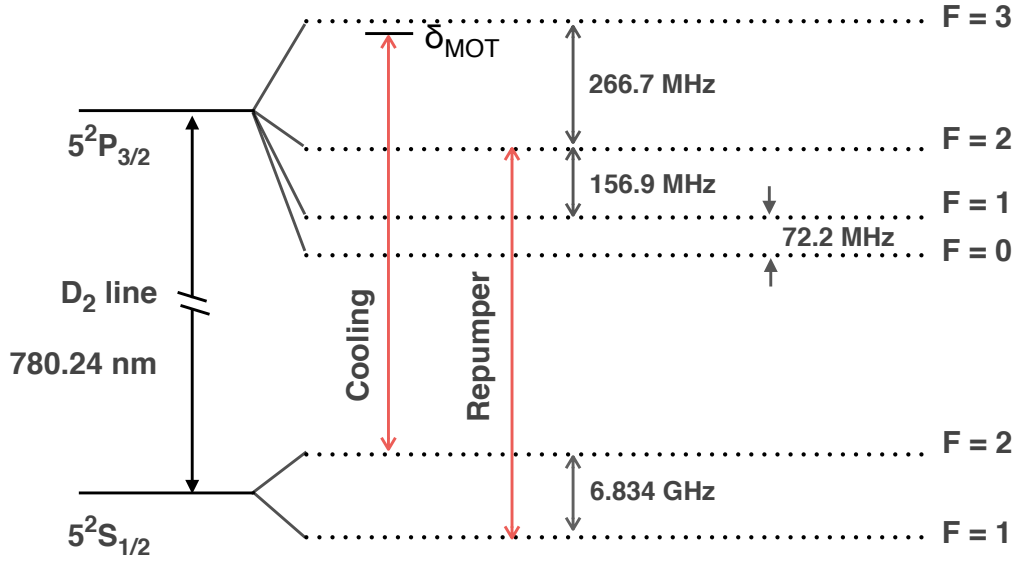


Figure 2.3: Hyperfine energy levels associated with the laser cooling of  $^{87}\text{Rb}$ .

is the magnetic quantum number,  $g_F$  is the Landé  $g$ -factor, and  $\mu_B$  is the Bohr magneton. The hyperfine  $g_F$  factor is [64],

$$g_F = g_J \frac{F(F+1) - I(I+1) + J(J+1)}{2F(F+1)} + g_I \frac{F(F+1) + I(I+1) - J(J+1)}{2F(F+1)} \quad (2.5)$$

where  $F$  is the total atomic angular momentum,  $F = J + I$ ,  $J$  is the total electronic angular momentum,  $J = L + S$ ,  $L$  and  $S$  are the electronic orbital and electronic spin angular momentum, respectively, and  $I$  is the total nuclear angular momentum. For the case when the atomic magnetic moment is positive,  $\mu > 0$ , the magnetic potential energy  $V$  will be negative, and the atoms will experience an attractive force towards the field minimum and vice versa. To create a trap for the low field seekers (atoms with  $\mu > 0$ ), it needs a magnetic field configuration in 3D which has a minimum in free space. Another allowed configuration would be a magnetic field maximum in free space, to trap high field seekers, but not practical to generate such a field distribution.

A very simple configuration to trap the low field seekers, is a magnetic quadrupole field. The first magnetic trapping of neutral atoms was demonstrated in this quadrupole trap [11]. It can be generated by using two current carrying coils in an anti-Helmholtz arrangement. The magnetic field amplitude increases linearly away from the zero-field point at the center. The field gradient along the axial direction is double than that in the radial plane,  $B = \alpha(x, y, -2z)$ . The trap depth of a quadrupole trap can easily reach up to tens of millikelvin – atoms with this maximum temperature/energy stay in the

trap. It depends on the gradient of the magnetic field or the current flowing through the coils. Fig. 2.4a shows a schematic diagram of the quadrupole trap. If the B-field is weak, Breit-Rabi formula [66] gives the energy of the Zeeman sublevels, for the quadrupole field and  $^{87}\text{Rb}$  atom it is shown in Fig. 2.4b. The low field seekers or the states which can be trapped in a magnetic trap are those which has  $\mu > 0$ , for  $^{87}\text{Rb}$  the trappable states are,  $|1,-1\rangle$ ,  $|2,1\rangle$ , and  $|2,2\rangle$ . The atoms stay in the trap as long as their magnetic moment is aligned with the B-field. The atomic magnetic moment precesses around the B-field on a timescale given by the Larmor frequency,  $\omega_L = \mu B/\hbar$ , clearly depends on the B-field amplitude. Fig. 2.4c) shows precession of the magnetic moment around the B-field. There is a condition for adiabaticity to be fulfilled for the atoms to remain trapped:  $\dot{\omega}_L \ll \omega_L^2$ . This condition can be violated, for e.g., if the B-field amplitude or direction changes much faster than the Larmor frequency or the atom moves so fast that it can not follow the B-field change. The result will be the depolarization of the atoms, i.e. by changing its internal state the atom leaves the trap.

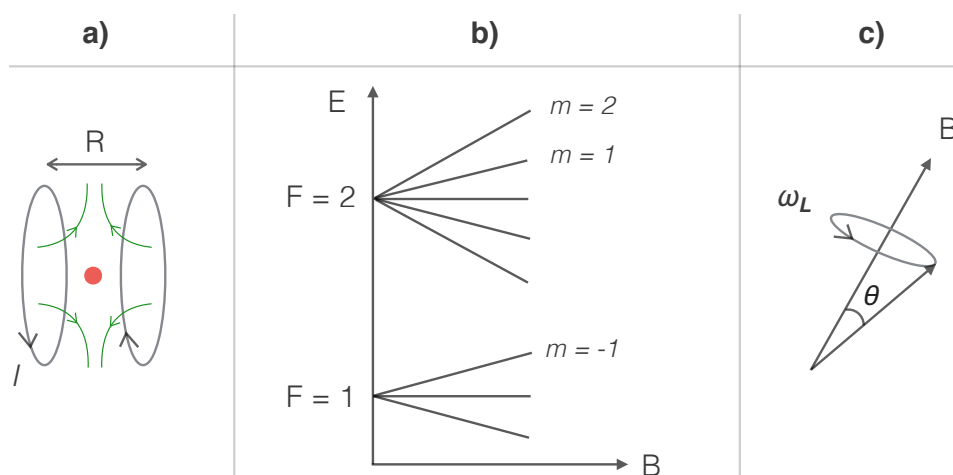


Figure 2.4: a) Coils in the anti-Helmholtz configuration produces the magnetic quadrupole field, trapped atoms shown in red at the center. The arrows show the B-field directions. b)  $^{87}\text{Rb}$  Zeeman sublevels in a quadrupole field for the two hyperfine levels of ground state in the weak-field regime (the labelled magnetic sublevels are the ones which can be trapped). c) Precession of the atomic spin around the local B-field direction.

A zero B-field point exists at the center of quadrupole trap since the field generated by the two opposing coils cancel. As said above, if the atomic spin is aligned with the spatially varying B-field, atoms would remain trapped. The field direction changes most rapidly around the center of a quadrupole trap. Atoms passing through the zero-field can lose the relative alignment of the magnetic moment to the B-field or their spin will be flipped to other states, untrapped or anti-trapped. This is called Majorana spin flip loss [67]. The loss rate or the probability to transit to other states is inversely proportional to



the thermal velocity of the atom passing through the center, or  $\Gamma \propto T^{-2}$ . As a result, a colder atomic ensemble will have a lower lifetime in the quadrupole trap compared to a hotter sample. For a few microkelvin temperature atom cloud, the lifetime is of the order of seconds in this trap.

### 2.1.3 A combination: magneto-optical trap

In the two sections above, I presented laser cooling and magnetic trapping of neutral atoms. To produce a high density cold atomic ensemble, both the techniques are not sufficient on their own. In the case of laser cooling it is atoms going out of resonance with the laser beam as their momentum reduces, and an optical molasses does not provide spatial confinement. A magnetic quadrupole trap, alone, has a very low trap depth and hence can not be used to capture the atoms from the background. However, the linearly increasing magnetic field of quadrupole trap is an answer to the much-needed spatial detuning against the changing Doppler shift. Fig. 2.5 shows the overlap of the optical molasses and a magnetic quadrupole field. The combination is called magneto-optical trap (MOT). The first realization of a magneto-optical trap was done in the optical molasses setup by simply adding a spherical quadrupole field [12]. The trap depth of the MOT can extend even up to a few Kelvin [68], and atoms can be loaded in this trap from the room temperature vapor [69].

Fig. 2.5 shows a schematic of configuration of the MOT. The setup has two counter-propagating laser beams along all the three Cartesian axes and coils in an anti-Helmholtz configuration. The coils which produce the magnetic quadrupole field are placed such that the zero of the magnetic field lies at the center of the laser beam overlap volume. To understand the working of this trap, let us first consider a 1D picture, and the idea can be easily extended to 3D. Along the  $x$  axis, due to the external B-field the magnetic sublevels of an atom are shifted proportional to the B-field amplitude, in this case the energy shift is linear. The polarization of the laser beams is set circular and opposite for the beams anti-parallel to each other. The frequency of the laser beams ( $\omega_L$ ) is red-detuned by  $\delta$ , from the atomic transition frequency for the laser cooling. For the atoms at rest, the atomic transition frequency is  $\omega_0$ . In the case of a two-level with a transition from  $J = 0$  to  $J = 1$ , there will be three Zeeman sublevels in  $J = 1$  and  $J = 0$  will remain degenerate. If an atom moves towards the  $+x$  direction, will absorb photons from the  $L(\sigma_-)$  beam (left circularly polarized light), and due to the successive momentum kicks will be pushed towards the center. This time the atom will remain resonant with the laser beam because of the linearly decreasing magneto-optical detuning. From the selection rules,  $R$  and  $L$  beams drive  $\Delta m = +1$  and  $\Delta m = -1$  transitions, respectively. For the

atoms with momentum vector towards the  $-x$  direction, the momentum loss comes by absorbing photons from the  $R(\sigma_+)$  beam. Since there are beams in all the six directions, for any atomic momentum vector there will be a restoring force towards the center and hence this configuration traps the atoms. Instead of having beams mutually orthogonal to each other, other arrangements are also utilized, e.g, retro-reflected beams at 120 deg. The idea is to cancel any momentum vector of the atoms in 3D.

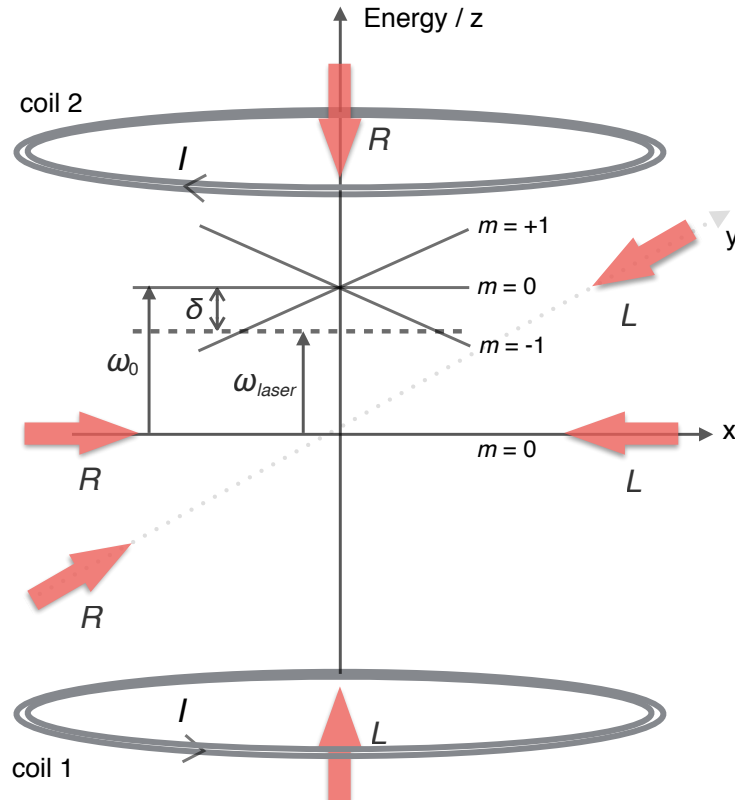


Figure 2.5: Schematic diagram of the magneto-optical trap. The Zeeman splitting is much smaller compared to the photon energy. R and L stand for the right and left circular polarization of the light.  $m$  represents the Zeeman sub-level.  $\omega_0$ , and  $\omega_{\text{laser}}$  are the atomic transition frequency, and the laser frequency, respectively.  $\delta$  is the detuning of the MOT laser beams, from the transition frequency.  $I$  is the current in the magnetic quadrupole coils.

To further increase the phase space density, the scattering rate is reduced for a very short time and as a result, atoms experience a lower radiation friction force. This step is done in a very short time making sure the cloud does not fall due to the gravity, and right before transferring the atoms into the magnetic trap. Once a saturation is reached in the MOT loading, reducing the photon scattering rate lowers the cloud size to achieve higher atomic density, utilized later in the evaporation stage. Each atom in the cloud sees photons from the laser beam and emitted photons from other atoms. Latter is more pronounced for the atoms which are deep inside the cloud or near the center. This effect

puts an upper limit on the achievable atomic density. During the compressed MOT (CMOT) stage, detuning of the laser beams is ramped downwards, from MOT detuning to tens of linewidth ( $\Gamma$ ) in a short duration (up to tens of ms). After the CMOT, the magnetic gradient is switched off for again a very small duration and the cloud is cooled further much below the Doppler limit, called polarization gradient or Sisyphus cooling [9].

## 2.2 A hybrid trap – dipole plus magnetic

First, let us go through the optical dipole trapping of neutral atoms. The trapping of dielectric particles by the use of a laser beam was first shown by Ashkin in 1970 [2]. The idea is not very different than of the magnetic trapping, i.e. as a magnetic dipole interacts with an external B-field similarly an electric dipole when placed in an electric field, interacts, and experiences a potential. The term *dipole* because the trapping here rely on the interaction of particle's electric dipole moment with a far-off resonant laser beam and the scattering force is negligible. Again, depending on the net sign of the potential energy (sign of the magnetic or electric dipole moment) either the particle is attracted towards the field minimum or maximum. The profile of an external B-field decides the shape of the Zeeman splitting, here, the hyperfine levels are shifted in space spatial according to the laser beam intensity, called ac-stark shift. The potential energy of the particle is directly proportional to the laser beam intensity. In the case of a far red-detuned (blue-detuned) focusing laser beam, a trap is formed with its center at the beam focus, for the particles with electric polarizability positive (negative).

A classical approach says that if a polarizable particle is placed in an electric field  $E(\mathbf{r}, t)$ , the field will induce an electric dipole moment  $\mathbf{p}(\mathbf{r}, t)$  of amplitude  $\tilde{p} = \alpha \tilde{E}$ . The electric field is of the form  $E(\mathbf{r}, t) = \tilde{e} \tilde{E}(\mathbf{r}) \exp -i\omega t + c.c.$ , where  $\tilde{e}$  is the unit polarization vector,  $\omega$  is the frequency of the field, and  $\tilde{E}$  the field amplitude. The polarizability  $\alpha$  depends on the frequency of the driving field and is a complex quantity,  $\alpha = \alpha(\omega)$ . The interaction potential of the electric dipole in t is:

$$V_{od} = -\frac{1}{2} \langle \mathbf{p} \mathbf{E} \rangle = -\frac{1}{2\epsilon_0 c} \text{Re}(\alpha) I \quad (2.6)$$

where  $I$  is the driving field intensity, equal to  $2\epsilon_0 c |\tilde{E}|^2$ . The derivative of the potential then gives the dipole force onto the particle/atom exerted by the electric field, given by:

$$F_{od} = -\Delta V_{od}(\mathbf{r}) = \frac{1}{2\epsilon_0 c} \text{Re}(\alpha) \Delta I(\mathbf{r}) \quad (2.7)$$

The imaginary part of the complex polarizability  $\alpha(\omega)$  which is responsible for the absorption-emission of the photons governs the power absorbed by the atoms,  $P_{od} = 2\omega\text{Im}(\alpha)I(\mathbf{r})$ . Hence, the number of photons scattered per unit time has the form:

$$\gamma_{od}(\mathbf{r}) = \frac{P_{od}}{\hbar\omega} = \frac{1}{\hbar\epsilon_0 c} \text{Im}(\alpha)I(\mathbf{r}) \quad (2.8)$$

From the equations above, it is clear that the real part of  $\alpha$  corresponds to the dipole potential (conservative) and the imaginary part photon scattering, and they both depend on the spatial intensity of the beam. An expression for the atomic polarizability can be found by the Lorentz's model. In the case of a small laser detuning from the transition frequency ( $\Delta \ll \omega_0$ ), by the use of rotating wave approximation the expression for the dipole interaction potential and scattering rate reduces to [70]:

$$V_{od}(\mathbf{r}) = \frac{3\pi c^2 \Gamma}{2\omega_0^3 \Delta} I(\mathbf{r}), \quad (2.9)$$

$$\gamma_{od}(\mathbf{r}) = \frac{3\pi c^2}{2\hbar\omega_0^3} \left(\frac{\Gamma}{\Delta}\right)^2 I(\mathbf{r}), \quad (2.10)$$

From the equations above, if the detuning is negative ( $\Delta < \omega_0$ ) atoms are attracted towards the field minimum and vice-versa. Another point to note is that the conservative light potential has  $1/\Delta^2$  dependence and the scattering rate  $1/\Delta^2$ , by going far from the resonance  $\gamma_{od}$  can be reduced. If the laser detuning is much below the transition frequency, the detuning term disappears and the dipole potential then only depends linearly on  $I(\mathbf{r})$ . Let's look at the widely used case of dipole trapping, a focused far-detuned Gaussian laser beam propagating along the  $z$  axis, shown in Fig. 2.6. The intensity profile of the laser beam is given by,

$$I(r, z) = \frac{2P}{\pi\omega(z)^2} \exp\left(\frac{-2r^2}{\omega(z)^2}\right) \quad (2.11)$$

where  $r$  and  $z$  are the radial and axial coordinates,  $P$  is the beam power, and  $\omega(z)$  the beam size along the propagation ( $z$ ) axis. The  $1/e^2$  beam size has the form,

$$\omega(z) = \omega_0 \sqrt{1 + \left(\frac{z}{z_R}\right)^2} \quad (2.12)$$

where  $z_R$  is the beam's Rayleigh length (the distance from the focus where the beam waist increases by  $\sqrt{2}$ , is equal to  $\pi\omega_0^2/\lambda$ ) and  $\omega_0$  is the beam waist. Going back to the Eq. 2.9, of the dipole potential and replacing  $I\mathbf{r}$  by the one of the beam profile above, we get the  $V_{OD}$  of our interest. This potential is harmonic only near the trap bottom or for the atoms with kinetic energies much smaller than the trap depth ( $k_B T \ll \tilde{V}$ ). The

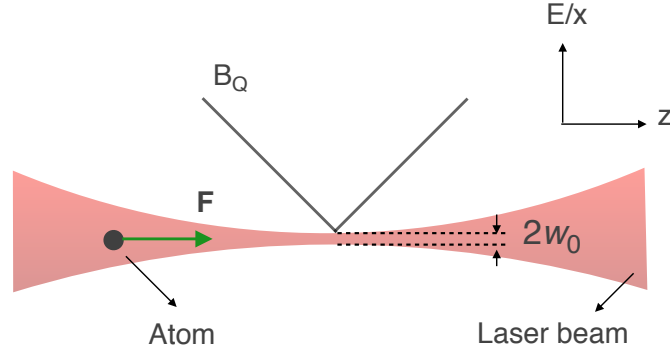


Figure 2.6: A hybrid trap consisting of a focused Gaussian laser beam and a magnetic quadrupole field.  $F$  represents the dipole force on the atom,  $B_Q$  represents the magnetic quadrupole gradient,  $2w_0$  is the beam waist diameter, and  $E$  stands for energy.

dipole potential in the above-mentioned regime is then given by:

$$V_{od}(r, z) \simeq \tilde{V} \left[ 1 - 2 \left( \frac{r}{\omega_0} \right)^2 - \left( \frac{z}{z_R} \right)^2 \right] \quad (2.13)$$

The trapping frequencies can be obtained by equating the radial and axial terms with the standard potential energy equation, i.e.  $1/2m\omega^2$ , and we get  $\omega_r = 2\sqrt{\tilde{V}/m\omega_0^2}$  and  $\omega_z = \sqrt{2\tilde{V}/mz_R^2}$  along the radial and axial axes, respectively. In a single laser beam dipole trap,  $\omega_r$  is much higher than  $\omega_z$ , by a factor  $\sqrt{2}(z_R/\omega_0)$  which is typically a few hundred. The result is a low density (collision rate) atomic gas which is not suitable for evaporation. A solution is to add a weak magnetic quadrupole field, helps in keeping the atoms spin-polarized and the longitudinal trapping frequency modifies (increases) to,  $\omega_z = (1/2)\sqrt{\mu\alpha/m\Delta z}$ , where  $\Delta z$  is the displacement of the B-field zero from the dipole minimum [71]. Another solution is a crossed beam dipole trap where the focus of two beams are intersected to increase the longitudinal trapping strength [70], and can be combined with a magnetic quadrupole as in the case of single beam for low beam angles. In our experiment, the two beams cross at an angle of  $17^\circ$  and corresponds to an aspect ratio of about 3.5 in the radial plane, which we further decrease by adding a quadrupole field. Evaporative cooling in a dipole trap is carried out by lowering the trap depth, i.e. laser beam intensity exponentially. The atoms with kinetic energies larger than the trap depth are ejected and the sample is cooled down.

## 2.3 Magnetic traps of this thesis

### 2.3.1 Time-orbiting potential trap

Due to the zero of the B-field at the center of the quadrupole trap, spin flip loss does not allow to reach the state of quantum degeneracy. To overcome this, if the B-field zero is displaced a few times the atom cloud size (kinetic energy/temperature of the atoms) and rotated in a circular trajectory, the cloud lifetime increases substantially and the time-averaged potential is a harmonic one [15]. The circle made by the rotating quadrupole field zero is called circle of death (atoms passing through the moving field zero leave the trap), its radius  $r = B_m/\alpha$ . where  $B_m$  and  $\alpha$  are the bias field amplitude and magnetic gradient, respectively. The trap depth of this trap is proportional to the amplitude of the bias field (spatial extent of the circle of death), given by  $U \approx 0.41\mu B_m$ . The addition of the bias field does not change the position of new harmonic trap minimum with respect to the quadrupole potential in the radial plane. However, along the gravity axis, due to the position dependent force on the atoms in a harmonic confinement there is a gravitational sag on the atoms, given by  $\Delta z = g/\omega_{\text{trap}}^2$ . This means that the atom cloud in a tight harmonic trap will sit closer to the center of the quadrupole field zero compared to a weaker trap. As the magnetic gradient is decreased, the point when the gravitational force is equal to the magnetic one, there remains no trap, at  $mg = \mu\alpha$ , this  $\alpha$  is 15.25 Gpcm for  $|1,-1\rangle$  state of  $^{87}\text{Rb}$ . Also, the trapping frequency is modified in the presence of the gravity.

For the TOP trap to work, the frequency of the rotation of the quadrupole field has to follow the relation:  $\omega_{\text{trap}} \ll \omega_{\text{bias}} \ll \omega_L$ , where  $\omega_L$  is the Larmor frequency,  $\omega_{\text{trap}}$  is the eventual trapping frequency of the harmonic trap, and  $\omega_{\text{bias}}$  is the rotation frequency of the bias field. The above condition says that when a rotating bias is added the atomic magnetic moment should still be able to follow the spatially varying B-field adiabatically ( $\mu$  remains aligned with the B-field), and the bias should not affect the periodic motion of the atoms in the trap. The first atomic Bose-Einstein condensate (BEC) was realized in a TOP trap, in 1995 [16].

### Trapping frequencies

A simple TOP trap can be generated by rotating the quadrupole field in a circle and the rotation frequency should be fast such that the atoms do not follow the quadrupole minimum. The rotating bias can be generated by using two orthogonal pairs of coils

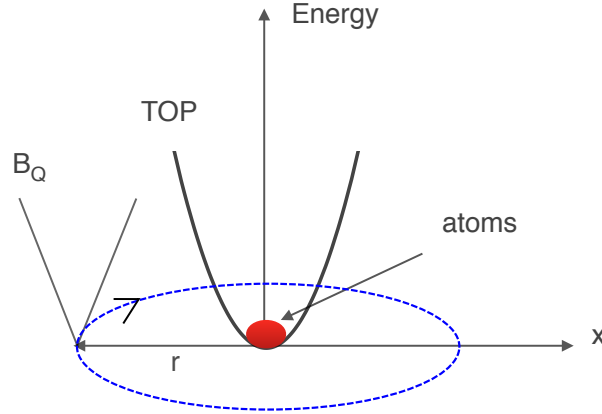


Figure 2.7: Scheme of the time-orbiting potential trap. The atoms are trapped at the center of the rotating quadrupole field, in a harmonic TOP trap.  $B_Q$  represents the instantaneous quadrupole field.  $r$  is the displacement of the quadrupole field due to the bias field, called the radius of the circle of death.

which are fed with sine (cosine) current signals oscillating 90 deg out of phase. The frequency of the bias field is typically of the order of a few kilohertz. Let us take the case of bias field rotation in a plane orthogonal to the gravity axis. The total magnetic field is:

$$\mathbf{B} = \alpha \begin{pmatrix} x \\ y \\ -2z \end{pmatrix} + \begin{pmatrix} B_m \cos(\omega_m t) \\ B_m \cos(\omega_m t + \pi/2) \\ 0 \end{pmatrix} \quad (2.14)$$

where  $\alpha$  is the magnetic quadrupole gradient,  $B_m$  is the bias field amplitude, and  $\omega_m$  is the bias field frequency. The magnetic potential energy is the dot product of the atomic magnetic moment and the B-field, i.e. a scalar quantity and only depends on the B-field amplitude. The amplitude of the B-field is given by,

$$|\mathbf{B}| = \sqrt{\left(\frac{\alpha}{2}x + B_m \cos \omega_m t\right)^2 + \left(\frac{\alpha}{2}y + B_m \sin \omega_m t\right)^2 + \alpha^2 z^2} \quad (2.15)$$

The magnetic potential energy of the atoms in a TOP trap is then,  $V(\mathbf{r}, t) = -\mu|\mathbf{B}|$ , where  $\mu = m_F g_F \mu_B$ . The integration of the potential energy over one cycle of the bias field gives the time-averaged potential, which has the form:

$$V_{av}(r) = \mu \left[ B_m + \frac{\alpha^2}{16B_m} (x^2 + y^2 + 8z^2) \right] \quad (2.16)$$

where only the first order terms are shown. The potential is harmonic near the center of the trap, or for the distances small compared to the radius of the circle of death. Comparing this form of the potential energy with the standard potential energy

expression,  $V(r) = \frac{1}{2}m\omega^2r^2$  gives the trapping frequencies along all the three directions. The radial and axial trapping frequencies of a TOP is:

$$\begin{aligned}\omega_r &= \alpha \sqrt{\frac{\mu}{8mB_m}} \\ \omega_z &= \alpha \sqrt{\frac{\mu}{mB_m}}\end{aligned}\tag{2.17}$$

An important point to note here is that the trapping frequency along the axial direction ( $\omega_z$ ) is  $2\sqrt{2}$  times higher than that of the radial one (cylindrical symmetry,  $\omega_x = \omega_y$ ). As a result, the trap shape (atom cloud shape) is like an oblate spheroid. Since the trapping frequencies depend on the magnetic moment, the trapping strength varies with the Zeeman sublevel and the hyperfine Landé g-factor. The calculation above does not include the effect of gravity. If the gravitational potential energy term,  $mgz$  is added in the Eq.2.16, the radial and the axial trapping frequencies will get a prefactor of  $(1 - \eta^2)^{1/4}(1 + \eta^2)^{1/2}/2$  and  $2(1 - \eta^2)^{3/4}$ , respectively, where  $\eta = mg/2\mu_B\alpha$  is the gravitation correction factor [72].

### Radio-frequency evaporation

Fig. 2.8 shows a schematic of the radio-frequency (rf) induced evaporation of atoms in a TOP trap. The addition of a rotating bias field to the magnetic quadrupole starts to move the field zero in a circle. The instantaneous quadrupole field is shown in the figure 2.8. The atoms see the time-averaged potential and sit at the center of the rotating zero. To evaporate the atoms from the trap, an rf-field is switched on at a frequency such that the rf-field photon energy ( $h\nu_{\text{RF}}$ ) is equal to the Zeeman splitting between the two magnetic sublevels. Due to the spatial spread of the atom cloud, the atoms resonant with the rf-field transit to other Zeeman levels (untrapped and anti-trapped) and eventually leave the trap. The probability of spin flip transitions is given by the strength of the rf-field (Rabi frequency, typically tens of milliGauss) and relative orientation of the rf-field and local B-field. The efficiency of the evaporation process can be characterized by looking at the atom number loss against the temperature drop,  $T_{\text{final}}/T_{\text{start}} = [N_{\text{final}}/N_{\text{start}}]^\alpha$ . The evaporation coefficient  $\alpha$  depends on the logarithmic derivatives of  $N$  and  $T$  since the evaporation follows an exponential scaling.

The starting frequency of the rf-field is chosen such that we first address (eject) the hotter atoms since they spend more time near the edge of the atom cloud. To evaporate the atom cloud in a continuous manner, the rf-field frequency is ramped down linearly. The duration of the frequency ramp is set by the elastic collision time between the



atoms, or higher the collision rate faster the evaporation can be done. Due to the rethermalization process, the removed energy (taken out by the ejected atom) is continuously shared among the atoms and the net kinetic energy of the sample goes down – cooling. When the rf-field frequency becomes equal to the Zeeman splitting at the center of the trap i.e.  $h\nu_{\text{RF}} = \mu B_m$ , all the atoms perform spin flips and the trap is emptied. Interestingly, this is a very precise way to measure the rotating bias field amplitudes and the relative phase between the two field components (see chapter 4).

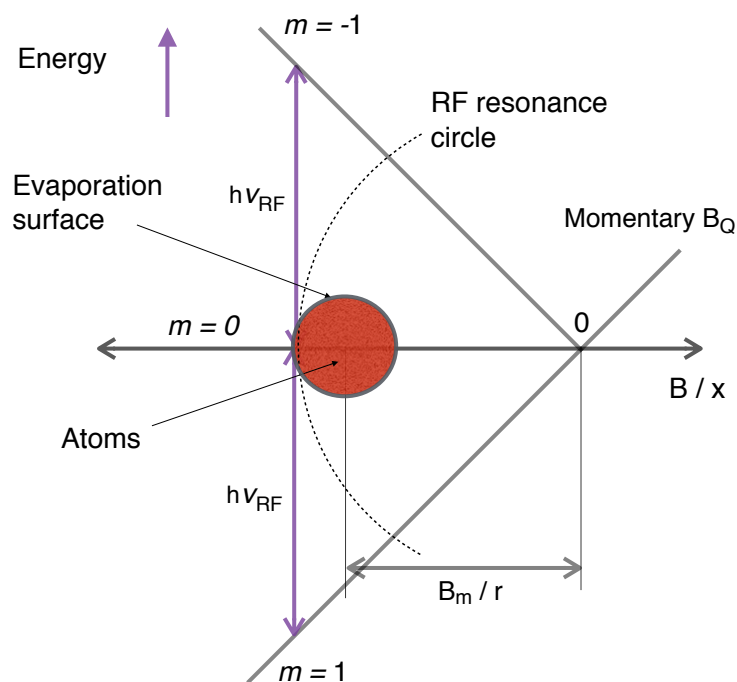


Figure 2.8: A diagram depicting the radio-frequency induced evaporation in a time-orbiting potential trap.

### 2.3.2 RF dressed adiabatic potentials

By the use of radio-frequency (rf) dressing of neutral atoms in dc magnetic traps a variety of trapping geometries can be generated, such as two-dimensional traps, rings, rf lattices, double wells and more. The different shapes of the neutral atom trap are essential for the realization of practical atomic sensors, atomic clocks, atomtronics, and quantum simulation [73, 74, 61]. The shape of this rf dressed trap is given by the orientation and polarization of the rf-field with respect to the dc trap B-field configuration (quadrupole or Ioffe-Pritchard). The coupling of the rf-field with the local dc magnetic field is maximum when the rf and static-field vectors are orthogonal to each other (cross product of the two vectors) and in 3D this gives an isopotential

surface. If the effect of gravity is ignored, the shape of this isopotential surface is then the shape of the trap (atom cloud). For example, in a magnetic quadrupole trap, a linearly polarized rf-field along the axial direction will have maximum coupling in a circle (ring), the center of the ring will be same as of the quadrupole trap. If a circularly polarized rf-field is used in the radial plane, coupling will be maximum at the bottom (top) of an *egg shell* shaped isopotential surface depending on the internal state of the atom. The size of the rf-dressed trap can be simply tuned by changing the rf-field frequency since the coupling occurs at a distance from the quadrupole center where the rf photon energy is equal to the Zeeman splitting between the magnetic sublevels.

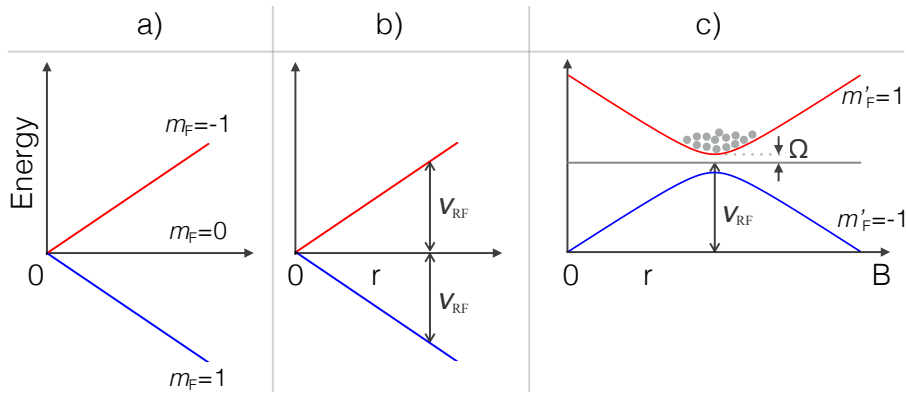


Figure 2.9: The idea of rf-dressing of neutral atoms in a linear dc trap in three steps. a) The three magnetic sublevels (bare states) of  $F = 1$  hyperfine level. b) A weak rf-field resonant with the Zeeman levels couples the bare states, principle behind the rf evaporation. c) A strong rf-field creates an avoided-crossing at the rf-field resonance point, shown in 1D, and the resonance surface creates a trap in 3D.

To understand the working of an rf-dressed trap, let us start with the bare states. Fig. 2.9a shows the Zeeman splitting of  $F = 1$  hyperfine level of an atom in a linear magnetic trap. Fig. 2.9b shows the mechanism behind the rf-induced evaporation of atoms. A weak rf-field with frequency  $\nu_{\text{RF}}$  is resonant with the magnetic sublevels at a distance  $r = h\nu_{\text{RF}}/\mu B$ . The atoms passing through this resonance point (surface) transit to other Zeeman states which are either untrapped or antitrapped and eventually leave the magnetic trap. When the rf amplitude is relatively high (strong coupling), as shown in the Fig. 2.9c, a semi-classical description can be obtained from the Landau-Zener model to quantify the probability for an atom to remain in the adiabatic state [75, 76]:

$$P = 1 - \exp(-\pi\Lambda) \quad (2.18)$$

where  $\Lambda$  is the adiabaticity parameter, given by  $\Lambda = V_0^2/\lambda$ . The coupling strength  $V_0$  then defines the probability for an atom to follow the adiabatic path as it crosses the rf resonance.  $\lambda$  is the rate of change of the potential in space times the atomic speed,

$\lambda = v\Delta V(\mathbf{r})$ . It is evident from Eq. 2.18 that there is a range in  $\Lambda$  where the adiabatic approximation is very good, for  $\Lambda > 1$ ,  $P$  approaches unity. Note that the description above is for a two level system but has been formulated for  $N$  equally spaced levels [77].

Considering an atom interacting with a static B-field, e.g., a quadrupole configuration  $\mathbf{B}_{\text{dc}}(\mathbf{r}) = \alpha(x\hat{\mathbf{e}}_x + y\hat{\mathbf{e}}_y - 2z\hat{\mathbf{e}}_z)$ , and an rf-field,  $\mathbf{B}_{\text{rf}}(t) = B_{\text{rf}}\hat{\mathbf{e}}_z \sin(\omega_{\text{rf}}t)$ , oscillating at  $\omega_{\text{rf}}$  with amplitude  $B_{\text{rf}}$ . The rf-field will be resonant with the atom at the location where  $\hbar\omega_{\text{rf}} = |g_{\text{F}}\mu_{\text{B}}|\mathbf{B}_{\text{dc}}(\mathbf{r})|$ , or the rf-field frequency is same as the Larmor frequency  $\omega_{\text{L}}$ .  $\omega_{\text{L}}$  is the separation between the adjacent magnetic sublevels, and if we work with a quadrupole field where the energy increases linearly, the spatial detuning from the rf resonance at an arbitrary position  $\mathbf{r}$  can be written as:

$$\delta(\mathbf{r}) = \omega_{\text{rf}} - \omega_{\text{L}}(\mathbf{r}) \quad (2.19)$$

Next, assuming that the dc field defines the local quantization axis (spin  $z$  axis), the Hamiltonian for an atom at rest in the presence of the rf-field and dc magnetic field is given by:

$$H(\mathbf{r}) = \frac{g_{\text{F}}\mu_{\text{B}}}{\hbar} (|\mathbf{B}_{\text{dc}}(\mathbf{r})|\hat{F}_z + \mathbf{B}_{\text{rf}}(\mathbf{r}, t) \cdot \hat{\mathbf{F}}) \quad (2.20)$$

where  $\mathbf{B}_{\text{rf}}(\mathbf{r}, t)$  is the spatially varying rf-field amplitude and  $F$  is the total atomic angular momentum. If we set the polarization of the rf-field to be linear, the Hamiltonian then becomes:

$$H(\mathbf{r}) = \frac{g_{\text{F}}\mu_{\text{B}}}{\hbar} |\mathbf{B}_{\text{dc}}(\mathbf{r})|\hat{F}_z + \frac{g_{\text{F}}\mu_{\text{B}}}{\hbar} |\mathbf{B}_{\text{rf}}^{\perp}(\mathbf{r})| [\hat{F}_+ \exp(\mp i\omega_{\text{rf}}t) + \hat{F}_- \exp(\pm i\omega_{\text{rf}}t)] \quad (2.21)$$

where  $\hat{F}_+$  and  $\hat{F}_-$  are the raising and lowering operators, equal to  $\hat{F}_{\pm} = \hat{F}_x \pm i\hat{F}_y$ , and  $\mathbf{B}_{\text{rf}}^{\perp}(\mathbf{r})$  is the rf-field component perpendicular to the local dc B-field. These extra terms, i.e.  $\mathbf{B}_{\text{rf}}^{\perp}(\mathbf{r})$ ,  $\hat{F}_{\pm}$ , and the factor of two in the second part of the Hamiltonian appear because in the rotating wave approximation the counter-rotating terms are dropped [78]. The positive and negative signs correspond to the sign of the Landé  $g$ -factor ( $g_{\text{F}}$ ). Now changing the frame to the rotating rf-field, at  $\omega_{\text{rf}}$  with the same local basis, result is:

$$H(\mathbf{r}) = \pm (-\delta(\mathbf{r})\hat{F}_z + \Omega_0(\mathbf{r})\hat{F}_x) \quad (2.22)$$

where rf-field Rabi frequency is equal to,  $\Omega_0(\mathbf{r}) = (g_{\text{F}}\mu_{\text{B}})/(2)|\mathbf{B}_{\text{rf}}^{\perp}(\mathbf{r})|$ , and is given only by the orthogonal component of rf-field to the local static B-field. The rf-dressed adiabatic potential is then obtained by diagonalising Eq. 2.22 along the quantization axis set the dc field, gives  $H(\mathbf{r}) = \Omega(\mathbf{r})\hat{F}_{z'}$ , where  $z'$  is the new dressed basis for the atoms. The generalized Rabi frequency takes the form,  $\Omega(\mathbf{r}) = \sqrt{\delta(\mathbf{r})^2 + \Omega_0^2(\mathbf{r})}$ . The rf

dressed adiabatic potential is of the form:

$$V_{\text{rf}}(\mathbf{r}) = m'_F \hbar \Omega(\mathbf{r}) = m'_F \hbar \sqrt{\delta(\mathbf{r})^2 + \Omega_0^2(\mathbf{r})} \quad (2.23)$$

where  $m'_F$  is a label in the adiabatic basis, and they also take all the values from  $-F$  to  $+F$ . The shape of this trapping potential is quasi-harmonic, in the sense that near the trap center it is harmonic and for higher energies the potential is linear (see Fig. 2.9c). The case above is for the linear polarization of the rf-field, another approach would be to consider linear rf as the sum of two circular components, i.e.  $\sigma_+$  and  $\sigma_-$ . In the RWA, one neglects the terms with the wrong sense of rotation, which is given by  $g_F$ . Therefore, in Rb87, each manifold is coupled only by either  $\sigma_+$  or  $\sigma_-$  polarised rf-fields. As a consequence, if the field is linearly polarised each manifold is dressed with a Rabi frequency that is "half" of the total Rabi frequency of the linearly polarised rf-field.

### 2.3.3 TAAP rings

Time-averaged adiabatic potentials (TAAP) are generated by a combination of a dc magnetic quadrupole field, strong radio-frequency (rf) fields and low frequency modulation fields [53]. TAAP is a time-averaged version of the rf-dressed adiabatic potential, similar to the case of TOP trap. TAAPs can be used to create a large variety of neutral atom trapping geometries, e.g., rings, double wells, pancakes, array of cigars, and more. Another key feature of TAAPs is that the potential is extremely smooth making them an ideal candidate for applied and fundamental studies. This thesis work is based on the ring-shaped waveguides and half-moon shaped traps (tilted rings).

Let's begin with the rf-dressed adiabatic potential. We know that the frequency and polarization of the rf-field defines the spatial extent and shape of the rf dressed potential, respectively [79, 80]. The amplitude of the rf-field is set such that the probability for an atom to remain in the dressed state is close to one [81]. If a linearly polarized rf-field is applied to a dc quadrupole trap, in the direction of the quadrupole strong axis, the rf coupling will be maximum in a circle in the radial plane. The gravitational acceleration does not allow the atoms to stay in this coupling region, and they fall at the bottom of the egg-shell isopotential surface. The addition of a vertical modulation field lifts the rf potential up and down, or the time-averaging provides axial confinement forming a ring waveguide. The frequency of the modulation field is chosen between the Larmor and the trapping frequency,  $\omega_{\text{trap}} \ll \omega_{\text{bias}} \ll \omega_L$ . This is to ensure that the modulation field does not affect the physical motion of the atoms and atomic spins can follow the spatially varying B-field adiabatically (negligible atomic spin depolarization).

### Flat ring waveguides

We create a flat ring-shaped TAAP by using dc quadrupole field, linearly polarized rf-field, and a linearly polarized modulation field. Let's assume that the strong axis of the quadrupole field is along the gravity axis ( $z$ ), and the orientation of the rf and modulation field is along the  $z$ -axis. The total B-field of a ring waveguide can be written as:

$$\mathbf{B} = \alpha \begin{pmatrix} x \\ y \\ -2z \end{pmatrix} + B_m \sin \omega_m t \begin{pmatrix} 0 \\ 0 \\ 1 \end{pmatrix} + B_{\text{rf}} \sin \omega_{\text{rf}} t \begin{pmatrix} 0 \\ 0 \\ 1 \end{pmatrix}, \quad (2.24)$$

where  $\alpha$  is the quadrupole gradient,  $B_m$  and  $B_{\text{rf}}$  are the modulation and rf-field amplitudes, respectively.  $\omega_m$  and  $\omega_{\text{rf}}$  are the oscillation frequencies of the modulation and rf-field, respectively. Let's go through in steps to examine the effect of the modulation and rf term on the quadrupole potential, first, I give the instantaneous picture. Since the frequency of the modulation field is much lower than the Larmor and faster than the timescale related to the motion of trapped atoms, it will only displace the quadrupole up and down. The instantaneous position of the quadrupole center along the  $z$ -axis will become,  $z_0(t) = (B_m/2\alpha) \sin(\omega_m t)$ . A factor of two because the magnetic gradient is twice in the  $z$  direction than in the radial plane. The Larmor frequency will also become time-dependent, in cylindrical coordinates, is:

$$\omega_0 = \omega_L \sqrt{\rho^2 + 4[z - z_0(t)]^2} \quad (2.25)$$

where  $\rho = \sqrt{x^2 + y^2}$ , and  $\Omega_L$  is the Larmor frequency in a dc quadrupole trap. The addition of the rf-field (third term in Eq. 2.24) will *dress* the atoms, and the instantaneous rf-dressed modulated-quadrupole potential can be rewritten, from Eq. 2.23:

$$V_m(\rho, z, t) = m'_F \hbar \sqrt{[\omega_0(\rho, z, t) - \omega_{\text{rf}}(t)]^2 + \Omega_1(\rho, z, t)^2} \quad (2.26)$$

where  $\Omega_1$  is the new time dependent Rabi frequency. The rf Rabi frequency varies spatially and it is maximum when the modulated-quadrupole field is orthogonal to the rf-field. Next, we will see how the time variation of the fields affect the stability of the ring trap and, in turn the atoms trapped in a ring centered on the origin. It is clear from the Eq. 2.26 that it is possible to have a stable isopotential circle around the center when  $\omega_0 = \omega_{\text{rf}}$ , for  $\rho = \rho_0$ , and  $z = 0$ . This conditions means that the Larmor frequency  $\omega_0$  will oscillate at twice the  $\omega_m$ , and hence the potential will not be static. A solution is to modulate the rf frequency, synchronized with the modulation. The time-dependent

rf-field frequency is then:

$$\omega_{\text{rf}}(t) = \omega_{\text{rf}}^0 \sqrt{1 + \beta^2 \sin^2(\omega_m t)} \quad (2.27)$$

where we call  $\beta$  the modulation index, is,  $\beta = (g_F \mu_B B_m) / (\hbar \omega_{\text{rf}})$ .  $\beta$  simply tells the extent of vertical up-down compared to the rf-field resonance. With this, we can almost get a stable ring of radius  $\rho_0 = (\hbar \omega_{\text{rf}}) / (g_F \mu_B \alpha)$ . I will assume that the rf-field Rabi frequency is constant over the extent of the rf resonance surface. However, due to the oscillation of the local B-field by the modulation, the Rabi frequency ( $\omega_1$ ) also changes in time (relative orientation between the rf and dc field changes). This can be avoided by modulating the rf-field amplitude, in a way that,

$$B_{\text{rf}}(t) = B_{\text{rf}}^0 \sqrt{1 + (2\beta \cos(\omega_m t))^2} \quad (2.28)$$

This ensures that the rf-field Rabi frequency is constant in a circle, i.e. at the bottom of the ring and will oscillate in other locations. Next, we put the two new modified terms, i.e. the rf-field and the rf-frequency into the Eq.2.26 and expand the potential around, first,  $z = 0$  and  $\rho = \rho_0$ , and then in the axial direction with  $\rho = 0$ . The integration of the potential over one cycle of the modulation field frequency gives the time-averaged ring potential, and the ring trapping frequencies: We tune the second harmonic to zero, which results in the following ring shaped potential

$$V_{\text{ring}}^{\text{av}}(r, z) = \hbar \Omega_0 + \frac{1}{2} m \omega_r^2 (r - R)^2 + \frac{1}{2} m \omega_z^2 z^2 \quad (2.29)$$

$$\omega_r = \omega_0 (1 + \beta^2)^{-1/4} \quad (2.30)$$

$$\omega_z = 2\omega_0 \sqrt{1 - (1 + \beta^2)^{-1/2}} \quad (2.31)$$

where  $\omega_0 = (m_F g_F \mu_B \alpha) / (m \hbar \Omega_0)^{1/2}$ , is the radial trapping frequency of the rf-dressed potential with no modulation field present and  $R$  is the ring radius. A circularly polarized rf can also be used to make the ring, only that it modifies the rf coupling strength at the location where the atoms are trapped and should have the right handedness according to the sign of the hyperfine  $g_F$  factor.

### Tilted ring traps

A tilted ring trap can simply be created by adding a small amplitude rf-field or a modulation field in the radial plane. The ring is tilted in a direction given by the relative phase between the vertical and the radial rf (modulation) field. The modulation

field tilt acts like a gravitational tilt, and does not act on different spins differently. It only deforms the ring waveguide potential at a given angle. However, a small amplitude elliptic rf-field gives a state dependent tilt since one circular polarization only couples with atoms in a certain hyperfine level (sign of  $g_F$  factor). The modified ring potential takes the form, extension of Eq. 2.29:

$$V_{\text{ring}}^\delta(r, \phi, z) = \hbar\Omega_0 + \frac{1}{2}m\omega_r^2(r - R)^2 + \frac{1}{2}m\omega_z^2z^2 - \frac{\delta}{2}mgR \cos(\phi - \phi_0) \quad (2.32)$$

where the radial and the axial trapping frequencies are of approximately the same as in the ring waveguide for small tilt angles. The factor of 2 in the last term comes from the fact that the magnetic gradient is twice as strong in the vertical direction than in the radial plane, and thus the curvature at the bottom (eq. 2.33).  $\phi_0$  is the angle of the tilt and  $\delta$  is the tilt amplitude (radial field strength). The azimuthal trapping frequency of a tilted ring, is:

$$\omega_\phi = \sqrt{\frac{\delta g}{2R}} \quad (2.33)$$

which is very much like a tilted pendulum oscillation frequency. More details on the state dependent (rf), independent (modulation), and arbitrary tilts (rf + modulation) can be found in [61].

## 2.4 Bose-Einstein condensation

By the use of trapping and cooling techniques explained in the sections above, atoms can be cooled down to very low temperatures near absolute zero (recent numbers in the picoKelvin regime). During the cooling process, both the atom number and temperature drops. If the temperature drop is higher than the particle number loss, the phase space density increases, i.e. the atomic de Broglie wavelength increases and the atoms come closer. The point when the atomic quantum wavelength becomes equal to the mean interparticle separation, the tiny atomic waves overlap and form a giant quantum matter, called Bose-Einstein condensate (BEC). The atoms remain no longer distinguishable, and they are described by one single wave function, since the majority of the atoms occupy the lowest quantum energy state. The size of this quantum object goes up to tens of micrometers and can be easily imaged with a CCD camera making it an excellent candidate to unfold the mysteries of the quantum world. In the two sections below, I present general formalism for the trapped ideal and weakly interacting Bose gas.

## Ideal Bose gas in a trap

First, let's consider the ideal gas case where the interaction between the Bosonic atoms is absent, like in a classical ideal gas, and the atoms only interact via perfect elastic collisions. However, this is not a very practical scenario since the atoms do have some level of interaction unless tuned. For both of the cases above, a more detailed description can be found in [82]. If we put some non-interacting Bosonic atoms in a confining potential  $V(r)$ , the average occupation of the single particles states  $\epsilon_k$  at thermal equilibrium is given by the Bose distribution function:

$$n_k = \frac{1}{\exp(\epsilon_k - \mu) / k_B T - 1} \quad (2.34)$$

where  $\mu$  is the chemical potential of the gas, at a fixed temperature  $\mu$  is constant by the conservation of number of particles,  $N = \sum_k n_k$ .  $\mu$  has a large and negative value for the higher temperatures, it approaches  $\epsilon_0$  as the temperature drops. At a certain critical temperature,  $\mu$  takes the value of the ground state eigenenergy, i.e.  $\mu = \epsilon_0$  and majority of the atoms occupy the ground state of the system. This phenomenon of macroscopic occupation of the ground state is called Bose-Einstein condensation. If we split the number of atoms in the ground ( $N_0$ ) and upper excited states ( $N_{th}$ ) as,  $N = N_0 + N_{th}$ , the number of atoms in the thermal state is then:

$$N_{th} = N - N_0 = \int_0^\infty \frac{\rho(\epsilon) d\epsilon}{\exp(\epsilon_k - \mu) / k_B T - 1} \quad (2.35)$$

where  $\rho(\epsilon)$  is the density of states for the gas in an external potential  $V(r)$ , given by:

$$\rho(\epsilon) = \frac{2\pi(2m)^{\frac{3}{2}}}{(2\pi\hbar)^3} \int_{v < \epsilon} dr \sqrt{\epsilon - V(r)} \quad (2.36)$$

The spatial density distribution of the atom cloud can be found by the normalization of the particle number conservation and the two equations above, result is:

$$n(r) = \frac{1}{\lambda_{th}^{\frac{3}{2}}} g_{\frac{3}{2}}(\tilde{z} e^{-V(r)/k_B T}) \quad (2.37)$$

where  $\lambda_{th}$  is the de Broglie wavelength of the atoms,  $\tilde{z}$  is the fugacity term, and  $g_\alpha$  is a poly-logarithm function. The thermal wavelength of the atom is,  $\lambda_{th} = \sqrt{(2\pi\hbar^2)/(mk_B T)}$ , clearly as the temperature drops wave nature of the atom is more pronounced. The phase transition to BEC occurs when the value of the product  $n(0)\lambda_{th}^3$ , phase space density reaches the value 2.612. In the experiments where a



harmonic potential is used commonly, the density of states is given by:

$$\rho(\epsilon) = \frac{1}{2} \frac{\epsilon^2}{\hbar\bar{\omega}} \quad (2.38)$$

where  $\bar{\omega}$  is the geometric mean of the trapping frequencies. We can then find the  $N_{th}$  by putting the value of  $\rho(\epsilon)$  from above in the Eq. 2.35, and find:

$$N_{th} = g_3(1) \left( \frac{k_B T}{\hbar\bar{\omega}} \right)^3 \quad (2.39)$$

and the critical temperature can be derived from the equation above by the making the ground state occupation to zero, or  $N = N_{th}$ . The critical temperature for an ideal gas has the form:

$$T_c = \frac{\hbar\bar{\omega}}{k_B} \left( \frac{N}{g_3(1)} \right)^{\frac{1}{3}} \approx 0.94 \frac{\hbar\bar{\omega}}{k_B} N^{\frac{1}{3}} \quad (2.40)$$

## Weakly interacting Bose gas in a trap

The second case, unlike the one above, is when the atom are weakly interacting. In the routine ultracold atoms experiments where alkali atoms are used, the nature of the interaction is weakly repulsive, which is utilized in the collision-assisted cooling process. In the low temperature regime of the atoms, elastic collision between the atoms fall in the s-wave scattering limit, and the scattering process can be described by a pseudo potential [83]:

$$V(\mathbf{r} - \mathbf{r}') = g\delta(\mathbf{r} - \mathbf{r}') = \frac{4\pi\hbar^2 a}{m} \delta(\mathbf{r} - \mathbf{r}') \quad (2.41)$$

where  $g$  is the interaction parameter. We see that the potential is proportional to the scattering length  $a$ , for  $^{87}\text{Rb}$  the sign of the scattering length is positive, and hence the interaction repulsive. The value of  $a$  is,  $198.98(4)a_0$  [84], where  $a_0$  is the Bohr's radius, then  $a = 57.7 \times 10^{-10}$  m. The s-wave approximation is valid for  $|R_0/\lambda_{th}| \ll 1$ , where  $R_0$  is the psuedo potential range, given by,  $R_0 = (C_6 m / (2\hbar^2))^{\frac{1}{4}}$ . Again, for  $^{87}\text{Rb}$  the value of  $R_0$  is 7.3 nm, obtained by the values of mass and value of van der Waals coefficient  $C_6$  [85]. Now, if we convert  $R_0$  into temperature, we get 1 mK which is an upper limit for the applicability of the s-wave approximation. As the temperature of the gas goes higher, d-wave scattering starts to matter and increases the elastic collisional cross section of the atoms. If the correlation between the atoms is on a much smaller scale than of the atom cloud size, mean field theory can be used to describe the properties of the gas [86]. In the regime where the temperature of gas goes below  $T_c$ , macroscopic occupation of the ground state occurs and single wave function ( $\phi(r)$ ) of the ground state component is

given by the Gross-Pitaevskii equation (GPE),

$$\left( -\frac{\hbar^2 \Delta^2}{2m} + V(\mathbf{r}) + g|\phi(\mathbf{r})|^2 \right) \phi(\mathbf{r}) = \mu\phi(\mathbf{r}) \quad (2.42)$$

the first term corresponds to the kinetic energy, second the external potential and the last term represents the interaction. The spatial density of the ground state part (BEC) is given by,  $n(\mathbf{r}) = |\phi(\mathbf{r})|^2$ . For the case of high atomic density, the mean field interaction takes over the kinetic energy and then the first term can be dropped in the above equation. It is called Thomas-Fermi approximation, and the distribution becomes,

$$n(\mathbf{r}) = \frac{1}{g} [\mu - V(\mathbf{r})] \quad (2.43)$$

It is clear that the BEC spatial density depends on the profile of the confining potential and the repulsive mean field interaction. If we take a harmonic potential as a trap to confine the atoms, the shape of the spatial condensate density is an inverted parabola. Also,  $n(\mathbf{r})$  goes to zero when the confining potential energy is larger than the chemical potential. Using this approach, we get the Thomas-Fermi radius of the BEC as:

$$R_k = \frac{1}{\omega_k} \sqrt{\frac{2\mu}{m}} \quad (2.44)$$

where  $\omega_k$  is the harmonic trap frequency along a particular axis, out of three. To obtain the total number of atoms in the condensed phase, the condensate density, from Eq. 2.43, is integrated over the size of the cloud, given by:

$$N_0 = \int n(\mathbf{r}) d\mathbf{r} = \left( \frac{2\mu}{\hbar\bar{\omega}} \right)^{\frac{5}{2}} \frac{a_{ho}}{15a} \quad (2.45)$$

where  $a_{ho}$  is the ground state harmonic oscillator length, is  $a_{ho} = \sqrt{\hbar/m\bar{\omega}}$ . The same result also contains an expression for the chemical potential ( $\mu$ ) of the trapped Bose condensed gas. To give a number for  $^{87}\text{Rb}$  atoms, the ground state energy  $\mu$  is typically of the order of a few kHz, for e.g., in a TOP trap of  $\omega_r = (1/\sqrt{8})\omega_z = 2\pi \times 50 \text{ Hz}$  and containing  $10^5$  atoms,  $\mu$  is 1.2 kHz, or 56 nK.

## Chapter 3

# Experimental Setup

### 3.1 Lasers

In this section, I will describe the laser system of the BEC lab, used for the laser cooling and imaging of the atomic cloud. The different stages of the laser system can be divided mainly in four parts, 1) saturated absorption spectroscopy where the laser is locked to the cycling hyperfine transition of  $^{87}\text{Rb}$ , 2) first amplification stage, referred to as slave laser, 3) AOM distribution board where the laser frequency is shifted for different stages of the experiment cycle, and 4) the final amplification stage called tapered amplifier. More details on our saturated absorption spectroscopy setup can be found in the ref's [87, 88], and this part of the laser system will be referred to as Master laser. Below I describe the working of last three stages of the laser system which I worked on.

#### 3.1.1 Injection-locked slave laser

After locking the diode laser light to the  $^{87}\text{Rb}$  transition  $|5S_{1/2}, F = 2\rangle \rightarrow |5P_{3/2}, F = 1/3\rangle$  in the Master laser setup, the laser beam is transported using a single-mode optical fibre to the slave setup. This is the first amplification stage of the laser system. Here the power is amplified via the injection locking method [89]. Fig 3.1 shows the schematic diagram of the slave laser setup. First, the master beam is coupled to the slave diode as shown in the figure, and by tuning the polarization of the beam using the first  $\lambda/2$  waveplate maximum coupling to the diode is achieved. An optical isolator (OI) is used to prevent any back injection of the amplified beam back into the diode. The diode box contains a Fabry-Perot (FP) diode, center wavelength at 780 nm, and mounted on an Al cylindrical mount. The diode is temperature stabilized using a Peltier element, and a thermistor attached to the mount.

A very small portion of the output is deflected by a wedge plate (WP) and directed to a Fabry-Perot cavity (confocal configuration). This home built cavity allows to monitor the modes of the beam. The main line is finally coupled into a single-mode optical fibre which takes the light to the AOM distribution board. The injection beam from the Master laser has a power of  $\sim 3\text{mW}$  power, and the maximum power which can be derived from the slave diode (Panasonic LNC728PS01WW) is about 200 mW. Typically the diode is not operated at the maximum current to derive the maximum power. Working at high currents reduces the locking range of the diode and needs a lower working temperature (via the Peltier element) which increases the risk of condensation. The diode normally operates at around 120 mA and we get sufficient power to feed the tapered amplifier and imaging lines.

In order to avoid the use of a repumper laser, a microwave (mw) radiation at 6.8 GHz is injected electrically to the diode. This mw injection creates side-bands at 6.8 GHz next to the optical frequency given by the Master laser. In our setup, the maximum mw power which can be injected to the diode is 37 dBm at  $50\ \Omega$ . The lower left corner of Fig. 3.1 shows a bias-tee which combines the AC (mw) and DC (diode normal operation) currents which is then injected to the diode. For the experiment, three different mw frequencies can be generated for their use at different stages. These stages are, MOT loading (2D-MOT and 3D-MOT share the same frequency), compressed MOT (CMOT), and the imaging.

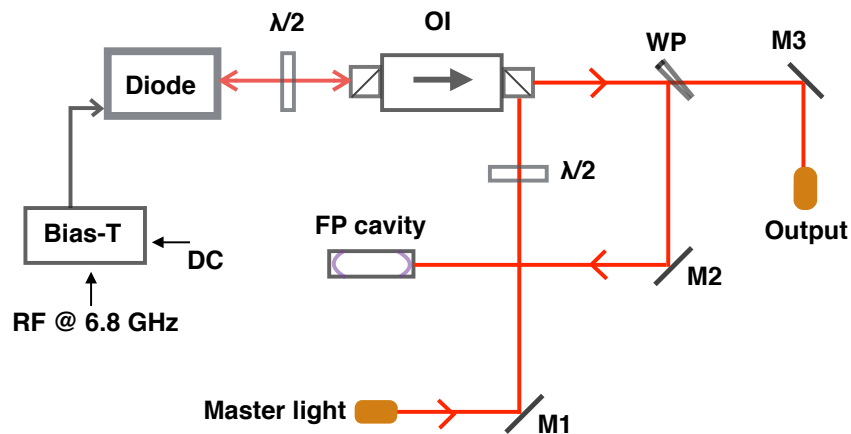


Figure 3.1: Schematic of the slave laser setup.

### 3.1.2 AOM distribution board

The output of the slave laser is transported to the AOM distribution board where it is divided into four different paths. The main purpose of this stage is to generate beams

with different frequencies, to be used at different stages of the experiment. Fig. 3.2 shows a schematic of the AOM setup. The laser beam frequency coming from the slave laser (Master) is 211.8 MHz down from the laser cooling transition of  $^{87}\text{Rb}$ . In order to laser cool and trap the atoms in a magneto-optical trap, the frequency of the beam needs shifting upwards by 211.8 MHz. The first AOM (A1) shifts the laser beam frequency up by 60 MHz and the first order is then directed to the next three AOMs. The zeroth mode of A1 is directed via a mirror to a different path for various test purposes. The beams going into the AOMs A1, A2, and A3 are focused with a 30 cm lens (CL) with their focus at the center position of the AOM(s). The beam is focused to improve the diffraction efficiency. After the single pass through the AOM, the beam passes through a  $\lambda/4$  waveplate and reflected back from a concave mirror (CM). The use of a concave mirror ensures the overlap of the input and reflected beams. The reflected beam then again passes through the AOM and its frequency is shifted by the same amount (in the same direction and here upwards). The zeroth order of the AOM goes to a beam block (BB). The output of the different ports is coupled to single mode polarization maintaining fibres, for their use in the experiment. Just before the fibre, mechanical electromagnetic shutters (MS) are installed to block the beam completely with rise(fall) time of about 1.5 ms.

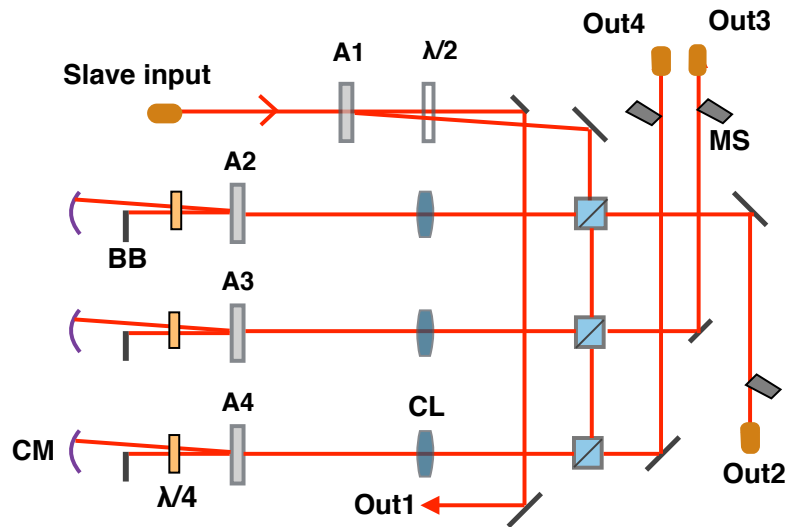


Figure 3.2: The layout of the AOM distribution board.

The center frequency of the AOM A4 is at 115 MHz and thus shifts the laser beam frequency upwards by 230 MHz, in this double pass configuration. The output of this line is transported to the tapered amplifier setup. To make the laser beam resonant with the laser cooling transition, the laser frequency is shifted downwards in the taper setup. This two-step shifting is done to achieve a large range in the frequency ramp on the

negative detuning side, for the efficient compression of the atomic cloud at the CMOT stage. AOMs A3 and A4 has their center frequencies at 75.5 MHz and they are used for the two absorption imaging lines i.e. horizontal and vertical. The lines A3 and A4 are transported directly to the experiment for the imaging. Both the amplitude and frequency of the AOMs can be programmed (switched on/off and ramped) as needed. Before each of the output fibre, the beam has 2 to 3 mW of optical power.

### 3.1.3 Tapered amplifier

This stage of the laser system does the final amplification of the laser beam before it is delivered to the experiment. The output of the tapered amplifier is transported to the experiment for its use in the 2D-MOT and 3D-MOT. The line A4 of the AOM distribution board acts as a seed for the tapered amplifier (TA) setup. Fig. 3.3 shows the different elements of our TA setup. The injection beam of power 1.1 mW is coupled to the TA chip after it passes through an optical isolator, a cylindrical lens ( $f=50$  mm), and finally through an aspheric lens ( $f=4.5$  mm). This is a double pass amplification configuration, the beam after its first amplification is injected back to the diode by the use of a mirror M5. A small portion of the beam is collected with a wedge plate (WP) onto a photodiode, to monitor the power of the beam which is injected back to the chip. This is done to ensure the maximum injection to the chip (here 50 mW) and prevent any damage. TA chip is mounted on a Copper base which is temperature stabilized using a Peltier element and a thermistor.

The output of the TA then passes through an AOM which shifts the laser beam frequency downwards by 80 MHz and makes the beam resonant with the laser cooling transition of  $^{87}\text{Rb}$ . The zeroth order of the AOM is blocked with a beam dump (BD). The first order is coupled into a polarization maintaining single-mode optical fibre, which transports the beam to the experiment. With an injection of 1.1 mW the optical power in the first mode after the AOM is about 700 mW. The coupling efficiency at the output fibre is about 40%, and  $\sim 300$  mW of optical power reaches the experiment. With this total power, the 3D-MOT beams have a saturation intensity of about  $3 \times I_{sat}$ . In the experiment, this power is sufficient to load about  $10^9$  atoms into 3D-MOT from the 2D-MOT in a loading time of 5 s. Fig. 3.4a) shows the dependence of injection power (amplified optical power to the experiment) versus the number of atoms in a quadrupole trap after RF evaporation. Since the number of atoms loaded into the magnetic trap is proportional to the number of atoms loaded in the 3D-MOT, is a study of saturation in the amplification of the TA. After 0.8 mW of injection, the number of atoms loaded into the trap reaches a steady state. The injection power is then kept fixed

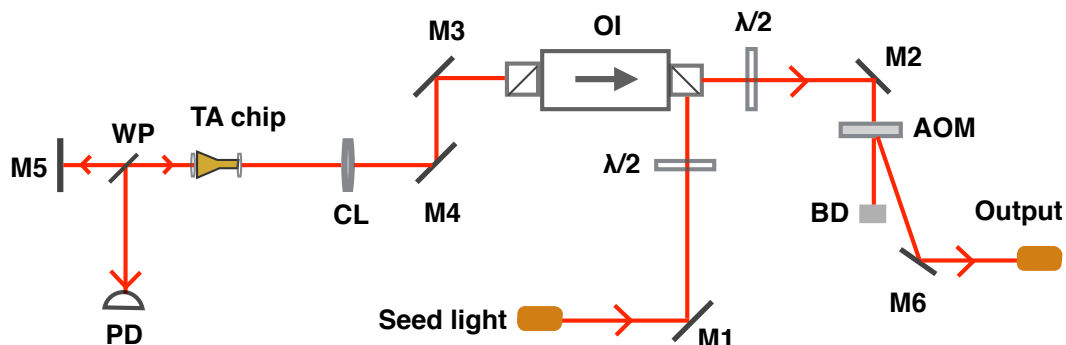


Figure 3.3: Schematic of the tapered amplifier setup.

at 1.1 mW. Fig. 3.4b) shows the shot to shot stability in the number of atoms loaded into the magnetic trap (3D-MOT) versus the injection power to the TA. Around the saturation in the injection to the TA, the number stability improves significantly. It demonstrates the stable working of the TA chip in terms of the injection power.

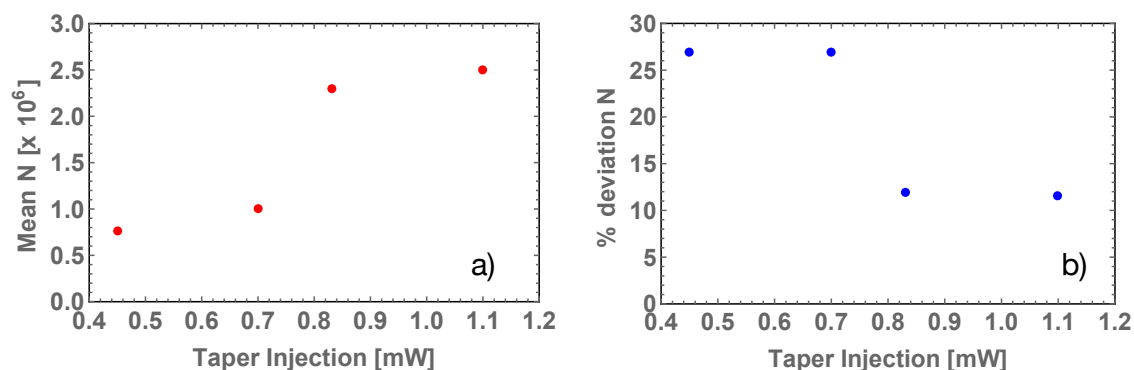


Figure 3.4: a) Number of atoms in the quadrupole trap against the injection power to the TA. b) The stability in the number of atoms as a function of injection power to the TA. Each data point comes from a measurement window of about 20 minutes.

### 3.1.4 MOT setup

The output of the TA and the two imaging lines of the AOM distribution board is transported using polarization maintaining single-mode optical fibres to the experiment. TA output is taken to the MOT distribution board where the beam is divided into different ports for its use in the 2D-MOT, 3D-MOT, and as a push beam. First stage is the MOT distribution board where the input from TA is divided in nine using polarizing beam splitters (PBS), more details in [88]. Among the nine, six beams are used for the 3D-MOT, two for 2D-MOT and one acts as a push beam which

transports a cold atomic beam from 2D-MOT to 3D-MOT. With the use of  $\lambda/2$  waveplates mounted before each of the PBS's, the beam power can be tuned precisely. The power ratio is tuned between the 2D-MOT and 3D-MOT, and between the counter-propagating beams of the two 3D-MOT. The ratio between the two 2D-MOT beams i.e. vertical and horizontal can also be tuned with the help of a  $\lambda/2$  waveplate. A detailed description of the 2D-MOT and 3D-MOT can be found in the reference [87].

## 2D-MOT

The atoms in a two-dimensional MOT (2D-MOT) are cooled and trapped only along the two axis, hence the name 2D-MOT. 2D-MOT acts as a source of slow atoms for the 3D-MOT and increases the atom loading rate drastically. The loading of 3D-MOT is done by the use of a near-resonant collimated laser beam (push beam). In chapter 1, I explained the first laser cooling experiments where an atomic thermal beam was slowed down by a laser beam. Here, the same idea applies, i.e., the atoms moving towards the push beam are slowed down and pushed away from the source. Since we only have one beam, the atoms are decelerated and carried with the push beam. The push beam is aligned such that it overlaps with the very elongated 2D-MOT cloud in the longitudinal direction. The beam does not go through the 3D-MOT center but a few mm (size of the 3D-MOT) away, to keep the radiation pressure balance of the 3D-MOT beams.

In the experiment, 2D-MOT setup needs a magnetic quadrupole field, two counter-propagating sheet-like laser beams, and an atom cell. The 2D-MOT cell (made of pyrex) is maintained at a pressure of  $10^{-7}$  torr, and 3D at  $10^{-11}$  torr. The 3D and 2D vacuum chambers are separated by a  $550 \mu\text{m}$  hole, maintains the differential pressure between the two chambers. A detailed description of both the vacuum systems is in the reference [87]. The laser beams are transported from the MOT distribution board to an Al mount, where by the use of spherical and cylindrical lenses the beams are expanded and collimated to a dimension of  $150 \text{ mm} \times 20 \text{ mm}$ . The two beams go through the 2D-MOT cell and reflected by prisms to create a retro-reflected configuration. The vertical beam is created by its reflection from a gold coated mirror above the 2D-MOT chamber, aligned at  $45^\circ$  from the vertical. Each beam has about 20 mW of optical power and the push beam carries about 10 mW, after the fibre. The two MOT's have the same frequency for the cooling and repumping, the cooling line -14 MHz red-detuned and repumper on resonance. The magnetic coils have a rectangular shape, four coils are installed each orthogonal to each other giving a magnetic gradient of 15 Gpcm. In the 3D-MOT, we get a flux of about  $10^8$  atoms/s when loaded from the 2D-MOT.



## 3D-MOT

Let us look at the two components of the 3D-MOT separately, the laser beams and the magnetic quadrupole field. The six laser beams are transported via single mode PM fibres from the MOT distribution board to six different MOT beam collimators. We use tube mounts from Thorlabs for the fibre adapter, collimation lens, and the quarter wave plate (QWP), are the components of the collimator. All the beams in the experiment are at a height of 5 cm. The collimation lens is a plano-convex type with a focal length of 10 cm. The QWP used to create right and left circularly polarized light has half an inch diameter. The beam after the collimator has 1 inch diameter. The intensity in each of the MOT beams is about three times the saturation intensity ( $I_s = 1.65\text{mW}/\text{cm}^2$ ). The detuning from the resonance, typically, is -14 MHz and the repumper on resonance F=1 to F=2 hyperfine level. For the 3D-MOT, we run the quadrupole coils at 6 A, giving 6 G/cm magnetic field gradient, powered by Delta Elektronika (DE) ES 015-10.

## 3.2 Coils for the magnetic trapping

### 3.2.1 Quadrupole coils

The magnetic quadrupole field is generated by two water-cooled hollow copper wires in anti-Helmholtz configuration, design in [87]. The same coils are connected with two power supplies for the operation of 3D-MOT and the magnetic trap. These two stages of the experiment need different current in the coils, or the magnetic field gradient. 3D-MOT typically needs up to 10 A, and the magnetic trap up to 300 A. We work with different magnetic traps created by the use of quadrupole coils, e.g., 1) quadrupole trap, and 2) TOP trap, 3) TAAP rings, 4) RF shell trap, and more. The different traps need different magnetic gradient along with rf-fields and/or the audio-frequency fields.

Fig. 3.5 shows a simple circuit diagram, the coils take input from two power supply units (PSU) from DE. The first PSU DE SM 15-400 can give a maximum output of 400 A at 15 V. The lower one goes up to 10 A at 15 V. After the PSU's, we have a box called *crap* which provides fast switching of the field when the trap is turned on/off. We do not draw the maximum current due to the additional resistance offered by this fast switch driver, reaches 310 A with the upper line. A fast switching is important because the atoms can not be transferred efficiently (no heating and atom number loss) from MOT to the magnetic trap if the switching time is slower than one trapping period. Also, when the trap is turned off the field should vanish quickly otherwise the sample will be

depolarized. The quadrupole field can be turned on and off on a timescale of less than  $100 \mu\text{s}$ .

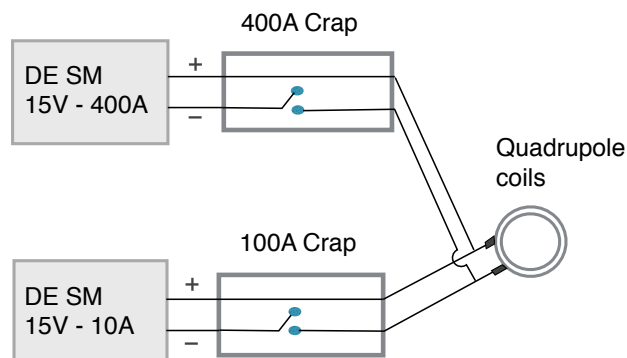


Figure 3.5: Quadrupole coil connection for the MOT and magnetic trap operation.

### 3.2.2 Modulation field coils

Three pairs of modulation coils in Helmholtz configuration are installed along all three lab frame axes. The horizontal pairs have a rectangular shape (X and Y), outer dimension  $20 \text{ cm} \times 24 \text{ cm}$  and the vertical coils (Z) are round, outer diameter 12 cm. The winding is done such that a different number of loops can be used. For the X, and Y coils, we can work with 1, 2, 4, 8 or 12 turns. Along the Z direction, we can create sound field with 1, 2, 4, 8, 12 or 28 number of loops. The modulation coils are in series with a set of capacitors and  $2 \Omega$  water-cooled resistor. The resistors tune the impedance of the circuit and thus helps in deriving the maximum output from the amplifier. The central frequency for all the resonators is tuned to 5.02 KHz. The sound file is created by mathematica in the wav file format and played by the audio card M-Audio 1010LT. The maximum sound field we can generate from the X and Y coils is up to 48 G, using Crown XLS 2000 amplifier (Impedance range  $2 \Omega - 8 \Omega$ ,  $650 \text{ W} @ 4 \Omega$ ). The Z coils generate a maximum field of up to 12 G when powered with an amplifier Cambridge Audio P500 (Impedance range  $6 \Omega - 16 \Omega$ ,  $55 \text{ W rms} @ 6 \Omega$ ).

The modulation coils are used for different purposes. X and Y modulation fields together with the quadrupole creates a TOP trap. To generate a TAAP ring waveguide, just the Z coils are used, and all three for the static and moving tilted ring traps. I also used the modulation coils in dc mode since they can give much higher amplitudes than the compensation coils, e.g., to load atoms into a flat ring. In the dc mode, the calibration for the X coil is  $4.54 \text{ G/A}$ , Y coil has  $4.49 \text{ G/A}$ , and  $2.94 \text{ G/A}$  for the Z coil, with full

windings used in all three. To test the alignment of the modulation coils with respect to our imaging system, I displaced a cold atomic cloud in the quadrupole trap by using X and Y coil fields, separately, in the dc mode. From the displacement of the cloud for different bias field amplitudes, I calculate the slope which gives a relative angle. The angles are  $1.1^\circ$  and  $1.6^\circ$  for X and Y coils, respectively. Fig. 3.6 shows the coils and field angles in the lab frame.

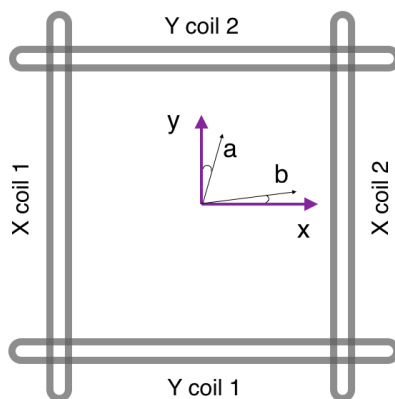


Figure 3.6: X and Y modulation field coils and the angles  $a$  and  $b$  corresponding to the dc field direction generated by these coils.

### 3.2.3 RF generation

This part describes the generation of the rf-field which is used to create rf-dressed adiabatic potentials and TAAPs. The rf resonator is a parallel LC circuit made of a single loop rectangular-shaped enameled Cu coil and polypropylene capacitors. The coil dimension is  $3 \times 7.5$  cm. The inductance of the rf resonator coil is about 400 nH. There are three rf resonators installed in the experiment, along the  $x$ ,  $y$ , and  $z$  axis. The  $x$  and  $y$  rf resonators have their resonance at 2.1 MHz ( $\omega_{\text{res}} = 1/\sqrt{LC}$ ) with a 15 nF capacitor in parallel. The bandwidth of these two resonators is  $\sim 230$  kHz. Fig. 3.7 shows a spectrum of  $x$  rf resonator taken with a vector network analyzer (Rohde & Schwarz ZVB8). The  $z$  rf resonator has its resonance at 2.55 MHz and with a bandwidth of  $\sim 150$  kHz, tuned by the use of a 30 nF capacitor in parallel with the inductor. All the rf circuits are powered with three different 30 W amplifiers (LZY-22+ Mini Circuits). The input to the amplifier comes from a function generator (DG1062 Rigol), operated in the amplitude modulation mode. For the rf-induced evaporation in the quadrupole and TOP trap, a different coil is used. It is a single loop antenna of diameter 25 mm and placed at a distance of about 6 cm from the atom cloud position. The coil is powered

with an rf amplifier (25A250A Amplifier research) which takes input from a Rigol function (DG1062 Rigol) generator in the frequency sweep mode.

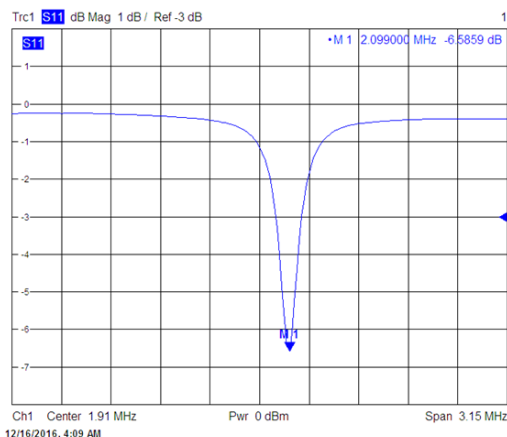


Figure 3.7: Spectrum of the  $x$  rf resonator taken with a vector network analyzer.

To test the precision and long term stability of our rf fields, I used a weak  $x$  rf field to tilt a ring potential filled with  $3 \times 10^5$  atoms at 470 nK temperature. The  $x$  rf,  $180^\circ$  out of phase with the  $z$  rf was switched on at various amplitudes and after 2 s hold time the cloud was absorption imaged. Fig. 3.8 shows the tilt of the ring potential, calculated from the atomic density imbalance around the ring potential. The data is fitted with a straight line and we find a slope of 2.6 (3) nK/mV. Also, the long term amplitude drift was tested by monitoring the rf amplitude needed to correct the mechanical tilt of the ring. There was no significant change in the value day to day. The error in the data comes from the short hold and the atom number variation shot to shot.

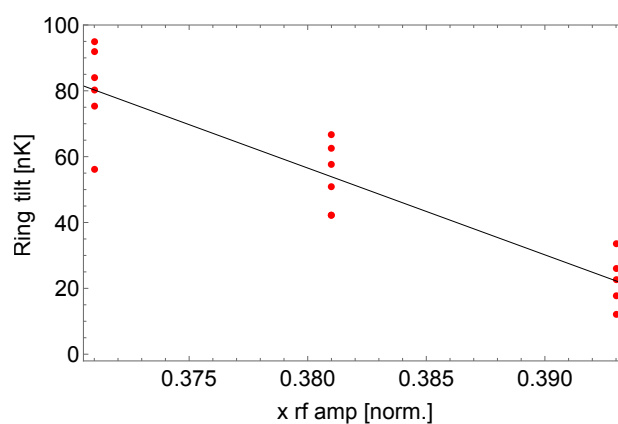


Figure 3.8: Tilt of the ring potential filled with ultracold atoms versus the  $x$  rf (in phase with  $z$  rf) amplitude.

### 3.2.4 Compensation coils

The compensation coils were built for different requirements in the experiment. First, matching of the MOT and magnetic trap (quadrupole or top trap) position in 3D, to transfer the atom cloud from MOT to the magnetic trap without heating or atom number loss. Second, adiabatic loading of BECs from the crossed dipole to a displaced ring trap. To do that, the ring potential was moved by one ring radius using the  $xy$  dc-bias fields. Third, cancellation of any stray dc B-field at the center of the trap where the atoms are, for spectroscopy experiments. We also load BECs from a crossed-dipole to the TOP trap, and the  $z$  compensation coil is used to match the two traps vertically.

Figure 3.9 shows the design of the compensation coils. There are two pairs along the  $x$  and  $y$  axis of the lab frame in the Helmholtz configuration, and one coil installed in the plane of the atoms which generates dc-bias field along the vertical direction. They are built in a way that different winding number can be chosen depending upon the amplitude of field needed, one can work with less windings for low noise operation. The winding numbers which can be used are, 2, 4, 8, 18, and 32. The coils are made of enameled copper wires of 1.8 mm diameter. The total resistance of one coil for the total number of windings, i.e. 62, is 2.51 Ohm. The frame onto which the coils are mounted is made of 2 mm thick Aluminum and 2.5 cm wide. The  $x$  and  $y$  compensation coil pairs generate 0.125 G of homogeneous field at the center of the coils for 1 A of current. The  $z$  coil has a calibration of 0.5 G/A.

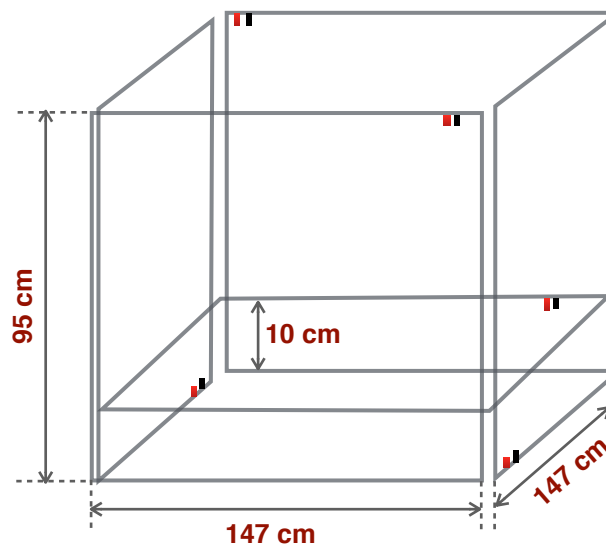


Figure 3.9: Schematic of the compensation coils, installed along all the three axis of the lab frame.

## 3.3 Optical dipole trap

### 3.3.1 Setup

In this section, I will describe the crossed-beam dipole trap setup, alignment of the dipole beams to the MOT and then to the magnetic quadrupole trap position, and the beam characterization. First, Fig. 3.10 shows the different parts of the crossed optical dipole trap setup. An optical breadboard was built to mount the laser head and other optics components. A fiber laser (ALS-IR-1064 Azur Light Systems) generates the dipole beam. The output of the laser head is a collimated beam of 1 mm diameter at 1064 nm wavelength, and maximum 20 W power. The beam first passes through the two AOM's (ATM – 803FB6 IntraAction Corp.) and is split into four distinct modes. The two AOM's take input from a function generator (DG4162 Rigol) amplified by the RF amplifiers (KU PA 006008 – 30 HY Kuhne Electronic, 62 to 78 MHz frequency range). We drive the function generator in the amplitude modulation (AM) mode, and thus the beam power in each of the four arms can be tuned precisely. First AOM (AOM-H) diffracts the incoming beam in the horizontal plane, operates at 78 MHz with 2 W of incident RF power. Second AOM (AOM-V) is placed vertically; sound wave propagates downwards and diffracts the beam vertically. AOM-V operates at 68 MHz with an input RF power of 2 W. The upper two modes after the vertical AOM (AOM-V) are used to make a crossed dipole trap. The beam height after the mirrors M3 and M4 is kept 5 cm throughout. The two dipole beams after M3 and M4 make an angle of  $17^\circ$ .

Since the beam diameter from the laser head is 1 mm, we built a Galilean beam expander to first get a larger size collimated beam and then focus at the trap center to achieve a smaller waist for atom trapping. The beam is expanded and collimated using two lenses, a diverging (L1:  $f = -200$  mm,  $D = 25.4$  mm) and a converging (L2:  $f = +500$  mm,  $D = 25.4$  mm) lens. The beam diameter after the Galilean expander increases to 2.7 mm, and with this we get a waist 68  $\mu$ m at the location of the atoms. The zero order of AOM-V, two beams pointing downwards is blocked using a beam dump (not shown in the scheme). The first order of AOM-V is used in the experiment. The first mirror M1 is used to correct the height of the beam after the science cell. Mirrors M3 and M4 direct the two beams towards the trap center, and they are used for the fine alignment of the beams. The final focusing of the beams is done by two plano-convex lenses – L3 and L4 each of focal length +25 cm, and diameter  $D = 12.7$  mm. The two beams after the science cell are blocked with beam dumps BD1 and BD2.

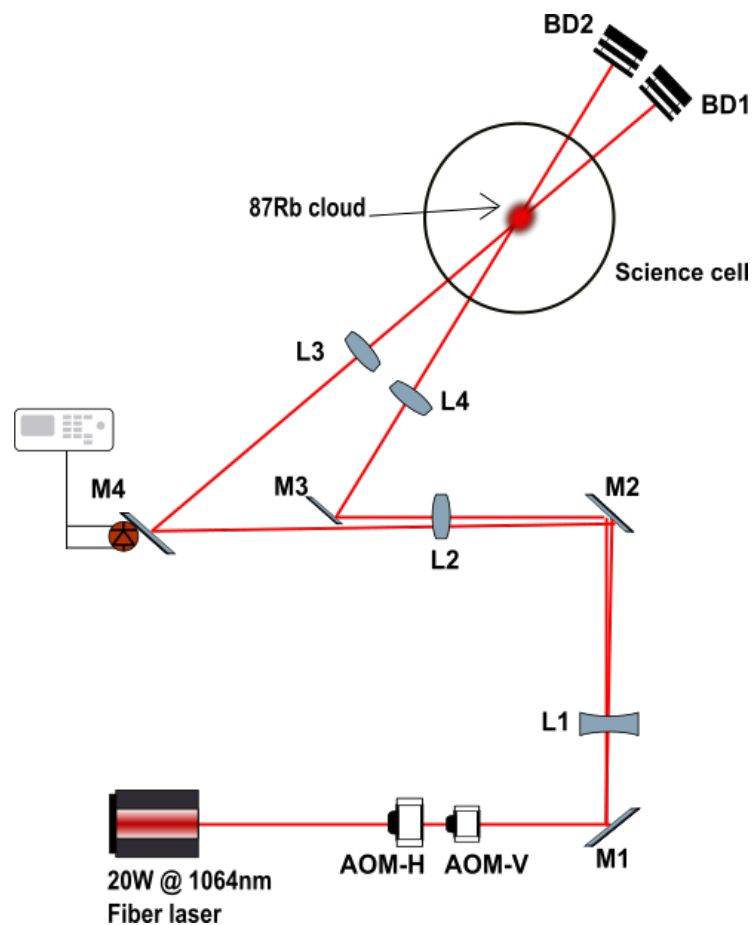


Figure 3.10: A layout of the crossed-beam optical dipole trap setup of the BEC experiment.

### 3.3.2 Dipole beams alignment and characterization

After installing the dipole trap setup, we aligned the dipole beams to the magnetic quadrupole trap center in two steps, 1) coarse alignment by overlapping the dipole beam with a resonant 780 nm beam, and 2) fine alignment by imaging a cold atomic cloud in the quadrupole and dipole trap, separately.

#### Coarse alignment

In the first step of alignment, we work with atoms in a 3D-MOT because it can be probed for a long time and continuously. Since the temperature of the atoms in the 3D-MOT is 100's of microkelvin, much above the dipole trap depth it is not possible to load the atoms directly into the dipole trap or see an effect of the dipole beam onto the atoms. We use a resonant 780 nm probe beam of diameter 1 mm and power a few mW's aligned

to go through the 3D-MOT. Due to the radiation pressure imbalance this beam empties the MOT, or makes a hole depending on its size compared to the cloud size. The probe beam comes from the opposite direction than that of the dipole beam. Once the probe beam is aligned to the center of the MOT, we switch on the dipole beam and overlap the two beams using irises of opening  $\sim 1$  mm, before and after the science cell. The overlap ensures that the dipole beam goes the MOT center. After the beams are overlapped, the probe beam is switched off and we run a MOT sequence until the molasses with dipole beams on. The cloud temperature in the molasses goes down to  $30\text{-}40\ \mu\text{K}$  (dipole trap depth set to  $70\ \mu\text{K}$ ). In this way, the atoms were loaded into a single beam dipole trap and the step was repeated for both the dipole beams. However, this is only a rough alignment to locate the beams near the trap center. Fig. 3.11 shows one of the first absorption images of the  $^{87}\text{Rb}$  atoms in a single beam dipole trap loaded from the molasses.

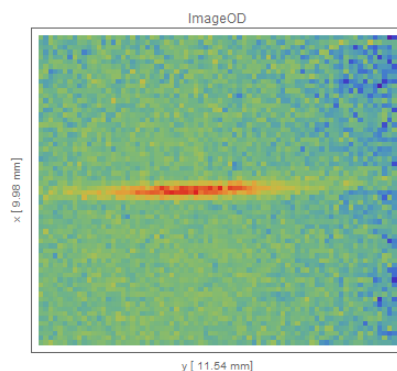


Figure 3.11: A false color absorption image of the atoms in a single beam dipole trap loaded directly from the 3D-MOT.

### Fine alignment

Since the cloud size in the MOT is a few millimeters and the MOT position can be slightly different than that of the magnetic trap, we go through a second step of fine alignment. Here, we fine tune the dipole beam position near the magnetic trap center, such that the dipole and quadrupole traps overlap down to a micrometers. We first load atoms from the MOT into a quadrupole trap and perform rf evaporation there. The final rf frequency is set such that the evaporated cloud size becomes of the order of the dipole trapping volume. We image the atoms from two orthogonal imaging systems, gives 3D position of the magnetic trap. The same step of locating the trap minimum in 3D was repeated for the single beam and crossed beam dipole. Fig. 3.12 shows two images after matching the crossed dipole and quadrupole trap.



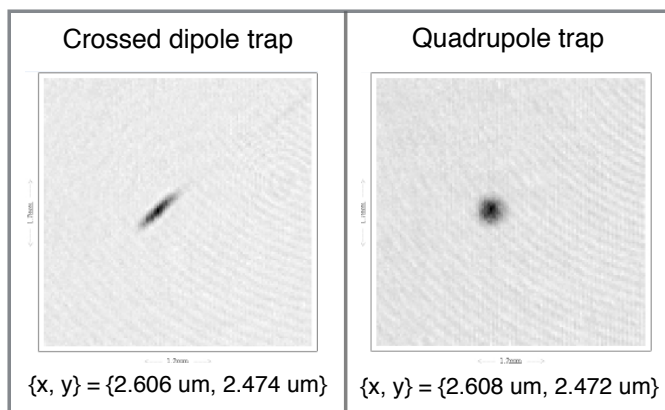


Figure 3.12: Absorption images of atom clouds in the crossed dipole and quadrupole trap, images taken from the vertical imaging system. The two trap positions differ only by a few  $\mu\text{m}$ 's which is the order of shot to shot trap stability.

We also measured the dipole beam pointing stability for the powers of up to 1 W using a CCD camera, a wedge prism, and found it to be less than  $2 \mu\text{m}$ . In the dipole setup, the dipole beam position at the science cell center was coarsely tuned by the mirrors M3 and M4, and fine tuned by the AOM frequencies. Care should be taken that there is no dc B-field present while measuring the magnetic trap position. This can be checked by looking at the magnetic trap position at different magnetic gradients).

### Beam waist measurement

To measure the dipole beam waist, we place a mirror right after the lens L3 (L4) (see Fig. 3.10) to direct the beam away from the compact dipole breadboard. The dipole beam sizes at different points along the path was measured by the knife-edge method. The measured beam sizes were fitted to the equation:

$$\omega(z) = \omega_0 \sqrt{1 + \left(\frac{z - z_0}{z_R}\right)^2} \quad (3.1)$$

where  $\omega_0$  is the beam waist and  $z_R$  is the Rayleigh length. Fig. 3.13 shows the dipole beam size at different distance of the razor blade from the lens L3 (L4). From the fitting we get: dipole waist of  $66 (4) \mu\text{m}$ ,  $z_R$  of 1.2 cm, and  $z_0$  is equal to 25 cm. If we calculate the Rayleigh length from,  $z_R = \pi(\omega_0)^2/\lambda$ , it comes to be 1.29 cm for the 1060 nm wavelength. We repeated the measurement of the dipole beam waist for both the beams and measured them to be equal.

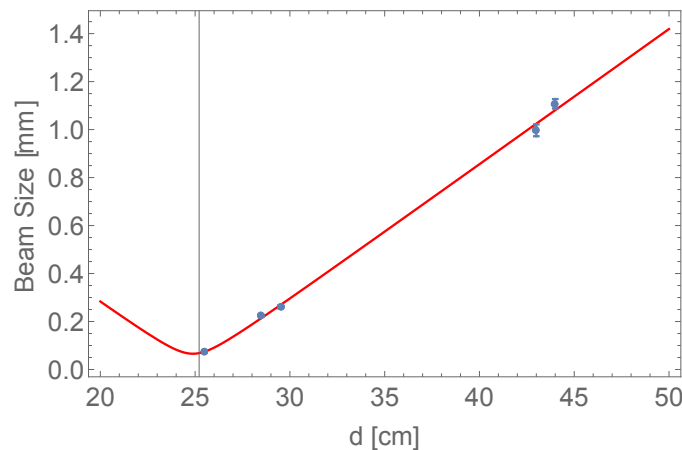


Figure 3.13: The size of the dipole beam at different distances from the lens L3 (see Fig. 3.10) to the razor blade. The points on the other side of the focus were not taken due to the lack of space.

### 3.3.3 Dipole laser safety interlock

A safety interlock system was built synchronized with the dipole laser amplifier. The safety interlock system was designed such that it is safe to work with different settings of the dipole power, experiment and lab doors. The dipole laser amplifier only gives an output when its interlock – two wires at the back, are connected. Our interlock system is an extension of these two wires, to an electronic circuit which automatically opens the circuit when it is an unsafe condition. The interlock system involves four experiment doors, main door of the lab, and the dipole setup AOMs. The four experiment doors are divided in two parts in the circuit – three side doors and one back door. The experiment table is covered with four pneumatic valve controlled doors. With the doors closed, the experiment table is completely shielded. The three side doors open towards a working area and the back doors faces a wall. Three switches are installed on each of the experiment door frames, the interlock circuit is closed when the doors are down. One switch is plugged to the lab door and connected with the interlock box.

Fig. 3.14 shows a truth table for different stages related to the interlock system. In the first column, the four bits represents – Master control, Dipole high power, back doors, and the side doors of the experiment table. The green light represents safe condition, yellow is intermediate, and red shows danger. The column 24 V relay represents on/off state of the dipole AOMs. The relays are controlled by the digital channels of the DIO-64 card, switched on/off during the experiment sequence. In the lab, a tricolor LED was installed, power by the interlock box, and it is used to indicate different stages related to the safety. The different states of the truth table are,

1000 – Dipole AOMs off (low power in the dipole beams), all experiment doors closed, lab door closed, Master switch engaged. The green LED glows and it is safe to work. This stage is for the low power dipole beam alignment.

1001 – Dipole AOMs off (low power in the dipole beams), experiment side doors open, experiment back door closed, lab door closed, Master switch engaged. The green LED glows and it is safe to work. This stage is for the low power dipole beam alignment.

1010 – Dipole AOMs off (low power in the dipole beams), experiment side doors closed, experiment back door open, lab door closed, Master switch engaged. The green LED glows and it is safe to work. This stage is for the low power dipole beam alignment.

1011 – Dipole AOMs off (low power in the dipole beams), experiment side doors open, experiment back door open, lab door closed, Master switch engaged. The green LED glows and it is safe to work. This stage is for the low power dipole beam alignment.

1100 – Dipole AOMs on (high power in the dipole beams), experiment side doors closed, experiment back door closed, lab door closed, Master switch engaged. The green and yellow LED glows and it is safe to work. This stage is for running the experiment.

1101 – Dipole AOMs on (high power in the dipole beams), experiment side doors closed, experiment back door open, lab door open, Master switch engaged. The red and yellow LED glows and it is a death mode – danger.

1110 – Dipole AOMs on (high power in the dipole beams), experiment side doors open, experiment back door closed, lab door closed, Master switch engaged. This stage is designed for the high power alignment of the dipole beams. The red and yellow LED glows and represents danger.

1111 – Dipole AOMs on (high power in the dipole beams), experiment side doors open, experiment back door open, lab door open, Master switch engaged. The red and yellow LED glows and represents danger.

State	Comment				Relays 24 V	Lab door defeated
1000	Low power, all doors closed				0	1
1001					0	1
1010					0	1
1011	Aligning safe light				0	1
1100	Standard Experiment running				1	1
1101	DEATH MODE				1	0
1110	Aligning HP Back door open				1	1
1111	DEATH MODE				1	0

Figure 3.14: Truth table of the dipole laser safety interlock system.

Fig 3.15 shows the dipole laser interlock box which is connected with all the experiment door switches, lab door switch, dipole AOMs, and the dipole laser amplifier interlock wires. The interlock box is powered by a 24 V DC power adapter. A Master switch was installed in the interlock box, to break the circuit manually if an emergency occurs. The green LEDs at the front of the interlock box indicates whether the respective door is engaged (closed) or defeated (open). The red LED represents whether the dipole AOMs are on (high power) or off (low power). The three switches at the front panel are four pole double throw type, and the master switch is push button type.

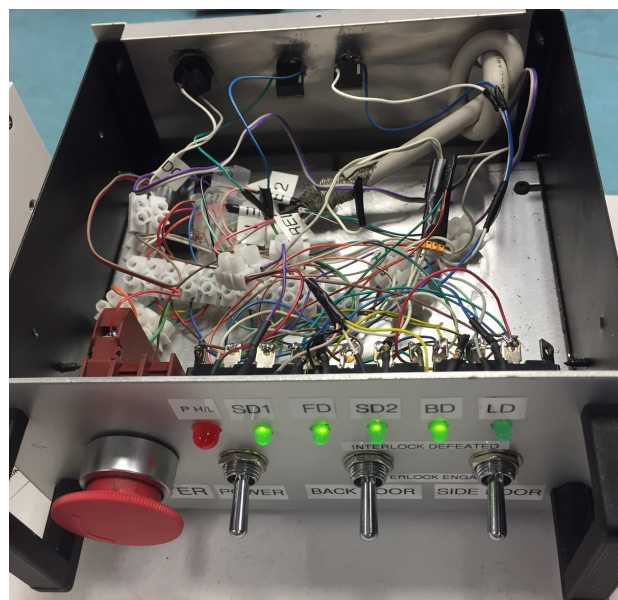


Figure 3.15: Dipole laser safety interlock box.

### 3.4 Imaging system

We use absorption imaging technique to determine the atom number and the size of the cloud. The temperature of the atom cloud is calculated from its size against a variable time-of-flight (TOF) expansion. By the use of two identical imaging setups, we can either image the atoms from the top (gravity axis) or aligned with the Y axis (horizontal) in the lab frame. The vertical imaging is mainly for the atoms in the TAAP ring. Fig. 3.16 shows a schematic of the imaging setup. The near-resonant imaging beam coming out of a single mode fibre is first allowed to freely expand and then collimated to a final size of 1 inch, as in the case of 3D-MOT beam collimators. The imaging beam is linearly polarized. The beam then passes through the atom cloud, since the beam is resonant with the atomic transition, absorption happens and some photons go missing in the direction of the beam. This creates a dark spot/shadow in the beam which is imaged onto a CCD camera (Andor iKon-M DU934N-BR-DD). A homemade telescope, L2 and L2 (4f system [87]) recreates the intensity profile after a distance  $4f$  which is then magnified/demagnified using a microscope objective. The resolution of this imaging is about  $13 \mu\text{m}$ . The intensity of the imaging beam is kept around  $1/10^{\text{th}}$  of  $I_s$ , to avoid saturation and stay in the linear regime of absorption. The duration for which the beam is turned on is  $< 200 \mu\text{s}$ . The beam detuning is varied depending on the density of the atom cloud, e.g., if imaging a BEC detuning is around  $-12 \text{ MHz}$  and resonant for a very dilute thermal cloud.

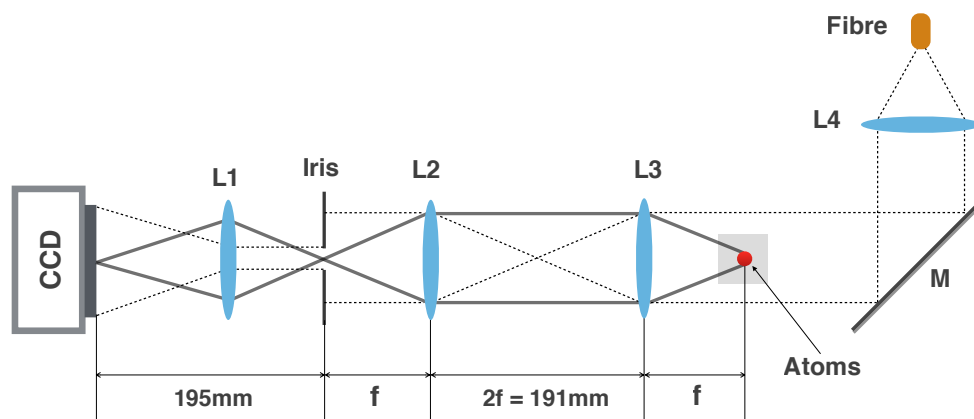


Figure 3.16: Schematic of the absorption imaging setup.

Let us look at the principle of the absorption imaging technique. Consider a laser beam with intensity  $I_0$ , passes through an atom cloud, and according to the Beer's law the transmitted intensity  $I$  will be given by:

$$I = I_0 e^{-OD} \quad (3.2)$$

where  $OD$  is the optical density, or the amount of light absorbed by the atoms. If the beam intensity is well below  $I_s$  then the  $OD$  can be written in terms of the absorption cross-section,  $\sigma$ , and the atom column density,  $n(x, y)$ . The above equation is then:

$$I = I_0 e^{-n(x,y)\sigma} \quad (3.3)$$

where  $\sigma$  is given by:

$$\sigma = \frac{\sigma_0}{1 + \frac{I_0}{I_s} + \left(\frac{\delta}{\Gamma/2}\right)^2} \quad (3.4)$$

where  $\sigma_0$  is the absorption cross section on resonance,  $\delta$  is the laser detuning, and  $\Gamma$  the natural linewidth. To calculate the atom number from the  $OD$ , three images are taken, one with atoms and the beam, one without atoms and the beam, and one where the camera is only exposed to the stray light. The  $OD$  is given by:

$$OD = \ln \frac{I_{\text{beam}} - I_{\text{stray}}}{I_{\text{atoms}} - I_{\text{stray}}} \quad (3.5)$$

where  $I_{\text{atoms}}$  is the intensity with the atoms,  $I_{\text{beam}}$  without atoms, and  $I_{\text{stray}}$  is when the imaging beam is off. Now the atom number  $n$  can be calculated by integrating the  $OD$  over the exposed region:

$$n = \int \int n(x, y) dx dy = \frac{1}{\sigma} \int \int OD dx dy \quad (3.6)$$

## Chapter 4

# BEC production

### 4.1 TOP trap

#### The road to BEC

The sequence begins by loading atoms into the 3DMOT from a 2DMOT, later compressed and sub-Doppler cooled in the CMOT and Molasses. The 3D-MOT beams are then suddenly switched off and the TOP trap is turned on, simultaneously. Both the quadrupole field and the rotating bias fields are switched on at the same time. It is crucial to switch on the magnetic trap fast compared to the time given by the effective trapping frequency in the MOT. The effective trapping frequency at the end of the MOT stage is measured via the time-of-flight (TOF) expansion method. A slow switch on will result in a mode mismatch, the result will be cloud heating, atom number loss, and shape oscillations. In our experiment, the quadrupole field rises to its maximum in about  $50 \mu\text{s}$  and the bias field in about  $2.5 \text{ ms}$ , which is much faster than the effective trapping period (of the order of  $100 \text{ ms}$  at the end of the MOT). Two things need to be considered for the mode matching: trapping frequencies and the positions of the trap. First one we optimize by varying the gradient and keeping the bias field amplitude to the maximum ( $48 \text{ G}$ ), and second by displacing the 3D-MOT using the dc field of compensations coils. The bias field switch on amplitude defines the radius of the circle of death, or the trap depth. Circle of death is essentially the trajectory of the quadrupole field zero, in a circle, and should be set large compared to the cloud size ( temperature). Typically it is set a few times higher than the cloud temperature and minimizes any evaporation due to this circling zero.

The atomic cloud captured in the TOP trap is then adiabatically compressed by ramping up the magnetic gradient and keeping the bias field amplitude fixed. The

compression is adiabatic in the sense that we do not lose atom number and only the temperature rises. This stage is optimized (ramp time and the final magnetic gradient) by looking at the evaporation efficiency in the next stage, i.e., rf evaporation. This is done by fixing all the parameters of the rf evaporation and maximizing  $N/\Delta x$  for different compression parameters, where  $N$  is the number of atoms and  $\Delta x$  the cloud size after a long TOF (essentially a measure of the temperature). Lastly, the cloud is evaporatively cooled using the rf-induced evaporation method. During the evaporation, both the bias field amplitude and the rf-field frequency is ramped down. The ramp shape for both the rf-field frequency and bias field amplitude is linear. There is an additional compression of the cloud during the rf evaporation since the bias field is ramped downwards, hence the trapping frequency increases. This increases the elastic collision rate as the evaporation proceeds. The initial rf-field energy is set in-between  $2g_F\mu_B B_m$  and  $g_F\mu_B B_m$  and the final value slightly above the  $g_F\mu_B B_m$ . A nearly pure BEC is formed when the rf photon energy approaches the ground state harmonic oscillator energy.

Below, I begin by describing a very precise calibration method of the TOP trap elements, i.e., bias field amplitudes, trap circularity, quadrupole field gradient, and then I will give the related results. The details of the BEC production is described in the section afterwards.

### 4.1.1 Trap characterization

In this section, I will describe a method for the complete characterization of the TOP trap by the use of rf evaporation and trapping frequency measurements. A simple and widely used TOP trap consists of a rotating bias field and a quadrupole field. The bias field can be decomposed in three: the two field amplitudes, generated by the two pairs of Helmholtz coils and a relative phase between the fields. The total B-field can be written as:

$$B = \alpha \begin{pmatrix} x \\ y \\ -2z \end{pmatrix} + \begin{pmatrix} B_x \cos(\omega_m t) \\ B_y \cos(\omega_m t + \phi) \\ 0 \end{pmatrix} \quad (4.1)$$

where  $\alpha$  is the magnetic gradient,  $B_x$  and  $B_y$  are two field amplitudes along the  $x$  and  $y$  lab frame axes,  $\phi$  is a phase offset between the two channels, and  $\omega_m$  is the oscillation frequency of the bias field.

To get a BEC in the TOP trap, I have taken two paths. First, transfer a ultracold cloud at  $\sim 2 \mu\text{K}$  temperature from crossed-dipole trap to the TOP, and then perform rf



evaporation. Second, transfer the atoms from MOT directly into the TOP trap, and subsequent compression and rf evaporation leads to a BEC. For the trap characterization, I followed the first one since it is much faster and efficient. Let us look at the  $\phi$  calibration first.  $\phi$  is a combination of, 1) the programmed electronic phase, and 2) physical angle between the coils. The physical angle can be measured by running the coils in the DC mode and displacing a cold cloud held in the quadrupole trap. This is a way to measure the orientation of the two bias field coils with respect to the imaging axes. From the experiment, I get an angle of  $1.1^\circ$  and  $1.6^\circ$  for the  $x$  and  $y$  coils, respectively, and both in the first quadrant of the imaging frame. This is included in the programmed phase as a correction factor. The electronic phase is measured by monitoring the voltage drop across the pickup resistors and is set very precisely to  $90^\circ$ . Now to calibrate the two amplitudes, I load an ultracold cloud in a slightly elliptic trap (see Fig. 4.1). The amplitude imbalance (ellipticity) is set a few times larger than the chemical potential of the BEC. Fig. 4.1 shows the elliptic trajectory of the quadrupole zero together with the instantaneous rf-field maximum coupling region.

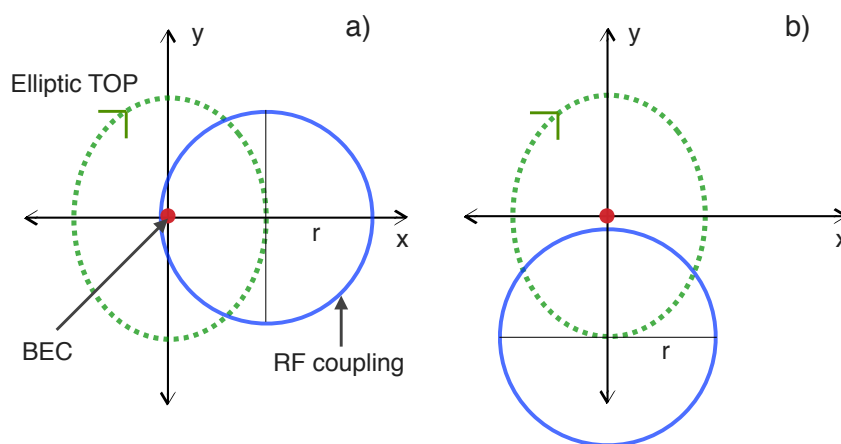


Figure 4.1: An elliptic TOP trap together with the rf-field. a) The rf-field resonance circle at some instant and the rf is resonant with the atoms due to  $B_x$ . b) After a quarter oscillation period of the bias field the circle rotates by  $90^\circ$  and the rf-field does not interact with the atoms.

By making the trap elliptic we see that the atoms do not see the rf-field when the instantaneous quadrupole is along the  $y$  axis. This is because a larger bias field amplitude, i.e.,  $B_y$ , displaces the quadrupole further away from the center and thus it will require a higher rf frequency for it to be resonant with the atoms. Using this technique the trap can be emptied with only  $B_x$  ( $B_y$ ) at a time, and the rf-field frequency where we exactly outcouple all the atoms corresponds to the bias field amplitude, linked by the relation  $h\nu_{RF} = g_F\mu_B B_m$ . The precision we get is a few kHz in the

rf-frequency for the bias field amplitudes up to 10 G, translates to  $10^{-4}$  level of precision in  $B_x$  ( $B_y$ ). This precision is mainly limited by the stability of the bias fields.

Before calibrating the amplitudes, I excite a circular center of mass oscillation of the cloud to measure the trap ellipticity. A scheme to excite such an oscillation is shown in Fig 4.2a. It is a two step process, first the trap is jumped along the  $x$  ( $y$ ) axis and then after a quarter of the trapping frequency hold the trap is jumped along the  $y$  ( $x$ ) axis. Finally, the trap is brought back to the initial position giving an angular kick to the cloud. The amplitude of the jump should be kept small compared to the harmonic extent of the trap or can be made equal to the in-trap cloud size. I program these jumps using the compensation coils.

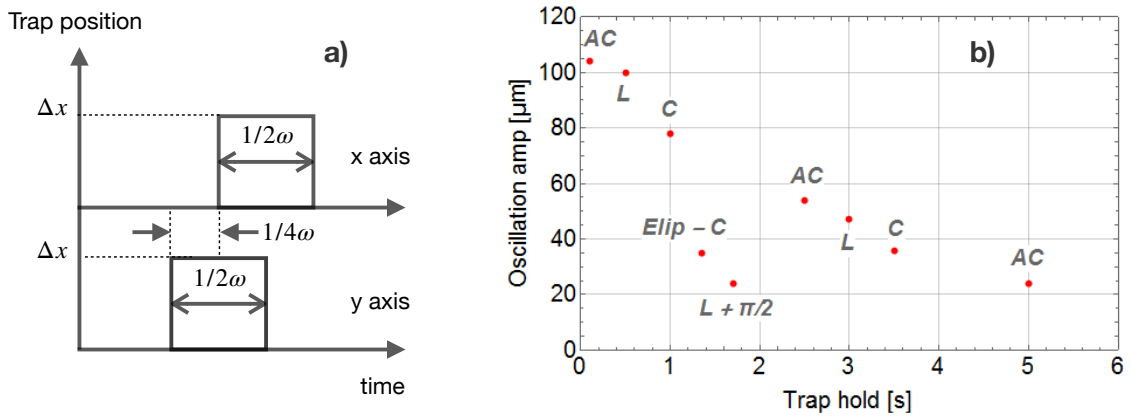


Figure 4.2: a) A method to excite circular center of mass oscillation of the cloud by jumping the TOP trap along the two orthogonal axis. b) Oscillation amplitudes and the sense of rotation of the cloud against hold times in the trap. AC and C stands for the anticlockwise and clockwise rotation of the cloud, respectively. This is for the case when the trap frequencies along the  $x$  and  $y$  axes are not matched.

This circular oscillation of the atoms will experience any small frequency difference between the two axis, or the cloud will undergo from clockwise – linear – anti-clockwise oscillation with a frequency given by the trapping frequency difference. Fig. 4.2b shows the oscillation amplitude of the cloud and the sense of rotation versus hold time in the trap. The trapping frequency difference from these oscillations is 2.7 Hz. Fig. 4.3 shows the cloud oscillation along the  $x$  and  $y$  axis after calibrating the two amplitudes by the use of rf outcoupling. For this set of data, the bias field and the magnetic gradient was at 5 G and 90 Gpcm, respectively. I fit the whole data to an ellipse with its principal axis, two frequencies, phases, and amplitudes as a free parameter. The position along  $x$  ( $y$ ) axis is then:

$$x(t) = a_0 + a_1 \text{Exp}[-t/\tau] \cos 2\pi f_x(t - t_0) \quad (4.2)$$

where  $a_0$  is an offset,  $a_1$  is the oscillation amplitude,  $\tau$  is the decay time constant,  $f_x$  is the trapping frequency along the  $x$  axis and  $t_0$  is a phase offset. The fit finds trapping frequencies of 36.17(1) Hz and 36.02(1) Hz along the  $x$  and  $y$  axis, respectively. The oscillation amplitudes along the  $x$  and  $y$  axis are 58(2)  $\mu\text{m}$  and 87(2)  $\mu\text{m}$ , respectively. The trap ellipticity is calculated by dividing the two trapping frequencies,  $\epsilon_{xy} = \omega_x/\omega_y$ , and  $\epsilon_{xy}$  is 1.0041(0.0004). In the fitting, the principle axis of the oscillation is set free, and find that the major axis of the ellipse is rotated by  $32^\circ$  w.r.t. imaging axis. We know the two coils are not exactly aligned at  $90^\circ$  but  $87.4^\circ$ . A small amplitude imbalance (with a few mG resolution) together with the phase can give rise to a large rotation of the principal axis. I find that the programmed quadrupole gradient was 0.8% higher than calculated from this trapping frequency measurement.

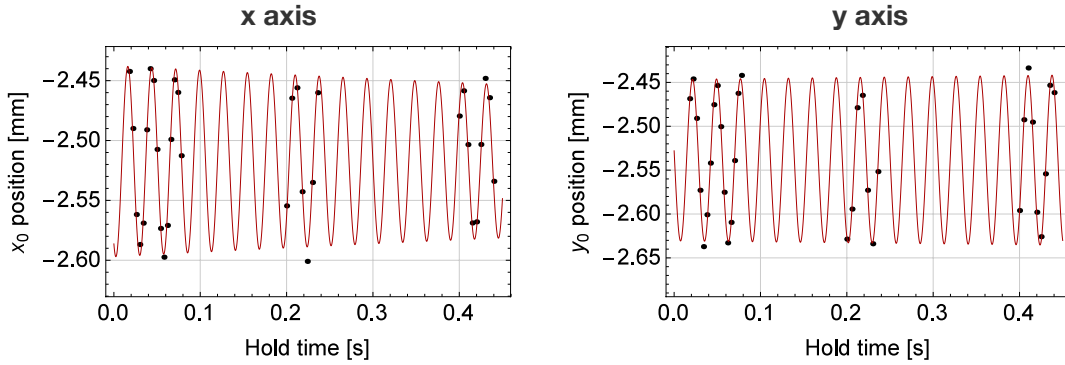


Figure 4.3: The position of the ultracold atom cloud along the two imaging axis during its circular oscillation in the trap, after matching the two-axis trapping frequencies.

### 4.1.2 BEC production

These results below are from a few years ago when the system was not working at its best, the sequence took longer with lower BEC numbers but the idea stands firm. Later we switched to the crossed-dipole trap since the evaporation efficiency is much higher than in the TOP trap. First, about  $3 \times 10^9$  atoms are loaded in the 3D-MOT in a duration of 35 s. The magnetic gradient and the laser beam detuning during this stage are 6 Gpc/m and -13 MHz, respectively. Right after the MOT loading, laser detuning is ramped away from the resonance, from -13 MHz to -30 MHz in 20 ms, and the cloud is compressed in this CMOT. The magnetic gradient is kept constant during the CMOT. The atom number drops to about  $2 \times 10^9$  at the end of the CMOT. The final stage of the MOT is molasses where the magnetic gradient is switched off completely and only MOT lasers are on for the next 20 ms. At this stage, the cloud has  $\sim 10^9$  atoms at a temperature of 130  $\mu\text{K}$ .

Next, we transfer the atoms into a TOP trap, the rotating bias is in the horizontal plane orthogonal to the gravity axis. The cloud is recaptured in a TOP trap of magnetic gradient and bias field amplitude equal to 65 Gpcm and 48 G, respectively. A hold time of 1 s is given after the recapture, for any oscillations to damp out. The cloud is then adiabatically compressed by ramping the magnetic gradient from 65 Gpcm to 210 Gpcm, in 12 s, corresponds to a factor of about 3 increase in the trapping frequency. The bias field is at 48 G until the end of the compression. Then, a weak rf-field is switched on at a frequency 68 MHz. We program a downward ramp in both the rf-field frequency (via sweep mode of the function generator) and rotating bias amplitudes (sound programmed in Mathematica) for 33 s. Fig. 4.4a) is an absorption image of the atom cloud after a TOF expansion of 12 ms, captured by the horizontal imaging system. The final value of the bias field amplitude and the rf-field frequency for this shot is 1.1 G and 0.97 MHz, respectively. Panels b) and c) shows atomic density profile along the  $x$  and  $y$  imaging axis, respectively. It is clear from the bimodal density distribution that the cloud contains Bose condensed atoms, released from a harmonic trap together with a thermal component. The number of atoms in the condensate and thermal cloud are,  $3.3 \times 10^4$  and  $7.2 \times 10^4$ , respectively. The lifetime of the condensate in a decompressed TOP trap goes up to 2 minutes.

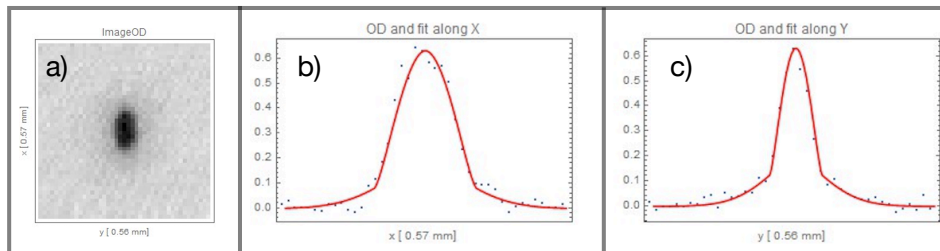


Figure 4.4: a) An absorption image of the Bose-Einstein condensate, taken after releasing the cloud from the TOP trap. b) and c) is a bimodal (Gaussian for thermal atoms and inverted parabola for the condensed atoms) fit to the atomic density along the  $x$  and  $y$  axes, respectively.

## 4.2 Crossed dipole trap

### The road to BEC

One big advantage of using an optical dipole trap is the desired tight confinement of the atoms for the BEC production. Due to the small trapping volume together with the large trap depth a high density cold atoms can be trapped in a dipole trap. This helps

in achieving small elastic collision times which is then utilized in the evaporation stage, resulting in a faster and efficient way of BEC generation in optical dipole traps. A very long lifetime of the cold atoms is achievable in such traps, up to minutes.

Let us first go through the theme behind the BEC production in a crossed dipole trap. We start by loading the 3DMOT from a 2DMOT and the cloud is then compressed in a CMOT, like in the case of TOP trap sequence. After the near-resonant light CMOT, atoms are transferred from  $F=2$  hyperfine state to  $F=1$  by ramping down the repumper amplitude, i.e., microwave radiation power (see 3.1). It is a dark MOT stage where due to the absence of scattering events, the cloud is compressed further [13]. The atoms in the internal state  $|1,-1\rangle$  are then recaptured in a quadrupole trap, compressed and evaporatively cooled with a weak-rf. The final temperature of the cloud in the quadrupole trap (or the final rf-field frequency) is set such that it is a factor of 2 to 3 below the dipole trap depth. The dipole beams can be switched on either during the magnetic compression or during the rf evaporation, at the maximum power.

To transfer the atoms from the magnetic quadrupole to the dipole, the quadrupole is lifted vertically upwards using a  $z$  bias field by about one dipole beam waist during the magnetic compression. This is done to avoid the overlapping of the B-field zero and the dipole trap center during the dipole evaporation (will result in spin flip losses), and gravity-enabled adiabatic loading of the dipole trap. The atoms are adiabatically loaded into the crossed dipole trap by ramping down the quadrupole gradient to slightly below gravity. The quadrupole is kept on at this value after the loading, provides longitudinal confinement and preserves the magnetic polarization of the atoms. Finally, the atomic cloud is evaporated by ramping down the power of the dipole beams, nearly exponentially, and the magnetic gradient. In this way, we produce BECs in a single-beam or crossed-beam hybrid magneto-dipole traps.

### 4.2.1 Sequence optimization

One of the important stage in the dipole experiment sequence is the CMOT. Here we compress the cloud in a dark MOT by ramping down the repumper power and populating all the atoms into the  $F=1$  hyperfine state, and the scattering rate drops enormously. Compression of the cloud at this stage is utilized during the dipole evaporation. Although there is another compression stage later, i.e., magnetic compression in the quadrupole but there we have heating of the cloud as well, which has an upper limit due to the dipole trap depth. In the dark MOT, there is compression and the temperature drops as in the case of a molasses. We ramp down the magnetic

gradient during the repumper downwards ramp, from 6 Gpc/m to 2 Gpc/m. Fig. 4.5 shows the peak optical density of the cloud for different dark MOT duration's, after loading the cloud from MOT to magnetic quadrupole to the crossed dipole. The optimum time for the CMOT we find is around 50 ms, for too low CMOT duration the atoms are not transferred to the dark state and for too long they are not trapped since the scattering force has been turned off.

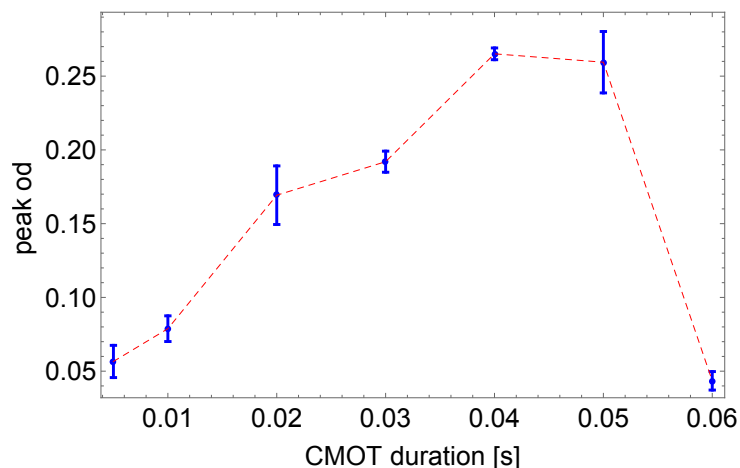


Figure 4.5: Peak optical density of the atom cloud loaded in the crossed dipole trap versus the duration of the CMOT. A higher od corresponds to more atoms in a smaller volume, i.e., higher atomic density, resulting in an efficient evaporation in the dipole trap.

Another crucial stage of the dipole sequence is the adiabatic loading of the atoms from the quadrupole trap to the crossed dipole (single beam dipole) trap. To achieve this, we follow the same idea as explained in the ref. [71]. A z d.c. bias field lifts the quadrupole upwards keeping the dipole beams position fixed. Then, the magnetic gradient is ramped down to a strength below gravity, and the atoms flow to the below-positioned dipole trap. If the quadrupole is too far from the dipole the atoms will fall and since they are not trapped anymore the cloud will expand. If the quadrupole is too close to the dipole center, due to the presence of the magnetic field zero there will be spin flip losses. An optimal situation is when the quadrupole is lifted by a distance equal to one waist of the dipole beam. Fig. 4.6 shows the number of atoms transferred to the crossed dipole trap versus the z bias amplitude.

## 4.2.2 BEC production

Here I will give the details of the BEC production sequence in our hybrid trap of crossed dipole and magnetic quadrupole. The sequence is same as of the TOP trap until

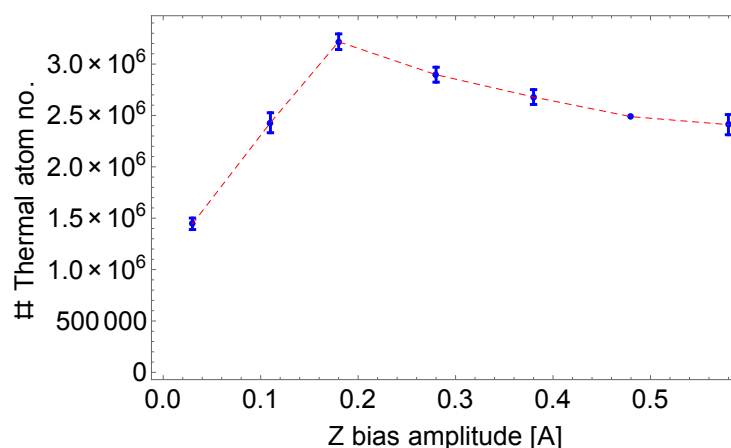


Figure 4.6: Number of atoms loaded in the crossed dipole trap versus the vertical position of the quadrupole (quadrupole position depends on the amplitude of the d.c. bias field added) with respect to the dipole center.

the MOT loading. We load about  $2 \times 10^8$  atoms into the magnetic quadrupole trap from the CMOT, cloud at a temperature of  $70 \mu\text{K}$  and the atoms in  $|1,-1\rangle$  state. The magnetic gradient for the recapture is  $50 \text{ Gpcm}$ , and is ramped from  $50 \text{ Gpcm}$  to  $120 \text{ Gpcm}$  in  $1 \text{ s}$  to compress the atom cloud. The atom number remains almost unchanged during the magnetic compression and the temperature rises to  $130 \mu\text{K}$ . Afterwards, we perform rf-induced evaporation in the magnetic trap, the rf-field can be switched during the recapture or at the end of the compression, if the rf photon energy is larger than the energy/spatial extent of the cloud the rf acts as a energy knife only. We program a frequency sweep in the function generator (Rigol DG1062) for the rf evaporation, the initial rf frequency is at  $21 \text{ MHz}$ . The frequency sweep is programmed for  $5 \text{ s}$ , the rf frequency is ramped from  $21 \text{ MHz}$  to a final frequency of  $6.5 \text{ MHz}$ . Due to the forced evaporation, the atom number drops to  $2 \times 10^7$  and the temperature to  $40 \mu\text{K}$ .

The dipole beams are switched on during the magnetic compression, at a total power of  $12 \text{ W}$ . The power of the dipole beams is kept constant during the magnetic compression and rf evaporation. By the use of  $z$  modulation coils, we lift the magnetic quadrupole by about one beam waist during the magnetic compression (rf evaporation). During the dipole trap loading and evaporation in the hybrid trap the  $z$  d.c. bias amplitude is kept constant. To load the atoms into the crossed dipole, the magnetic gradient is ramped from  $120 \text{ Gpcm}$  to  $10 \text{ Gcm}$ , in  $1 \text{ s}$ . The step above opens up the quadrupole trap with the final trap strength below gravity, and the atoms fall into the crossed dipole trap. After loading the atoms into the hybrid magneto-dipole trap, we perform evaporation by ramping down the dipole beams power nearly exponentially, in about  $6 \text{ s}$ . The magnetic gradient during the dipole evaporation is ramped from  $10 \text{ Gpcm}$  to  $2 \text{ Gpcm}$ . A bimodal distribution start to appear at around

$1/10^{\text{th}}$  of the initial trap depth. Fig. 4.7 shows the transition from thermal distribution of the atoms to a BEC as the longitudinal trap frequency is increased by bringing the quadrupole closer to the dipole trap center. As explained in the theory chapter, a small displacement of the quadrupole from the dipole center gives a larger longitudinal trapping frequency and hence higher collision rates, and thus efficient evaporation.

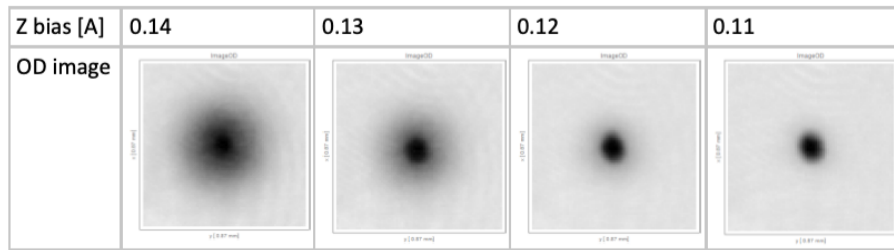


Figure 4.7: Thermal to BEC transition by varying the position of the quadrupole minimum with respect to the center of the dipole beam, or by tuning the longitudinal trapping frequency in a single beam hybrid magneto-dipole trap.

Another key test of a BEC apart from the bimodal distribution of the atoms is the inversion in the aspect ratio of the atomic cloud in free fall, when it is released from an anisotropic potential. This is due to the fact that along the direction in which the trapping frequency is higher there is a higher gradient in the density which gives rise to a faster expansion velocity compared to the weaker directions, see Fig. 4.8.

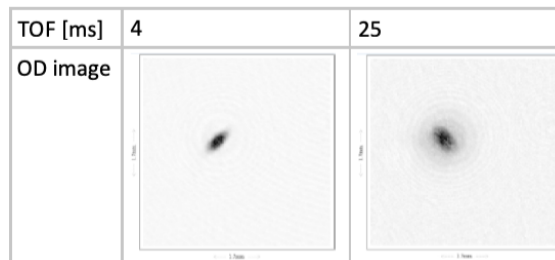


Figure 4.8: Inversion of the aspect ratio of the condensate after it is released from a crossed-beam optical dipole trap. Thermal atoms are not visible in short TOF, i.e., 4 ms but one can clearly see for the case of 25 ms.



### BEC number stability

I measured the stability of the number of Bose-condensed atoms produced in the crossed-beam dipole trap. Fig. 4.9 shows the number of atoms in the BEC for about half an hour run, each experiment cycle is about 30 s. The standard deviation calculated from the data is about 6%. This fluctuation mainly comes from the initial stage of the experiment, i.e., MOT loading. Apart from this fluctuation, I also saw a slow drift (on the time scale of half an hour) in the atom number loaded into the dipole during the morning only and later confirmed that it was due to the dipole laser finding an equilibrium after switching it on. The atom number then reaches a steady value after this half an hour drift.

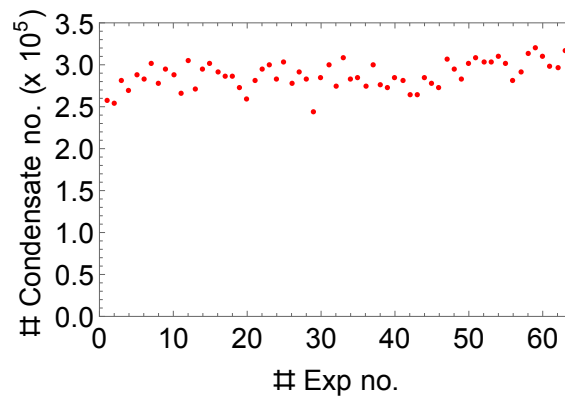


Figure 4.9: Condensate number stability in the crossed-beam dipole trap.

## Chapter 5

# Ring trap loading, characterization, and arbitrary traps

### The idea

BECs are loaded into the TAAP ring from a combined trap of magnetic quadrupole and crossed-beam optical dipole trap. We first evaporate the atom cloud in the crossed dipole trap down to the BEC, and keep a sub-gravity strength quadrupole field on. Since the quadrupole is one-beam-waist above the dipole during the evaporation stage, we need to displace the quadrupole minimum radially and axially, such that the ring overlaps with the crossed dipole. We do this in a single step – right after the evaporation quadrupole is displaced radially by using the  $xy$  compensation coils, and the  $z$  d.c. bias is ramped to zero, simultaneously. The direction of the ring displacement is set orthogonal to the crossed dipole trap long axis i.e. 45 deg from the  $x(y)$  axis of the lab frame, provides mode matching between the two traps resulting in an adiabatic transfer. Then the full ring potential is turned on at a very low magnetic gradient, which gives a very large radius ring. We turn on the rf dressing field and the low frequency modulation field, both  $\pi$  polarized along the  $z$  axis. The dipole trap strength is kept constant during the d.c. bias ramps and ring turning on, holds the atom cloud.

After the rf-dressing and modulation fields are turned on, the magnetic quadrupole gradient is ramped upwards slowly to a desired value, creates a horizontal ring waveguide of well-defined radius. Finally, the power in the crossed dipole beams is ramped down slowly and BECs are loaded into the ring waveguide. Any mismatch in the trapping frequencies of the two traps do not matter since we ramp down the dipole trap slowly (adiabatically), like in the case of adiabatic compression (decompression). Since the dipole trap gives a tighter confinement than the ring trap,

there is cooling of the atomic gas due to the transfer. The center of the two traps were matched down to a few micrometers, using the d.c. bias fields in all the directions to displace the ring, and by imaging the atoms in both the traps separately. For different experiments, BECs were loaded into the tilted ring traps as well as in the flat ring waveguides. For the BEC acceleration, transport and atom optics experiments, a tilted ring potential was switched on from the beginning to avoid spreading of the atom cloud along the azimuthal direction. We were able to transfer the atom cloud without any atom number loss, heating, shape or center of mass oscillations. Fig. 5.2 shows the ring loading scheme from a crossed dipole trap.

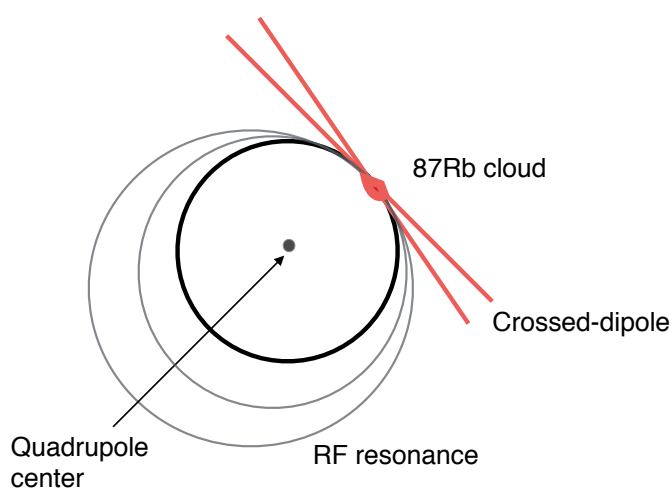


Figure 5.1: Schematic of the ring loading from a crossed beam optical dipole trap. The two red lines (the dipole beams have large Rayleigh length compared to the ring-dipole cross-section) represent the crossed beams of the dipole trap with atoms trapped in the intersection volume. Black circles represent the TAAP ring potential minimum for different magnetic gradients during the loading.

## 5.1 Ring loading results

The sequence until the crossed dipole evaporation is described in the section 4.2. At the end of the crossed dipole evaporation, we get about  $3 \times 10^5$  atoms in the BEC with the ensemble temperature at 50 nK. The crossed dipole evaporation happens in a duration of about 6 s. During the dipole evaporation, the magnetic gradient was ramped downwards from 10 Gpcm to 2 Gpcm, and the total dipole power from 12 W to about 1 W. Using the  $xy$  compensation coil d.c. fields, the magnetic quadrupole at 2 Gpcm was displaced horizontally and orthogonal to the crossed-beam dipole long axis, and the  $z$  bias was ramped to 0 in 200 ms, at the same time. The radial displacement of the

quadrupole field was chosen to be about 20% larger than the ring radius to avoid any excitation due to the rf and modulation fields turning on. Next, we ramp the  $xy$  d.c. bias amplitudes to a matching condition, i.e., displacement of the ring center from the dipole center is one ring radius, in 50 ms. To load the atoms into the ring waveguide, a full TAAP ring was switched on – linearly polarized  $z$  rf-field and the  $z$  modulation field at amplitudes  $\sim 350$  kHz of Rabi frequency and 1.4 G, respectively. The frequency of the rf and modulation fields were fixed at 2.55 MHz and 5.02 kHz, respectively. To load the atoms into a tilted ring potential,  $xy$  modulation fields were also switched on together with the  $z$  rf and modulations field. The  $xy$  modulation fields oscillate at the same frequency as of the  $z$  and have an equal amplitude of 0.55 G (this amplitude decides the azimuthal ring trapping frequency and hence matching with the dipole long axis trapping frequency). The relative phase between the  $xy$  ( $x$   $y$  are in phase) and  $z$  modulation fields were set such that the ring potential is tilted or creates an azimuthal confinement along the direction of the crossed-dipole trap center. Before the final step, the magnetic gradient is ramped from 2 Gpcm to 70 Gpcm in a 100 ms duration. Since the displacement of the quadrupole is proportional to the d.c. bias field amplitude, when the gradient is ramped up the ring radius decreases and the ring center moves towards the crossed dipole trap. In other words, ring and the crossed dipole trap remains aligned during the gradient ramp. Finally, the dipole beam power is ramped down completely in 150 ms and the atoms are loaded in the ring trap. Since the ring is displaced horizontally by one ring radius with respect to no d.c. bias condition, we ramp down the  $xy$  bias to 0 in 100 ms.

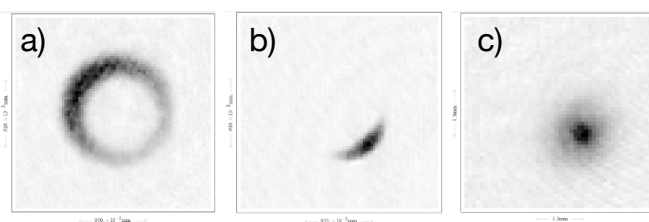


Figure 5.2: Absorption images of ultracold atom clouds in the ring potential. a) An ultracold thermal cloud loaded into a flat ring waveguide without correcting the mechanical tilt. b) BEC loaded in a tilted ring trap, image taken after 100 ms of hold time and ToF of 3 ms. c) 24 ms TOF image of b) with a clear bimodal density distribution of the atoms. All the images were taken by using the vertical imaging system. The fringes in the background are due to the imaging.

## 5.2 Ring trap characterization

After loading BECs into the tilted ring traps, the potential was characterized via several measurements. The ring trapping frequencies were measured by exciting center of mass oscillations of the cloud along the azimuthal, radial and axial directions. The dependence of ring radius on the magnetic quadrupole gradient, modulation field and rf-field amplitudes was studied. The lifetime and heating rate of the atomic cloud was measured with ultracold atoms in the ring trap. The natural tilt of the ring waveguide was measured and corrected using additional radial rf-dressing fields.

### 5.2.1 Trapping frequencies

#### Azimuthal direction

The ring trapping frequency along the azimuthal direction was measured by exciting center of mass oscillation of the cloud trapped in a tilted ring. After loading an ultracold atom cloud (BEC) into the tilted ring trap, the azimuthal potential minimum was jumped by a small angle. The azimuthal minimum was jumped by switching the relative phase between the  $xy$  and  $z$  modulation fields, from 0 deg to 22.5 deg.  $z$  and  $xy$  modulation field amplitudes were 1.4 G, and 0.55 G, respectively. As a consequence, the cloud started to oscillate in this azimuthally displaced trap. After the trap is jumped, the position of the cloud is measured for different hold times in the tilted ring trap. Fig. 5.3 shows oscillation of the atom cloud for various hold times in the trap. The cloud position is fitted to the model,

$$y(t) = a_0 + a_1 \sin(2\pi ft + \phi) \quad (5.1)$$

where  $a_0$  is a no-oscillation trap position,  $a_1$  is the oscillation amplitude,  $f$  is the azimuthal ring trapping frequency, and  $\phi$  is some arbitrary phase. From the fit, we find  $a_0$  and  $a_1$  to be 3.6 mm and 148  $\mu\text{m}$ . The fit gives an azimuthal trapping frequency of 9.17 (3) Hz.

#### Along the radial and axial direction

The ring trapping frequency along the radial and axial directions were measured by using the same method - by exciting center of mass oscillations. For these measurements, a tilted ring trap containing BEC was jumped by using the  $xy$  compensation coil fields. The jump amplitude was programmed to be of the order of

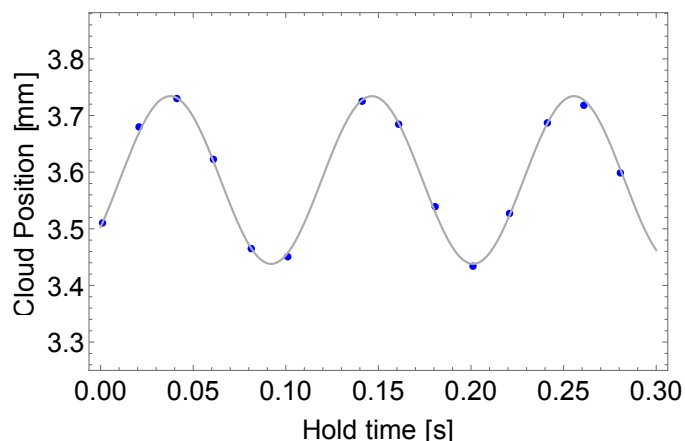


Figure 5.3: Center of mass oscillation of the atom cloud along the azimuthal direction of a tilted ring trap.

the cloud size. In order to excite both the radial and axial oscillations, the direction of the jump was not exactly orthogonal to the radial direction but slightly tilted. Fig. 5.4 shows center of mass oscillation of the atom cloud versus hold time in the ring trap after the trap was displaced instantaneously. The cloud position versus hold time was fitted to the equation,

$$y(t) = a_0 + a_1 \sin(2\pi f_r t + \phi_1) + a_2 \sin(2\pi f_a t + \phi_2) \quad (5.2)$$

where  $a_0$  is the mean trap position,  $a_1$  and  $a_2$  are the oscillation amplitudes along the two directions,  $f_r$  and  $f_a$  are the radial and axial trapping frequencies, respectively, and  $\phi_1$ ,  $\phi_2$  are the arbitrary initial phases for this two-axis oscillations. The fit provides 0.43 mm for  $a_0$ ,  $a_1$  and  $a_2$  to be  $39 \mu\text{m}$  and  $30 \mu\text{m}$ , and  $f_r$  and  $f_a$  to be 85.3 (4) Hz and 46.2 (3) Hz, respectively. These trapping frequencies match well with the theoretical predictions and we derive the  $z$  rf-dressing field Rabi frequency  $\Omega_{\text{RF}}$  to be 357 kHz, from the radial trapping frequency.

## 5.2.2 Ring waveguide radius

I studied the dependence of a flat ring waveguide on the different parameters of the system, i.e., magnetic quadrupole gradient, the  $z$  rf-field amplitude, and the  $z$  modulation field amplitude.

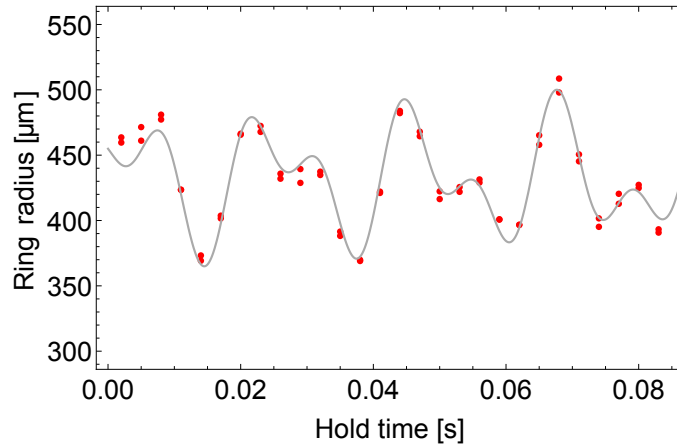


Figure 5.4: Center of mass oscillation of the atom cloud along the radial and axial directions, in a tilted ring trap.

### Gradient dependence

Figure 5.5 shows the radius of a horizontal flat ring waveguide with the magnetic gradient. The relation between the magnetic gradient and the ring radius comes from the fact that the potential minimum of the rf-dressed trap lies where the rf-field is resonant with the bare Zeeman sublevels. If one fixes the rf-field frequency and tunes the magnetic gradient, then at higher (lower) value of the gradient the absolute value of the slope of Zeeman energy levels increases (decreases). This means that at higher magnetic gradients the rf-field will be resonant near the center of the quadrupole trap, and hence a lower radius of the ring waveguide. The relation between the ring radius, magnetic gradient, and the rf-field frequency has the form:  $R \sim \hbar\omega_{\text{rf}}/|g_{\text{F}}|\mu_{\text{B}}\alpha$  [53].

### Modulation field amplitude dependence

A ring waveguide is formed when we add a vertical modulation field to the rf-dressed adiabatic potential. The strength of the modulation field plays an important role in the radius of the ring, trapping frequencies of the ring trap (see section 2.3.3), and also the lifetime of the atoms in the ring trap. Figure 5.6 shows the dependence of the ring radius with the  $z$  modulation field strength. In this case, to form the ring waveguide I used a linearly polarized rf-field in the vertical direction, with a frequency 2.55 MHz, Rabi frequency  $\approx 2\pi 357$  kHz. The magnetic gradient was at a value of 70 G/cm. For very low modulation field strengths, the radial ring trapping frequency is at the maximum, same as in the case of a rf-dressed trap with no modulation field, and the axial trapping frequency is close to zero. But due to the gravity the atoms fall, and they can not stay in this rf-coupling region, which is like a ring. As the modulation field becomes stronger

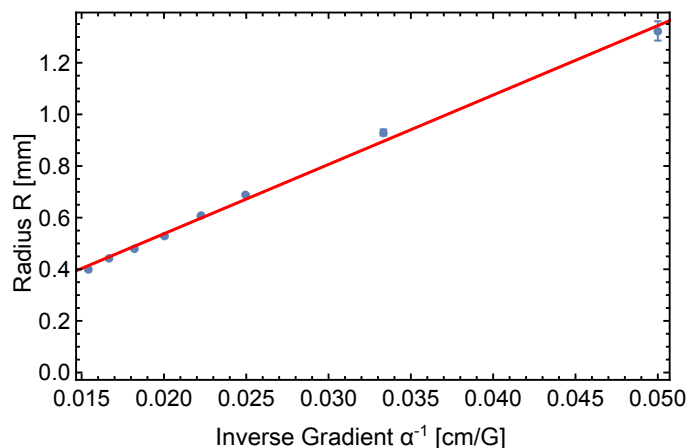


Figure 5.5: The radius of the ring waveguide versus the inverse of the magnetic quadrupole gradient. The circular  $xy$  rf-field frequency, rf-field Rabi frequency, and  $z$  modulation field amplitudes were, 2.5 MHz,  $2\pi 300$  kHz, and 1.9 G, respectively. The fluctuation (standard deviation) in the ring radius was about 0.3%, if the same experimental sequence is repeated many times. The red line is a guide to the eye. The figure is from the ref. [61].

the axial trapping frequency increases and hence the ring radius, i.e., atoms can stay against the gravity. For very large amplitudes, the potential is shaken out of the rf-field resonance region and one loses the coupling, and as a result the ring starts to deform again.

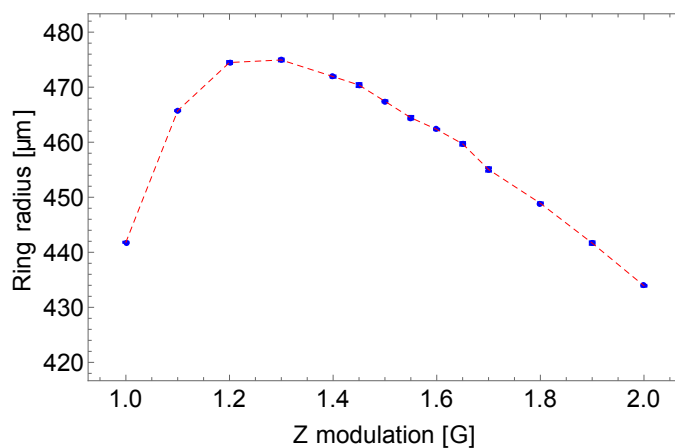


Figure 5.6: The ring radius versus the amplitude of the vertical modulation field. A 2 s hold time was given for all the data points before imaging the atoms.

### RF amplitude dependence

I also studied the dependence of the ring waveguide radius with the dressing rf-field strength. Figure 5.7 shows the radius of the atom cloud trapped in a flat waveguide for



different values of the  $z$  rf-field amplitude. A hold time of 2 s was given before measuring the ring radius, using the vertical absorption imaging. The lifetime of the atom cloud is relatively short for the lower rf-field amplitudes due to the increased probability of the spin flip losses, occurring at the bottom of the trap. The radial and the axial trapping frequencies of the ring trap are inversely proportional to the rf-field amplitude (see section 2.3.3), and thus for low rf-field strengths the axial trapping frequency is higher and hence atoms sit at a higher point vertically, against the gravity. As the rf-field strength is increased, the axial trapping frequency drops and the ring radius shrinks.

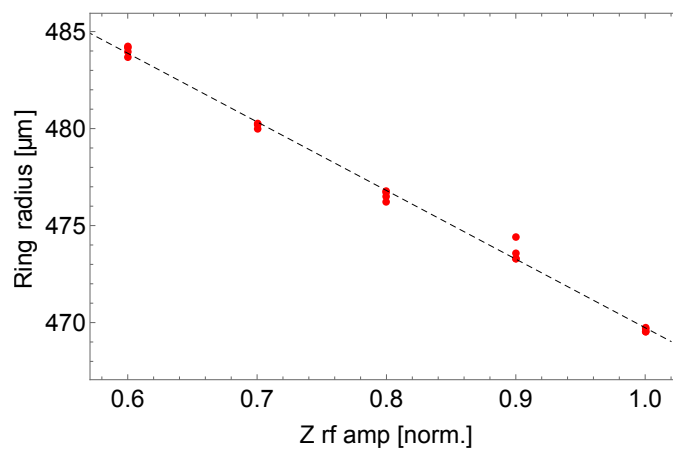


Figure 5.7: The relation between the ring radius and the strength of the linearly polarized rf-field, in the vertical direction. The experimental conditions were same as in the case of the section above.

### Stability over time

Figure 5.8 shows the radius of the ring waveguide over time, repeating an identical experimental sequence for up to 65 runs. It is a flat ring waveguide with the parameters same as in the sections above, images were taken after a hold time of 3.5 s. The mean value of the ring waveguide radius is  $470.3 \mu\text{m}$  with a standard deviation of  $0.5 \mu\text{m}$ , or 0.1%. For the case of tilted ring traps, the measured position stability has a standard deviation of  $10 \mu\text{m}$ , or 23 mrad, which is seen as the noise in the BEC transport, results in the chapter 6.

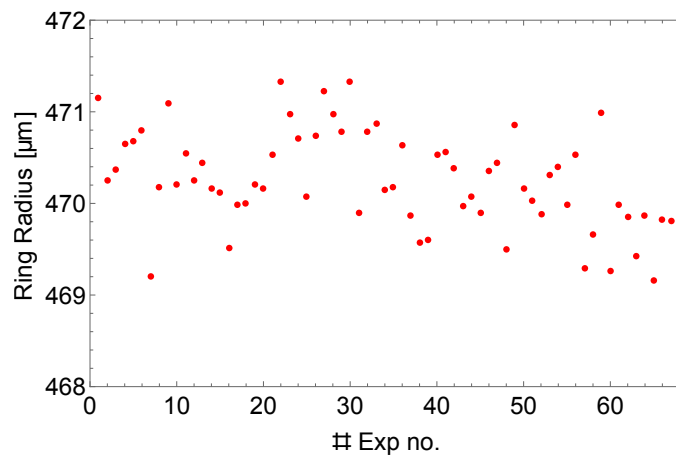


Figure 5.8: The radius of the ring waveguide over time. The spacing the points is equal to the experiment sequence time of 26 s.

### 5.2.3 Lifetime and heating rate

Figure 5.9 shows the decay in the number of ultracold thermal atoms loaded in a flat ring waveguide. I load about  $10^6$  atoms at a temperature of  $3 \mu\text{k}$  into the waveguide. The fit finds a  $1/e$  lifetime of 7.6 (5) s. The lifetime depends significantly on the noise in the sound field, i.e., the specs of the audio amplifier.

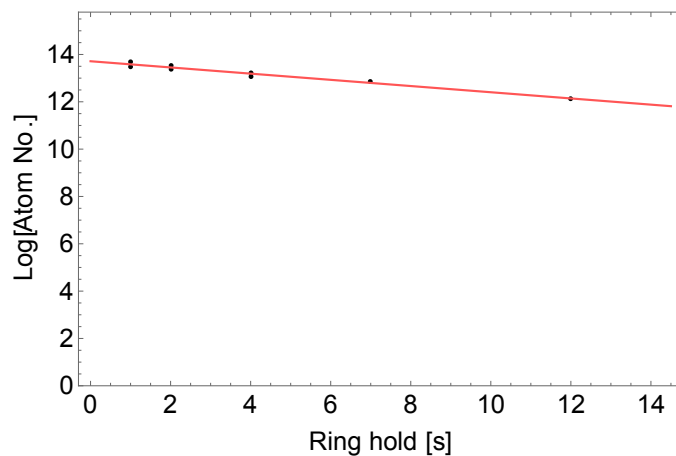


Figure 5.9: The lifetime of the atom cloud in a flat ring waveguide.

I measured the heating rate of the atom cloud loaded in the ring waveguide. Fig. 5.10 shows the temperature of the atom cloud versus the hold time. I fit a straight line to the data, and find a slope of  $3(1) \text{ nK/s}$ , with an initial temperature of  $460 \text{ nK}$ .

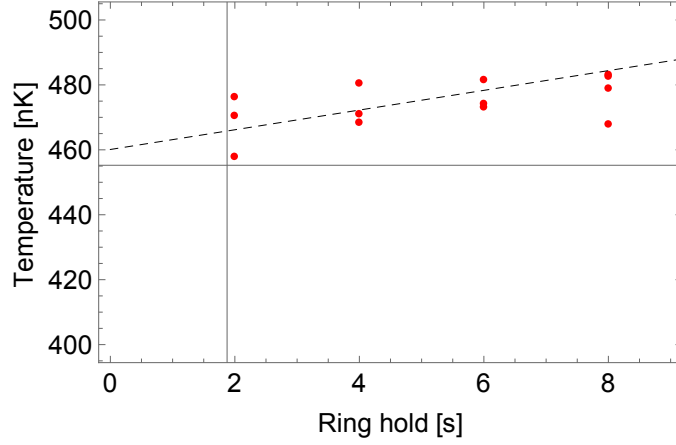


Figure 5.10: The temperature of an ultracold thermal cloud in a ring waveguide against the hold time.

### 5.3 Flattening the ring waveguide

This section explains the compensation of the mechanical tilt of our ring waveguide, can be present due to the imperfect alignment of the coils, or due to the mutual coupling between the coils, consider both the modulation and the rf-dressing coils. To characterize the flatness of our no-tilt ring potential with static atoms, i.e, no angular motion, atom cloud containing about  $10^6$  atoms at 430 nK is loaded into the ring potential. The radius of a no-tilt ring trap is  $470.3(5) \mu\text{m}$ . We image the atom cloud after a long hold of 6.5 s, to make sure there are no center of mass oscillations present. The azimuthal atomic density is fitted with a potential of the form:

$$V_\phi = V_{\phi c} [1 + h_1 \cos(\phi + \phi_1) + h_2 \cos(2\phi + \phi_2)] \quad (5.3)$$

where  $V_{\phi c}$  is a energy scale factor,  $h_1$  and  $h_2$  are arbitrary tilt amplitudes corresponding to  $\phi$  and  $2\phi$  tilt, respectively, and they a phase of  $\phi_1$  and  $\phi_1$ . I measured a 15 mrad tilt of the ring plane from the horizontal (or tilt a vector orthogonal to the vertical axis) for the  $\phi$  tilt. It can be due to a small deviation of the modulation or rf-field from the z-axis, or the coils are perfectly aligned with the vertical axis. To correct this mechanical tilt, it is important to identify the source causing it since both the rf-field and the modulation can result in a similar potential landscape. The addition of a weak modulation field in the  $xy$  plane tilts the ring potential in the direction of field added, very much like a gravitational tilt.

An arbitrary static tilt can be designed over  $2\pi$  (at any angle in a circle) by the use of  $x$  and  $y$  modulation or rf fields. We use  $x, y$  modulation fields for the azimuthal BEC trapping and transport. A weak  $x$  rf-field is used for the correction of the mechanical

tilt. The angle of the mechanical tilt is along the  $x$  rf antenna, and I programmed  $x$  rf to be  $180^\circ$  out of phase with respect to the  $z$  rf giving a tilt in the direction opposite to the mechanical tilt. After correction, the measured amplitudes for the  $\phi$  and  $2\phi$  tilts are 0.104 and 0.2 mrad, respectively. Our experiment table has a re-leveling accuracy of less than 33 nm (or  $33 \mu\text{rad}$  with IPV-HP2-KT Newport isolation valves) over 1 mm diameter of the ring. Fig. 5.12 shows the tilt amplitude  $h_1$  of the ring potential versus the normalized  $x$  rf amplitude,  $h_2$  remains nearly unchanged due to this compensation.

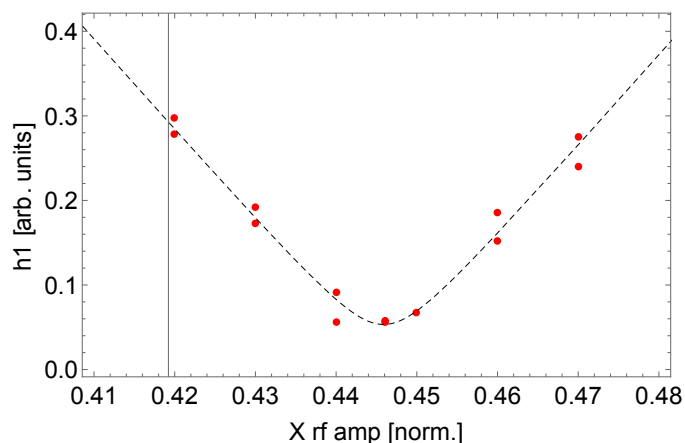


Figure 5.11: Tilt amplitude  $h_1$  versus the amplitude of the weak  $x$  rf, used to compensate the mechanical tilt.

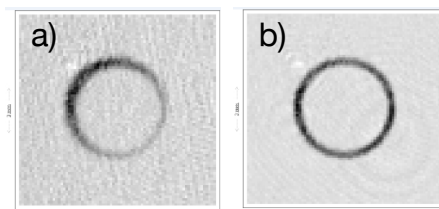


Figure 5.12: a) Absorption of an ultracold thermal cloud in the waveguide without the mechanical tilt compensation, b) after compensation, using the  $x$  rf-field, in phase with the  $z$  rf.

## 5.4 Arbitrary ring traps

We devised methods to manipulate ultracold atoms in tilted ring traps in a state (spin) dependent and state independent manner. This is important for the atom interferometry in our magnetic ring trap using internal states of the atoms, and keeping the atom cloud compact as it goes around in a circle. A combination of two

orthogonal vectors (here modulation field and rf field tilts) can give complete freedom to move the resultant vector anywhere in a circle. The modulation field tilt is state independent, and a weak elliptic rf was used to create state dependent tilts. For the rf tilts, only one state can be trapped in one half of the ring, and vice versa. I give results for both the individual type of tilts and when they are combined.

### 5.4.1 State-insensitive: modulation tilt

Figure 5.13 shows different angle of the azimuthal minimum when  $x$  modulation (sound) field is added to the  $z$  with different relative phases. The atoms are in the  $|F = 1, m_F = -1\rangle$  state. The experimental sequence is same as in the sections above, MOT to quadrupole trap to crossed-dipole trap to the ring, loaded with about  $1.5 \times 10^5$  atoms at a temperature  $< 1 \mu\text{K}$ . These rings are at a magnetic gradient of 85 Gpc/m, and the  $z$  modulation field amplitude is 1.7 G. To move the ring azimuthal minimum, the amplitude of the  $x$  modulation was fixed at 0.1 G, and only the phase was varied. After loading the atoms into a flat ring waveguide, I ramp up the  $x$  field amplitude, and give 120 ms of hold time before imaging the atoms. All the images were taken after a time-of-flight of 1.3 ms. The modulation tilt is very much like the gravitational tilt, i.e., if the gravity axis was not vertical but slightly tilted. This tilt has the same effect on the ring trap for both the internal states.

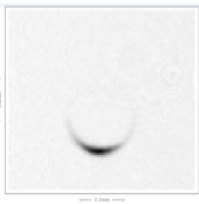



Image				
X sound phase [deg]	0	180	135	-45

Figure 5.13: Absorption images of ultracold atom clouds in modulation-field tilted ring traps, depending on the relative phase between the  $z$  and  $x$  modulation field, the tilt finds a new minimum. The phase of the  $x$  sound field is with respect to the  $z$  one.

### 5.4.2 State-sensitive: rf polarization tilt

The ring can be tilted by the use of rf field as well, but now depending on the relative phase between the radial and the axial rf, one can create state dependent of independent

traps. If we choose the relative phase to be  $\pi/2$ , the ring will deform into two half moon shaped traps, for the two states. This is because the two clock state of  $^{87}\text{Rb}$ ,  $|1,-1\rangle$  and  $|2,1\rangle$ , have the opposite sign of the gyromagnetic ratio. Fig. 5.14 is an absorption image of the atoms, in the  $|2,2\rangle$  state, loaded in an rf-field tilted ring trap, the relative phase between the  $xy$  and  $z$  rf was  $90^\circ$ . We can also move the azimuthal potential minimum in a circle by just modulation the phase between the radial and the axial rf, or together with the amplitude can give full control to perform transport of BECs (ultracold atoms).

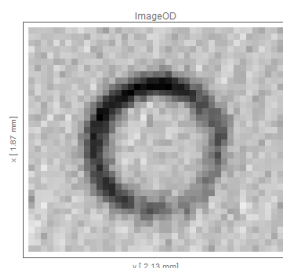


Figure 5.14: Absorption image of  $|2,2\rangle$  atoms in an rf tilted ring trap.

### 5.4.3 Simultaneous independent traps for two spin states

Here I give the results for the case where the two kinds of tilt are combined, i.e., the state dependent modulation and the state independent rf tilt. During the interferometer sequence, the one starts with a single cloud trapped by the modulation tilt, apply the microwave beam splitter, and the ramp up the rf tilt and ramp down the modulation tilt, simultaneously. The amplitude of the rf and the modulation fields are very weak compared to the axial ones. The relative phase between the axial and the radial rf field is  $\pi/2$ , provides coupling to one internal state in half of the ring and other state is trapped in the other half. Fig. 5.15 shows the trapping of the atoms, in two different internal states in the ring traps. As shown in the fig. 5.13 we can dynamically move the two trap minimum (for the two states) by adjusting the rf and the modulation field amplitudes. These results were published in the reference [61].

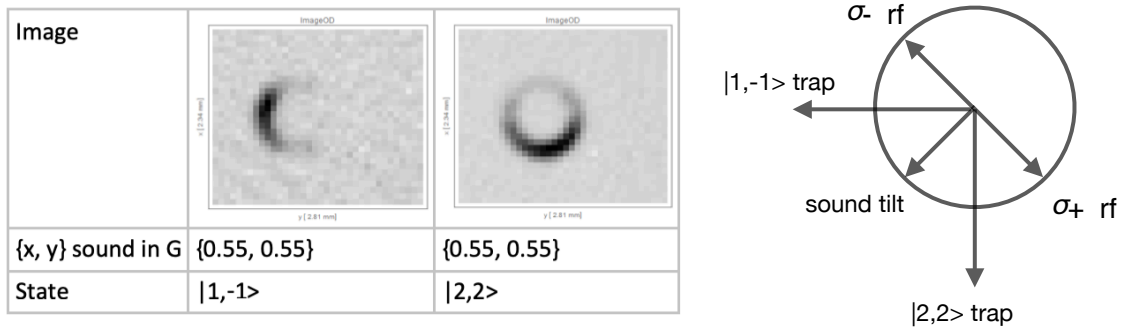


Figure 5.15: Left: Two absorption images of the atom clouds in arbitrary ring traps. Atoms in the two different internal states find a different minimum in an identical experimental sequence. Right: the arrows showing the programmed sound and the rf tilts, and the resulting trap location for the two states, which matches with the images.

## Chapter 6

# Acceleration and hypersonic transport of BECs

In this chapter, I provide the experimental study of the acceleration and hypersonic transport of BECs in tilted TAAP ring traps. I will start by explaining one of the solutions of the optimal control theory, i.e., Bang-bang scheme [48], which we used to accelerate and then transport the ultracold atoms for record long distances and without any measurable excitation of the atom cloud. By the use of  $x, y$  modulation and radio-frequency fields, an arbitrary azimuthal trap trajectories can be designed [61], and for the two internal states of the atoms. The transport of BECs, here, is done by moving the azimuthal potential minimum of the ring trap in a circle. We can design and precisely control the acceleration profile of the trap, with an upper limit on the final angular speed set by the radial trapping frequency of the ring trap. Due to the angular motion of the trap, the centrifugal force modifies the ring trapping parameters and the ring radius, and I explain that with a model. To transport the Bose-condensed atoms at hypersonic speeds, trap acceleration was stopped at a well-defined angular speed and then switched to a constant speed. In this chapter, I provide results for the excitationless BEC acceleration, and transport for up to tens of centimeter long distances in tilted ring traps.

### 6.1 Bang-bang control

Let us start by considering that we have the atoms trapped in a harmonic potential, at rest (no center of mass motion), and sitting at the bottom of the trap. The center of mass manipulation of the cloud will be done in such a way that the cloud remains in the harmonic region of the potential. The main idea is to transport the atoms without



exciting any shape or center of mass oscillations. One can not reach a constant velocity without going through acceleration of the particles, and the same idea applies if the atoms are to be brought at rest again. The steps I am describing below is true for a circular trajectory of the trap (atoms) as well for the linear one.

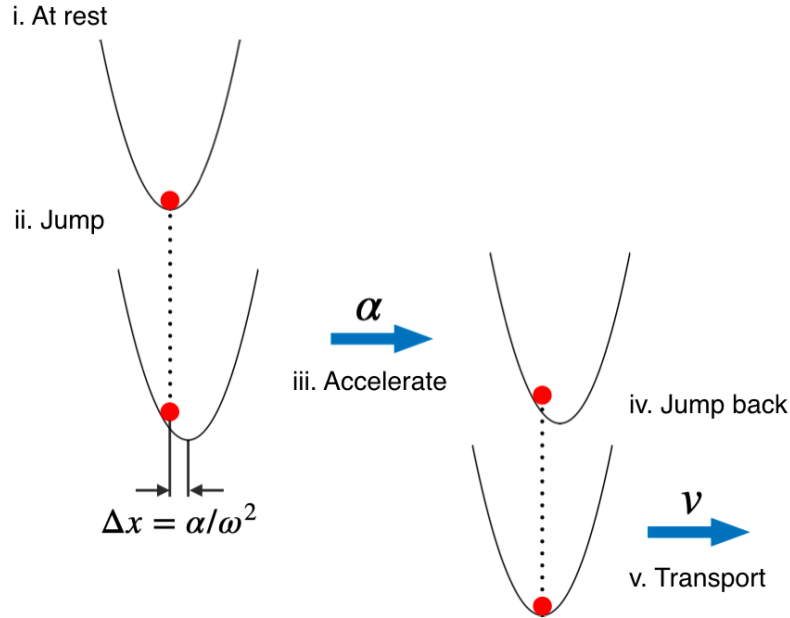


Figure 6.1: The steps involved in the acceleration and transport of ultracold atoms in our ring trap.

To start the trap (atom cloud) motion, the trap is first jumped forward by an angle  $\Delta\phi$  along the azimuthal direction. A jump in the trap is needed to compensate the pseudo force felt by the atoms while the trap is accelerating. To calculate the trap jump amplitude, we equate the force due to the trap acceleration  $\alpha$  and the force due to the harmonic potential curvature, i.e., gradient of the potential at a distance  $\Delta\phi$  away from the trap center. This means,  $m\omega^2\Delta\phi = m\alpha$ , where  $m$  is the mass of the particle and  $\omega$  the trapping frequency. The amplitude of the trap jump is then,  $\Delta\phi = \alpha/\omega^2$ , for the linear transport case this will not be an angle but in distance units. In the experiment, we jump the azimuthal trap minimum angle by fast switching of the  $x$  and  $x$  modulation field amplitudes and keeping the resultant amplitude (like a vector moving in a circle), and the relative phases fixed. Next is the trap acceleration, it is done by programming a frequency sweep between the radial and the axial modulation fields, i.e., the trap minimum starts to accelerate in a circle. After reaching a desired angular speed, the same step is repeated – the trap is jumped back by the same amount (angle) and the we then program a constant angular speed motion of the trap (atoms). To bring the atoms at rest after some transport, we can follow the same steps backward with a difference that now the jump directions will be reversed.

## 6.2 BEC acceleration

Before starting the ring acceleration, I load about  $3 \times 10^5$  Bose condensed atoms into a tilted ring trap from the crossed dipole trap, BEC chemical potential at 32 nK. Figure 6.2 shows the absorption images of BECs while they are accelerated in a tilted ring trap. The angular acceleration programmed in this case was  $2\pi \times 50 \text{ rad/s}^2$ , and if one calculates the angular distance travelled by the atoms in 200 ms, it is  $2\pi$ , from  $s = \frac{1}{2}at^2$ , which means the atom cloud comes back to the original position/angle, and very clear from the images. Using the horizontal imaging system, and a long time of flight after switching off the trap, I confirmed that the atom cloud is still a condensate. In the section below, I give the lifetime and heating rate measurements for both the static and moving trap (atom cloud) case.

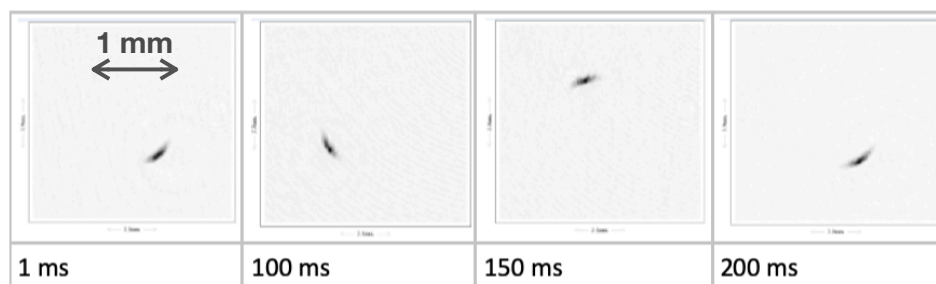


Figure 6.2: Absorption images of BECs accelerating in a tilted ring trap. The images were taken after a time of flight of 3.3 ms.

I also studied the motion of BECs for different angular accelerations, fig. 6.3 shows the angular position of the BECs for this case. For a different acceleration, the trap jump amplitude has to be different, and hence for the five different acceleration in Fig. 6.3. In the case of  $2\pi \times 25 \text{ rad/s}^2$ , the programmed trap jump was  $\Delta\phi = \pm 0.5 \text{ mrad}$ , and it scales proportional to the acceleration value. I analyzed the radial and the longitudinal widths of the atom cloud during the acceleration. The radial size of the cloud remains nearly unchanged up to the maximum acceleration programmed,  $2\pi \times 400 \text{ rad/s}^2$ . A small positive slope was measured in the azimuthal size for the acceleration above  $2\pi \times 100 \text{ rad/s}^2$ , the effective azimuthal trapping frequency reduces as the angular velocity increases which is like a trap decompression and the cloud size increases.

### 6.2.1 Waveguide deformation due to the angular motion

For the BEC transport sequence, explained below, at  $2\pi \times 10 \text{ rad/s}$ , first, the BECs are accelerated at  $2\pi \times 50 \text{ rad/s}^2$ . Due to the centrifugal force associated with the angular

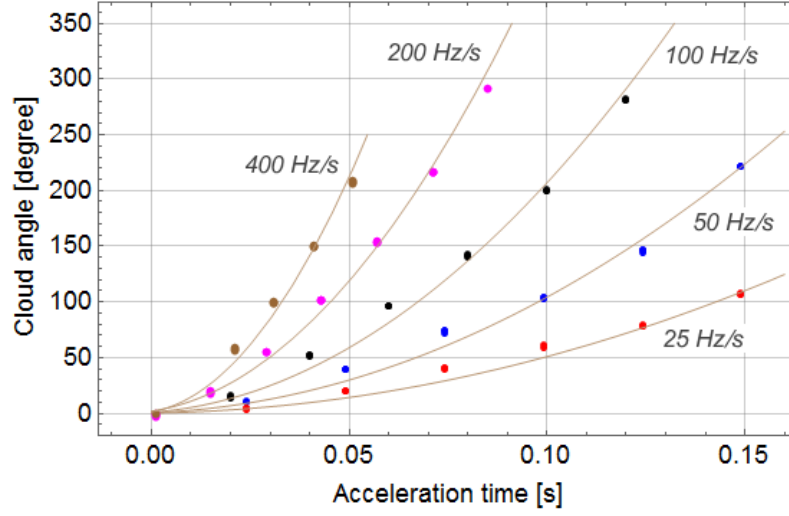


Figure 6.3: The angular position of the atom clouds for different accelerations, from  $2\pi \times 25 \text{ rad/s}^2$  to  $2\pi \times 400 \text{ rad/s}^2$ . The error in the data points are of the order of the point size. A small deviation in the center of mass angular position from the ideal trajectory, in the beginning of the acceleration, is due to the smaller phase jump programmed than the optimum, or any weak in-trap oscillation in the first static trap.

acceleration the ring radius increases and the azimuthal trapping frequency drops. I measured the azimuthal trapping frequency in both the static and the constant speed trap case, it decreases from  $9.17(3) \text{ Hz}$  (static trap) to  $7.76(1) \text{ Hz}$  ( $2\pi \times 10 \text{ rad/s}$ ), in  $0.2 \text{ s}$ . We fulfill the adiabatic condition – on the change of the trapping frequency in a given duration, i.e.,  $\dot{\omega} \ll \omega^2$  and thus no shape oscillations are excited along the azimuthal axis.

To estimate the ring radius increase due to the acceleration, we derive an equation for the ring radius against the angular speed by equating the centrifugal force and the gradient in the potential. In the harmonic limit, the ring radius increases with the angular speed, according to

$$R(\Omega) = \frac{R(0)}{1 - (\Omega/\omega)^2} \quad (6.1)$$

where  $\omega$  is the radial trapping frequency,  $\Omega$  is the angular speed, and  $R(0)$  is the in-trap radius. Our accelerator and the transport sequence is well within the harmonic regime. The ring radius changes from  $436(2) \mu\text{m}$  (static ring) to  $443.4(4) \mu\text{m}$  due to the angular acceleration up to  $2\pi \times 10 \text{ rad/s}$ , with a deviation of  $0.2\%$  from the predicted value.

## 6.3 Hypersonic transport of trapped BECs

### 6.3.1 Phase jump optimization

One very important parameter in the transport sequence is the amplitude of the trap (phase) jump at the beginning and end of the acceleration, before transporting the BECs at a constant speed. If the cloud oscillates at the first place, i.e., right after loading from the dipole, and the first jump happens at a time when the center of mass is not at rest and at the bottom of the potential, the cloud will not follow the ideal trajectory. The result will be in-trap oscillation of the cloud in the next constant speed trap. I first checked for any in-trap oscillation in the static trap, and measured none, or is the shot to shot non-periodic position stability of the trap. Then, went to optimize for both the trap jump amplitudes, fig. 6.4 shows the trap oscillation amplitude, measured after the acceleration is stopped and the cloud is transported at 10 Hz. The minimum oscillation amplitude, here, is  $\approx 0.8^\circ$  ( $\approx 7 \mu\text{m}$ ), in a ring trap of radius  $440 \mu\text{m}$ . The condensate azimuthal size is about  $12^\circ$  and clearly the oscillation amplitude is much smaller than the cloud size. Also, the minimum oscillation amplitude is linked with the tilted ring trap position stability, which is about  $10 \mu\text{m}$ , close to the minimum oscillation amplitude I measured.

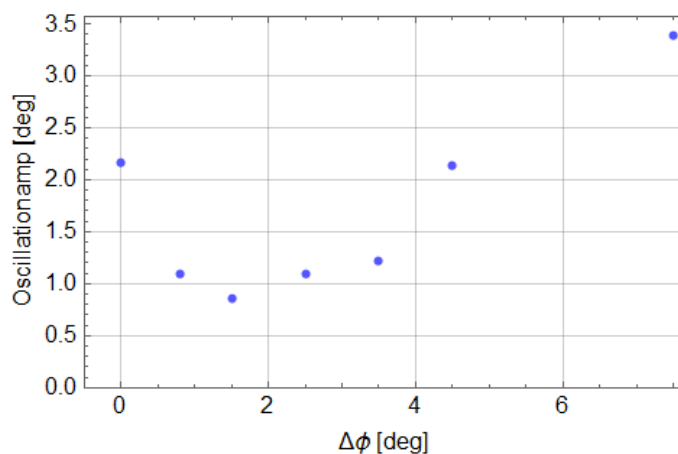


Figure 6.4: The azimuthal in-trap oscillation amplitude versus the amplitude of trap jump, for BEC transport at  $2\pi \times 10 \text{ rad/s}$ . The minimum oscillation amplitude is of the order of the trap position stability.

### 6.3.2 Transport Results

After accelerating the BECs at  $2\pi \times 50 \text{ rad/s}^2$ , for 200 ms, to a final angular speed of  $2\pi \times 10 \text{ rad/s}$ , we jump the trap back such that atom cloud center coincides with the moving

trap minimum. Fig. 6.5 shows the cloud angular position versus transport duration up to 14.276 s. The inset of the fig. 6.5 shows the bimodal distribution of the atom cloud after 44 round trips of transport. Fig. 6.6 shows the absorption images of BECs near the beginning of the transport sequence, very clear from the images that the atom cloud comes back to the initial position/angle after a 100 ms of travel time.

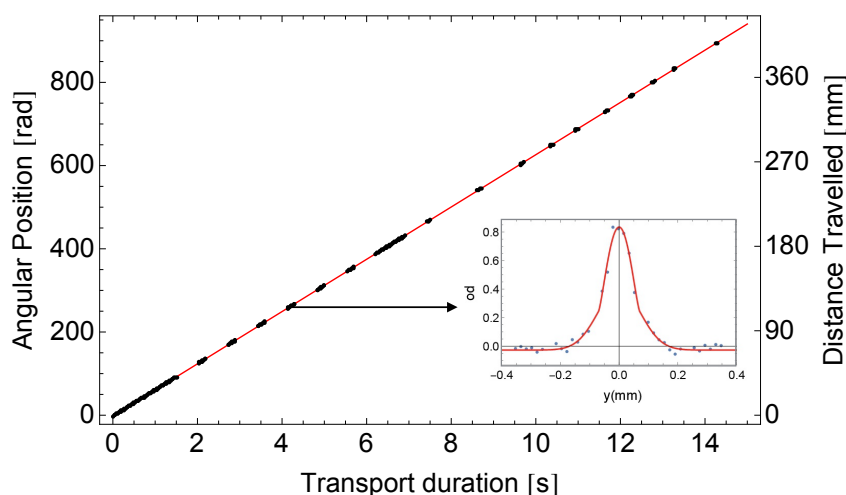


Figure 6.5: Long distance ultrafast transport of BECs in tilted ring traps, up to 14.276 s. The inset shows the bimodal density distribution of the atom cloud after a transport duration of 4.4 s, or 44 round trips.

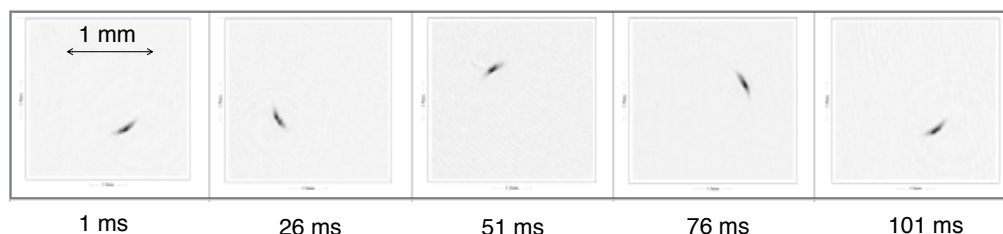


Figure 6.6: Absorption images of BECs during their transport in a 0.89 mm diameter tilted ring trap.

I stop the sequence at different transport duration to measure the atom number (used to calculate the cloud lifetime), cloud size (used to calculate the cloud temperature), and the radius (used to quantify the waveguide deformation), and the angular position of the atom cloud. The measured BEC lifetime in the static and the rotating ring trap is 1.3 s. The lifetime of the thermal cloud in the static and moving ring trap is 3.3 s. The radial and the azimuthal cloud size shows a very small oscillation at 10 Hz, with amplitudes  $2.3(\pm 0.5) \mu\text{m}$  and  $16(\pm 3) \mu\text{m}$ , over a mean size of  $54 \mu\text{m}$  and  $196 \mu\text{m}$ , respectively. The cloud radius while they are transported also shows a very weak oscillation at 10 Hz, with an amplitude  $4(\pm 1) \mu\text{m}$  over a ring radius of

443.4(4)  $\mu\text{m}$ . I start the accelerator sequence with  $3 \times 10^5$  nearly pure condensate, the sample at 60 nK, and measure  $1.1 \times 10^3$  atoms in the condensate after 4.4 s of transport. The heating rate of thermal cloud for both the static and moving trap is 3(1) nK/s. We do not observe any reduction in the lifetime and extra heating due to the center of mass motion of the condensate. More details of the characterization are given in the sections below.

### 6.3.3 The term *hypersonic*

We transport BECs at hypersonic speeds, where the speed of sound is linked with the density of the medium. In this context, speed of sound depends on the density of the Bose condensed atoms, trapped in the potential. There is a critical velocity (Bogoliubov speed of sound) where the maximum phonon-like excitation's are generated, given by [90]:

$$c = \sqrt{\frac{n U_0}{m}}, \quad (6.2)$$

where  $U_0 = 4\pi\hbar^2 a_{\text{Rb}}/M$  is the bosonic interaction parameter,  $a_{\text{Rb}}$  and  $m$  are the scattering length and mass of  $^{87}\text{Rb}$ , respectively.  $n$  is the density of the atoms in the condensate. For our weakly interacting gas, the density profile is parabolic, with the maximum density being at the center, or the maximum speed of sound occurring at the center. The peak density of the atoms is given by:

$$n_{\text{max}} = \frac{1}{8\pi} \left[ 15N \left( \frac{M\omega_{\text{ho}}}{\hbar\sqrt{a_{\text{Rb}}}} \right)^3 \right]^{2/5}, \quad (6.3)$$

where  $\omega_{\text{ho}}$  is the geometric mean of the three trapping frequencies, for our parameters it is 31.2 Hz. We work with  $N = 3 \times 10^5$  atoms in the condensate, from the equation above the calculated maximum speed of sound in the condensate is then 1.75 mm/s. The BECs are transported around the ring at a linear speed of  $v = \omega \times R = 2\pi 10 \text{ Hz} \times 443 \mu\text{m} = 27.8 \text{ mm/s}$ . This means that the BECs are travelling at a speed,  $27.8/1.75 = 16$  times higher than their maximum speed of sound. This is another strong evidence that TAAP rings, and other TAAP geometries are extremely smooth, making them an ideal candidate for atomtronic sensors and devices.

### 6.3.4 Micromotion of BECs

Figure 6.7 shows the deviation of the atom cloud angle/position from the straight line (uniform circular motion) as shown in the Fig. 6.5, while the tilted ring trap is moved at a constant angular speed. We observe micromotion [91] of BECs at the center of mass driving frequency 10 Hz and at its first harmonic, i.e., 20 Hz. It is due to the azimuthal potential variations in the static ring. If at the end of the acceleration the center of mass has not reached the right angular speed, in-trap oscillation of the cloud is expected at the azimuthal trap frequency. This can be avoided completely by knowing the initial phase of the in-trap oscillation, to adjust further the second trap jump, which could eliminate any velocity mismatch between the moving trap and the atom cloud. I fit three sine waves to the residual oscillation data, at 10 Hz, 20 Hz, and one frequency as a free parameter for the azimuthal trapping frequency. The subtracted data points are fitted to a function:

$$\phi(t) = \phi_0 + 2\pi 10 t + a_1 \sin(2\pi 10 t + \phi_1) + a_2 \sin(2\pi 20 t + \phi_2) + a_3 e^{-t/\tau} \sin(2\pi \omega_\phi t + \phi_3). \quad (6.4)$$

where  $(\phi_0)$  is an arbitrary starting phase, the second term corresponds to a uniform

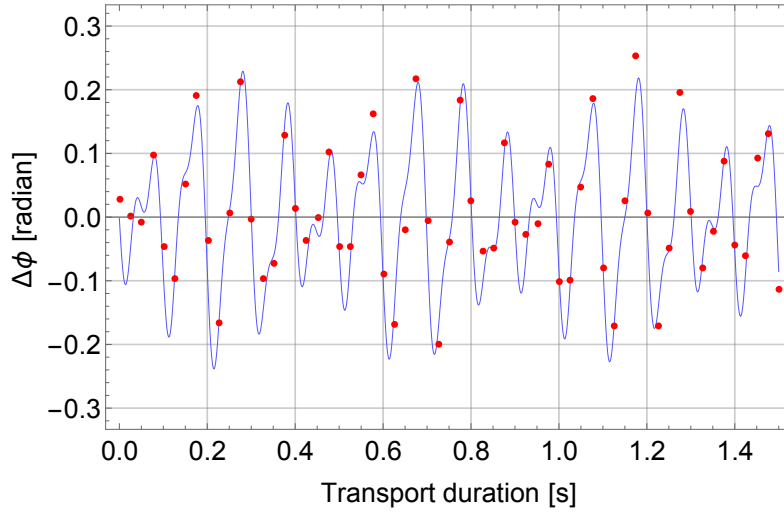


Figure 6.7: The deviation of the atom cloud angular position from the uniform circular motion, at  $2\pi \times 10$  rad/s.

circular motion at 10 Hz, the third and the fourth term represents the micromotion of BECs at the driving (transport) frequency (10 Hz) and its first harmonic (20 Hz), and the fifth term is for the in-trap oscillation along the azimuthal direction. The fit finds oscillation amplitudes at 10 Hz ( $a_1$ ), 20 Hz ( $a_2$ ), and  $\omega_{phi}$  ( $a_3$ ) to be 140 (10), 40 (10) and 70 (10) mrad, respectively. The fit provides the starting phase of the oscillations,  $\phi_0$ ,  $\phi_1$ ,  $\phi_2$  and  $\phi_3$  to be 2.2, 3.3, 3.5 and 0.5 rad, respectively. Also, for the whole transport

duration of 14.276 s, the fit does not detect any drift in the phase or amplitude at the driving frequencies, i.e., at 10 and 20 Hz. For the final term, in-trap oscillation during the transport, the fit finds a decay time constant ( $\tau$ ) of 5.3 s, and the azimuthal trapping frequency ( $\omega_\phi$ ) to be 7.76 (1) Hz.

### 6.3.5 Lifetime measurements

In order to characterize the efficiency of our BEC transport sequence, lifetime measurements were performed for both the cases i.e. in a static and moving trap. Figure 6.8 shows the thermal cloud lifetime measurement in the transport case, at  $2\pi \times 10$  rad/s angular speed. The data was fitted to a straight line, slope gives the  $1/e$  lifetime and the offset initial atom number. The fit finds  $1/e$  lifetime of 3.3 s.

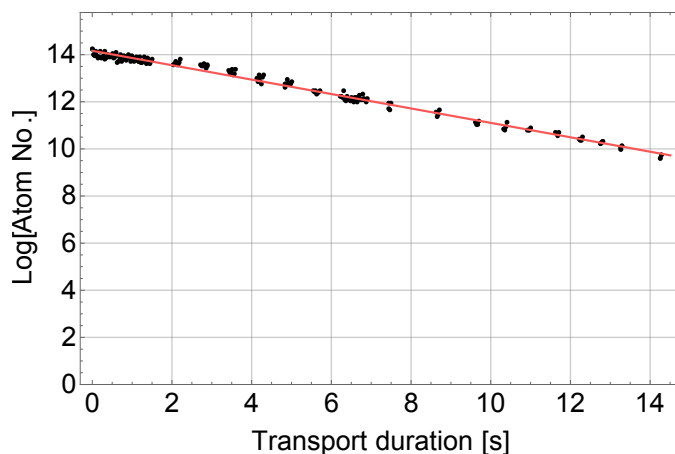


Figure 6.8: Lifetime measurement of the thermal cloud for the ultrafast transport case. On the  $y$ -axis, the logarithm is to the base 10.

For the Bose condensed atoms, Fig. 6.9 shows the decay in the condensate atom number for various transport duration. The fit provides a  $1/e$  lifetime of 1.3 s. I also measured the lifetime of the thermal and condensed cloud in a static tilted ring trap, after loading the atoms from the crossed-dipole trap. In the static trap, the measured lifetime of BEC and ultracold thermal cloud was 1.3 s and 3 s, respectively. Any reduction in the lifetime for the case where BECs are transported at very high speeds, would come from the extra heating (more than in the static case) of the sample. In the section below, I provide the heating rate measurements for the static and travelling atomic clouds.



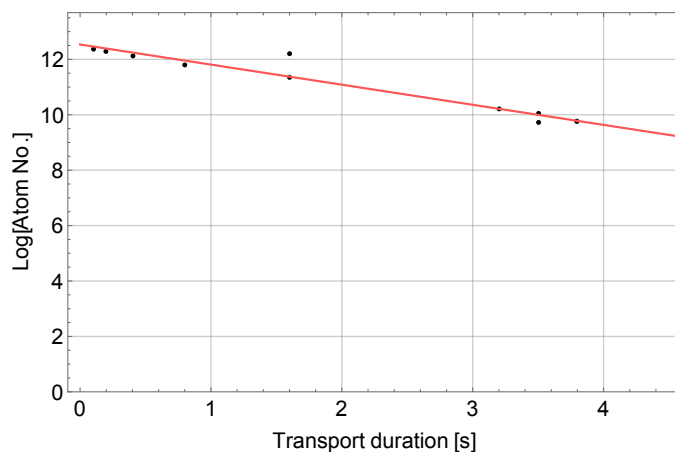


Figure 6.9: Lifetime measurement of the Bose condensed atom cloud for the transport case. On the  $y$  axis, the logarithm is to the base 10.

### 6.3.6 Heating rate measurements

To measure the effect of the hypersonic transport on the heating rate of the atom cloud, I measured the temperature of the ensemble after various transport duration in the ring trap, and compared with the values if a BEC is trapped in a static titled ring trap. Figure 6.10 shows the measured temperature of the atom cloud after various transport duration in the ring. The data is fitted with a straight line, of the form,  $y = mt + c$ , where  $m$  is the slope, or the heating rate, and  $c$  is the initial temperature of the cloud. The two cases have different initial temperatures, by about 20 nK, due to a different final power of the dipole beams at the end of the evaporation. The heating rate is not effected by this small difference in the initial temperature unless one enters into a regime where other loss mechanisms start to play a role.

For both the static and travelling ring trap, the fit finds a slope of 3 (1) nK. Any extra heating due to the transport of the atom cloud is only 1 nK/s, corresponding to 32 pK/mm. The starting temperature for the static and moving case, is 83 nK, and 62 nK, respectively. It is clear from the data that there is a fast rise in the temperature in both the cases, for duration less than 2 s, and later slow. For the static case, if the data is fitted in two sections, the fit gives heating rates of 24 nK/s and 4 nK/s for  $< 2$  s and  $> 2$  s of trap hold duration, respectively. This indicates towards a higher heating of the sample when the ensemble has a larger BEC fraction compared to the pure thermal case. For the moving case, again, if the whole data in divided in two sections, the fit finds heating rates of 11 nK/s and 0.4 nK/s for  $< 2$  s and  $> 2$  s hold times, respectively. These tiny values of the heating rates is due to the smoothness of the TAAP potential, other one explained in section 6.4.

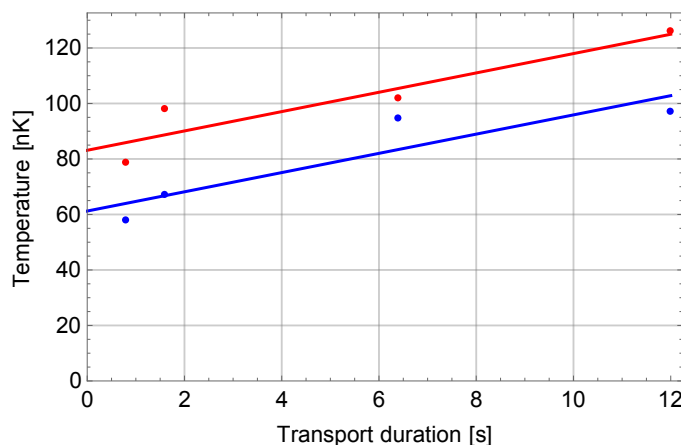


Figure 6.10: Blue: temperature of the atom cloud in a travelling ring trap, at  $2\pi \times 10$  rad/s, for different duration of transport. Red: temperature of the atom cloud in a static tilted ring trap.

### 6.3.7 Shape oscillations

From the BEC transport data, taken from the vertical imaging, I plot the radial and the azimuthal size of the condensed cloud for different transport times. Figure 6.11 shows the azimuthal size of the atom cloud (thermal) for up to 1 s of transport, at an angular speed of  $2\pi \times 10$  rad/s. The reason to analyze the data up to 1 s is that in the long run, there is no continuous data points. The data is fitted to a function:

$$\Delta\phi(t) = \tau(t - t_0) + a_1 \cos(2\pi f_\phi t + \phi_0) \quad (6.5)$$

where  $\tau$  is a slope in the decay of the mean azimuthal size of the cloud,  $t_0$  corresponds to the initial size (offset),  $a_1$  is the oscillation amplitude,  $f_\phi$  is the size oscillation frequency, and  $\phi_0$  is an arbitrary starting phase. From the fit, I find the values of  $\tau$ ,  $t_0$ ,  $a_1$ ,  $f_\phi$ , and  $\phi_0$  to be,  $21$  (7)  $\mu\text{m/s}$ ,  $9$  (3) s,  $16$  (3)  $\mu\text{m}$ ,  $10.1$  (1) Hz, and  $0.6$  (3) rad, respectively. It is not surprising that the size oscillates at the frequency which is center of mass driving frequency, i.e., 10 Hz, and the amplitude of the oscillation is about 10%, the points away from the ideal sin (cos) curve is due to the initial fluctuation in the atom number (size). The linear decay in the size is linked with the reduction in the number of atoms as the transport time increases.

Next, let us look at the radial size of the atom cloud as it is transported in tilted ring traps. Figure 6.12 shows the radial size of the atom cloud, imaged from above with the vertical imaging. We do see a small oscillation in the radial size, again at 10 Hz. The data

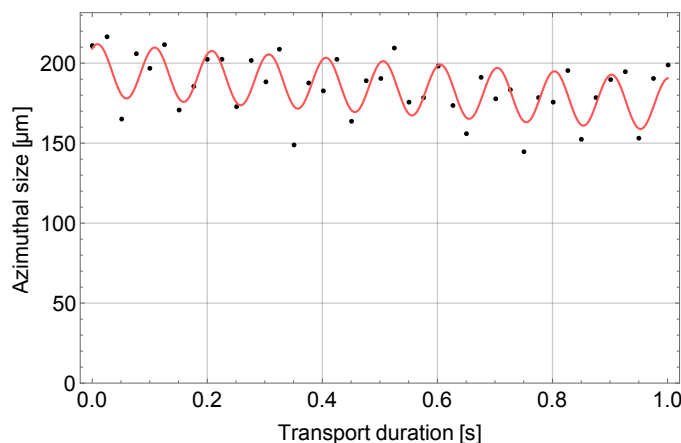


Figure 6.11: The azimuthal size of the atom clouds during their first second of transport.

is fitted to an equation:

$$\Delta r(t) = \tau(t - t_0) + a_1 \cos(2\pi f_{\text{rad}}t + \phi_0) \quad (6.6)$$

where  $\tau$  is a slope, for the mean radial size to increase (decrease),  $t_0$  corresponds to the initial size (offset),  $a_1$  is the oscillation amplitude of the radial size,  $f_{\text{rad}}$  is the oscillation frequency, and  $\phi_0$  is an arbitrary starting phase. From the fit, I find the values of  $\tau$ ,  $t_0$ ,  $a_1$ ,  $f_{\text{rad}}$ , and  $\phi_0$  to be, 1 (1)  $\mu\text{m}/\text{s}$ , 44 (43) s, 2.3 (5)  $\mu\text{m}$ , 10.0 (1) Hz, and 0.5 (4) rad, respectively. Essentially, the radial size of the cloud remains unchanged, but it does oscillates at the frequency we move the tilted ring trap.

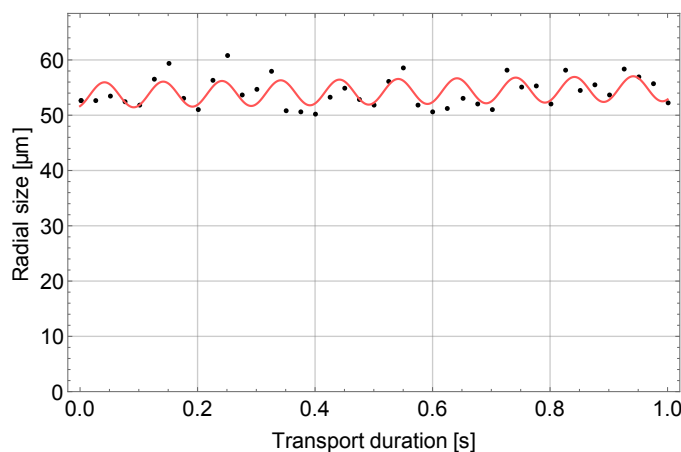


Figure 6.12: The radial size of the atom clouds during their first second of transport.

### 6.3.8 Ring radius

During the long distance BEC transport, I looked at the stability of the cloud (ring trap) radius. Figure 6.13 shows the radius for up to 1 s of transport. The data is fitted to a cosine wave, with a function of the form:

$$r(t) = r_0 + a_1 \cos(2\pi f_r t + \phi_0) \quad (6.7)$$

where  $r_0$  is the mean radius,  $a_1$  is the oscillation amplitude,  $f_r$  is the oscillation frequency in the radius of the cloud, and  $\phi_0$  is an arbitrary starting phase. The fit finds an offset (mean) radius of  $443.4(4) \mu\text{m}$ . The oscillation amplitude from the fit is  $4(1) \mu\text{m}$ . The frequency of the oscillation in the radius is  $9.9(1) \text{ Hz}$ , and we transport the atoms at  $10 \text{ Hz}$ . The percentage oscillation in the radius of travelling BECs is  $\sim 1\%$ , at the driving frequency. The deviation of the points from the  $10 \text{ Hz}$  oscillation is mainly due to the trap position stability, is less than  $10 \mu\text{m}$ .

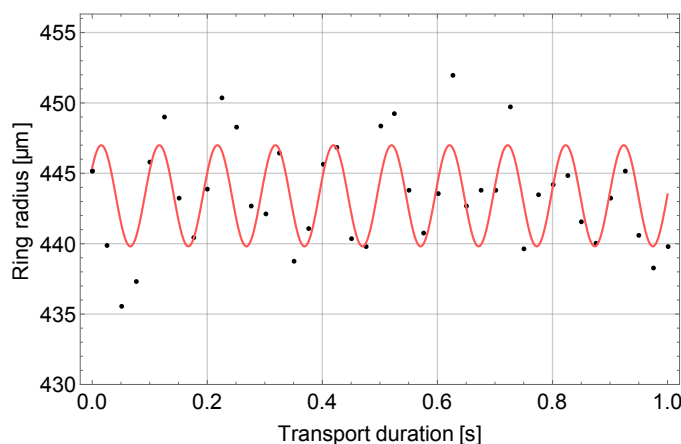


Figure 6.13: The radius of the atom cloud (effective azimuthal minimum of the ring trap) as the BECs are transported in tilted ring traps, at an angular speed of  $2\pi \times 10 \text{ rad/s}$ .

## 6.4 Ring flatness with circulating atoms

An alternate way to test the smoothness of our potential is to launch BECs into the flat ring waveguide and measure the heating rate, lifetime, and the decay time of the angular motion of the atoms. To do that, nearly pure BECs containing  $\sim 10^5$  atoms were first accelerated up to angular speeds of  $2\pi \times 10 \text{ rad/s}$  and then launched into the waveguide by slowly ramping down the azimuthal tilt amplitude, see fig. 6.14 lower

row. Once in the waveguide, atoms see the modulation of static ring at  $\phi$  and  $2\phi$  (we fit the azimuthal atomic density distribution to the eq.5.3). We established a relation between the variation in the atomic density along the azimuthal direction for the moving atoms and the height of the potential modulation. One can start by assuming that a fluid flows with velocity  $v$  through a landscape containing dips and hills, and keeping the flux constant. In the case of steady flow, the flux is given by the multiplication of  $v$  and the density per unit area and time. The difference in the kinetic energy at different points in the landscape is simply the difference in the potential energy between them. The fractional change in the flow velocity corresponds to the one in the atomic density. In the presence of a barrier of energy height  $\Delta E$  and assuming the flow is in a circle of radius  $r$  at an angular speed  $\Omega$ , the variation in the density (velocity) is:

$$\Delta v/v = \Delta n/n = -1 + \sqrt{1 + \frac{2\Delta E}{mv^2}} \quad (6.8)$$

where  $v$  is the linear velocity, equal to the product of the radius and the angular speed.

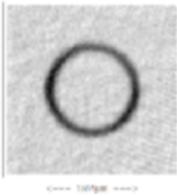
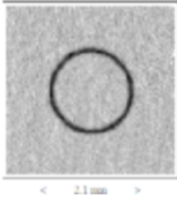
Case	Image	Hold time [s]
Static atoms		6.5
Moving atoms		1

Figure 6.14: Two absorption images, upper row:  $10^6$  thermal atoms at a temperature 430 nK are loaded into a flat ring waveguide, the atoms do not have any angular motion, and the image taken after 5.3 ms of ToF. Lower row:  $10^5$  BEC, sample at a temperature 28 nK, is first accelerated up to  $2\pi \times 10$  rad/s, launched into a flat ring waveguide, and then imaged after 1 s of hold, and 6 ms of ToF.

For the angular speed of  $2\pi \times 10$  rad/s in the experiment, I calculate the density variation to be 0.001%, and 0.0006%, for the  $\phi$  and  $2\phi$  tilt, respectively. The angle of the minimum (maximum) density jumps over the entire  $2\pi$  (anywhere in a circle), shot to shot. It is a strong indication that the density variation we observe is not due to the static ring potential but is a limit of our detection. The measured sample temperature is 28 nK and thus the effective flatness of the atomic density in the waveguide is 189 pK. In length units, the temperature 189 pK translates to 1.8 nm height difference along the

waveguide, from  $k_B T = mgh$ . From the azimuthal density modulation in the case of static atoms (no angular motion), see fig. 6.14 upper row, I calculate a maximum effective potential modulation of 250 nK. Also, we did not see any decay in the angular speed of the atoms over a timescale absorption image can detect the atoms in the ring, up to 10 s. The lifetime and the heating rate in this case (atoms not trapped in a tilted ring but moving in a flat waveguide) is similar to the one where BECs are transported in tilted ring traps.

## 6.5 The radius of circulating atoms in ToF

The radius of the ring waveguide containing moving atoms is different than if it contains static atoms, i.e., no angular motion, according to the eq. 6.1. The radius of the ring in the upper row of fig. 6.14 is  $476 \mu\text{m}$ , after 5.3 ms of ToF, and the radius of the ring in the lower row is  $517 \mu\text{m}$ , imaged after 6.3 ms of ToF. The difference in the radius between the static and the moving case is magnified in the time-of-flight, follows the relation:

$$R(t) = R(0)\sqrt{1 + (\Omega t)^2} \quad (6.9)$$

where  $R(0)$  and  $\Omega$  are the in-trap waveguide radius, and the angular speed of the moving atoms. The idea behind the relation can be seen in the fig. 6.15. Let us assume that a particle is tied to a rope and is undergoing circular motion, breaking the rope will result in a linear motion of the particle in the direction tangential to the circle. The linear velocity with which the particle will keep on moving, will be,  $v = R \times \Omega$ , and the distance travelled in time  $t$  will be  $s = vt = R(0)\Omega t$ . By just following the right angle triangle rule, the radius after a certain ToF can be known. I also used this method to calculate the angular speed of the atoms, after they are launched into the flat ring waveguide and fills the whole ring. In the case of lower row of fig. 6.14, measured  $\Omega$  is  $2\pi 10.01(\pm 0.06)$  rad/s and the acceleration was stopped at  $2\pi 10$  rad/s.

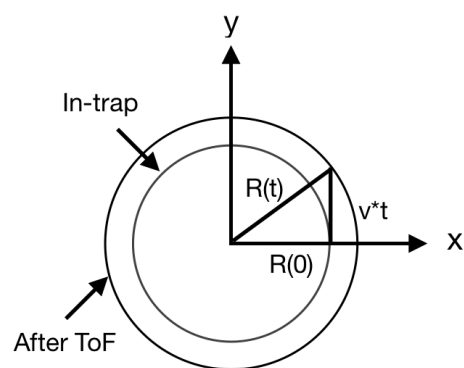


Figure 6.15: The radius of the atom cloud after the ring trap is switched off, for the case where the atoms have angular motion.

## Chapter 7

# Atom optics in the ring waveguide

### Motivation

Early versions of the atom optical elements were micro-fabricated gratings [92, 93, 94] and optical lattices [95, 96]. With the use of laser beams as atom optical elements, implementation of atom interferometers were reported in Raman [95] and Bragg configurations [97]. Today most of the atom interferometers use these methods as beam splitters to coherently split and recombine the atomic states. The shape and orientation of the interferometer loop is of major importance in determining which property of the non-inertial frame is under observation. Different trajectories of the atomic wave-packet motion in a matterwave guide have been studied, e.g. in a linear waveguide [23] or a number 8 shaped waveguide [98]. With the aim of developing high sensitivity rotation sensors [99, 57] and to pursue fundamental research [18, 58], ring-shaped magnetic [59, 60, 100, 61] and optical [63, 62] potentials have been implemented.

I have systematically studied the key elements of Sagnac-type guided atom interferometers based on the TAAP ring traps and waveguides. We proposed [61] two types of Sagnac interferometers, using 1) spin, and 2) momentum states in TAAP rings. For the first type, I presented one of the most important requirement for a guided clock-type ring interferometer in chapter 5, i.e. state dependent trapping and independent manipulation of the two internal states of  $^{87}\text{Rb}$  in a ring trap. In chapter ??, I provided results for the long distance, excitationless transport of BECs and ultracold clouds in moving TAAP ring traps. An ultracold atom cloud was transported up to a total distance of 40 cm (equivalent to 143 round trips) and BECs up to 15 cm (equivalent to 53 round trips) in a ring trap of  $444 \mu\text{m}$  radius at an angular speed of  $2\pi \times 10 \text{ rad/s}$ . This will provide an unprecedented gain in the sensitivity since the Sagnac phase scales



linearly with the area of the closed loop, or, equivalently with the number of round trips if the area is kept fixed. The second type we proposed is based on the coherent manipulation the atomic momentum states. In this case, the beam splitter and mirrors will be made of Bragg pulses [97] or Raman transitions [95]. Due to the absence of azimuthal trapping confinement in the second type, the atomic cloud expands at a rate given by the finite temperature or chemical potential in the case of thermal ensemble or BEC, respectively. The spreading of the guided wave-packet during the interrogation time is detrimental to the interference fringe contrast [101]. With the use of delta-kick cooling technique [102, 103, 104], an atomic beam can be collimated, and focused, and thus helps in achieving long interrogation times. Delta-kick cooling technique has been utilized in the free fall [105, 106] and guided atom interferometers [23]. In this chapter, I focus on minimizing the azimuthal momentum spread of guided atomic wave-packets using the delta-kick technique method in a ring geometry. I provide results for both the focusing and collimation of BECs launched in a ring waveguide.

## 7.1 BEC launch into the ring waveguide

Center-of-mass (COM) acceleration of BECs and ultracold thermal atom clouds in our TAAP ring waveguides is done via the bang-bang technique, under the formulation of inverse engineering method and optimal control theory (OCT) [48]. Starting from rest and to reach a final COM angular speed of  $\dot{\phi}_f$ , the trap is first jumped forward by  $\Delta\phi$  and then accelerated at  $\ddot{\phi}$ . The trap jump amplitude ( $\Delta\phi$ ) and the acceleration ( $\ddot{\phi}$ ) are related by  $\Delta\phi = +\ddot{\phi}/\omega^2$  where  $\omega$  is the ring azimuthal trapping frequency. To eliminate any deviation from the programmed acceleration  $\ddot{\phi}$  due to the in-trap oscillation in the initial static tilted ring trap, first trap jump can consist of two jumps, separated by a small hold time (of the order of the ring azimuthal trapping frequency). If there is any center of mass oscillation after loading the atoms into a tilted, one waits for a quarter of the trapping period until the center of mass velocity reaches zero, and then jump the trap to that position, catches the cloud in the new trap minimum. A second trap jump is programmed right before the trap is accelerated. Upon reaching the final angular speed of  $\dot{\phi}_f$ , the trap is jumped back by  $\Delta\phi$ . The acceleration is stopped at an angular speed of  $\dot{\phi}_f$  and BECs are then launched into a horizontal ring waveguide by slowly ramping down the azimuthal tilt  $\delta$  to 0. We then manipulate the azimuthal spread of the atomic cloud with an azimuthal kick-pulse.

Figure 7.1 shows absorption images of BECs after their acceleration and launch into the flat ring waveguide, for different hold times in the trap. The atoms freely

propagate in this no-azimuthal-confinement ring trap. The experimental sequence is same as in the case of BEC acceleration, only that after reaching an angular speed of  $2\pi \times 10$  rad/s the trap is jumped backwards, and the azimuthal tilt is removed completely in 50 ms. This experiment was done with about  $2 \times 10^5$  atoms in the condensate. The measured angular speed of the center of mass after the launch is  $2\pi \times 10.07(1)$  rad/s. As I explained in the section above, since we have switched off the

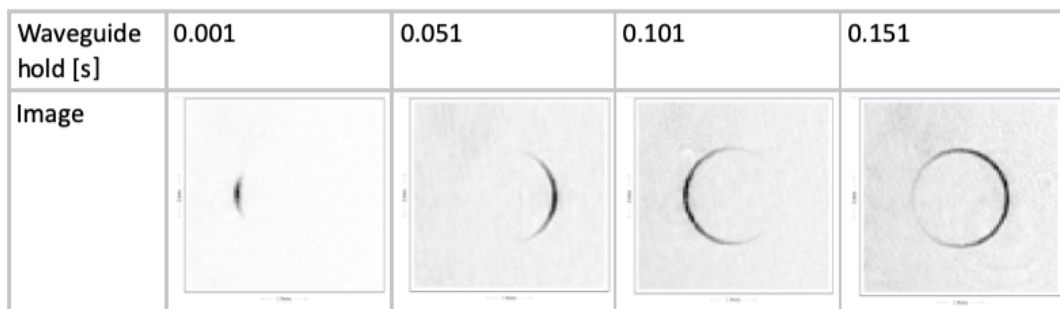


Figure 7.1: BEC expansion in the flat ring waveguide after the atoms are accelerated and the azimuthal tilt is ramped to zero. The center of mass angular speed of  $2\pi \times 10$  rad/s is very clear from these absorption images, i.e., the atoms come back to the same point/angle after 100 ms of travel. The time-of-flight for this experimental sequence was 2.3 ms.

azimuthal tilt, now the atoms travel around the ring and at the same time the azimuthal size increases. This is not very useful if we want to have long interaction times of the interferometer, and will result in a lower contrast of the interference fringes. The atoms fill the whole ring waveguide after about two round trip travel depending on the temperature (chemical potential) of the thermal cloud (BEC). Fig. 7.2 shows absorption images of the BECs for various long hold times in the ring waveguide, and after a long time of flight. The spirals are formed due to the difference in the angular speed of the atoms in the two halves, azimuthally. This is because the center of mass moves forward, one part of the cloud moves in the direction of it and the other part away, the net is the difference in the angular speed between the two portions. The bimodal density distribution of the atoms retains up to some six, seven round trips.

In the sections below, I provide collimation and focusing results of the ultracold thermal and condensed atom clouds in our TAAP ring waveguides.

## 7.2 The azimuthal lens

After the launch, we let the atoms propagate around the ring at  $\dot{\phi}_f$  for a waveguide expansion time of  $\Delta t_0$ .  $\Delta t_0$  is set large compared to the azimuthal trapping period

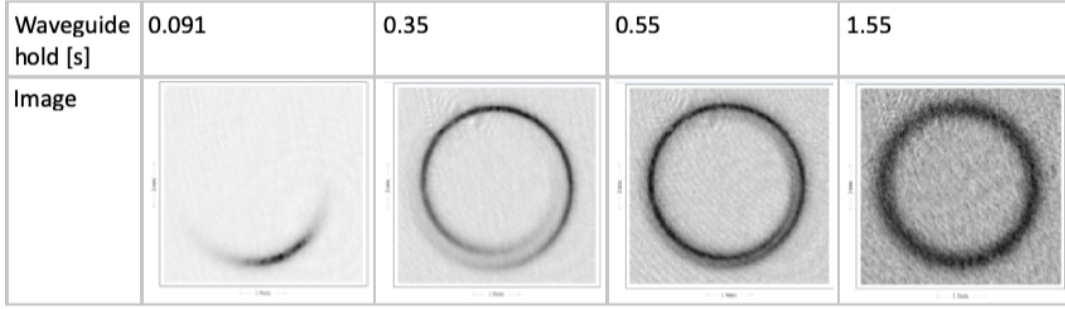


Figure 7.2: BEC propagation in the ring waveguide after the launch, for long hold times. Time-of-flight for these experimental sequence were 19 ms. The spirals are visible only for the long time-of-flights, and are formed because of the angular speed variation along the azimuthal axis.

( $1/\omega_\phi$ ). After a long free expansion along the azimuthal direction, atoms with different momentum ( $p$ ) spread spatially following the linear momentum relation  $p(\phi) = mR(\phi - \phi_0)/t_e$  where  $\phi_0$  is the center angular position of the cloud and  $(\phi - \phi_0)$  is the azimuthal spread of the cloud after an expansion time  $t_e$  (see Fig. 7.3a). The azimuthal size of the cloud increases with  $\Delta t_0$  at a rate determined by its temperature (or chemical potential for BECs) and eventually atoms fill the whole ring. This prevents using a closed loop waveguide for applications where the wave packet needs to be well localized. One therefore can use a harmonic lens potential to impart a position dependent impulse onto the atoms and thus reduce the expansion rate of the travelling cloud [102, 103]. To achieve very low temperatures, it is required to expand the cloud by a large factor before a kick pulse is applied [102]. In a closed loop geometry, there is an upper limit on  $\Delta t_0$  given by the finite length of the waveguide together with the cloud expansion rate. We generate the azimuthal lens potential by

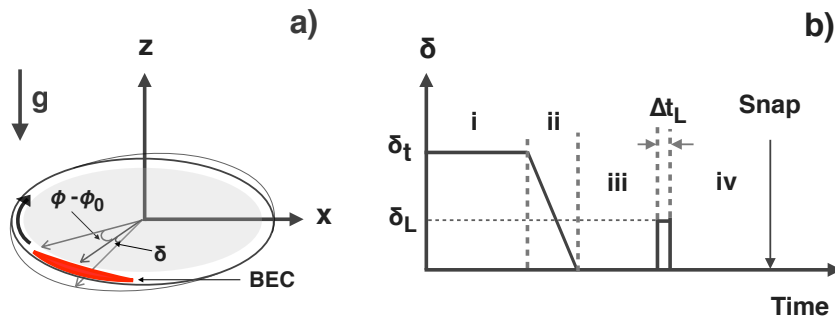


Figure 7.3: a) A cartoon showing the atom cloud propagating around the ring waveguide together with the lens potential, which is just a tilted waveguide. b) The azimuthal tilt amplitude, starting from the BEC acceleration (i), launch into the waveguide (ii), free propagation (iii), application of the lens, second free propagation (iv) before imaging the atoms.

tilting the ring waveguide itself by a small angle ( $\delta \leq 0.3$  rad) at the position of the

cloud (see Fig. 7.3a). The delta-kick pulse amplitude  $\delta$  sets the lens trapping frequency and it is varied to achieve different expansion slopes of the cloud. We choose the kick pulse duration ( $\Delta t_L$ ) for it to be very short compared to the lens trapping period ( $1/\omega_L$ ) along the azimuthal direction [102]. Fig. 7.3b shows the tilt amplitude  $\delta$  for our atom optics sequence, starting from the BEC acceleration, launch into the waveguide and finally a delta-kick pulse before the atoms are absorption imaged.

### 7.3 Experimental sequence

The atom optics sequence begins by adiabatically loading about  $2 \times 10^4$  Bose-condensed atoms in a tilted ring trap from a crossed-dipole trap. In a static tilted ring trap, the magnetic quadrupole field gradient is  $\alpha = 70 \text{ Gpcm}$ .  $xy$  and  $z$  audio-frequency fields oscillating at 5.02 kHz ( $\omega_m/2\pi$ ) have amplitudes 0.55 G and 1.4 G, respectively. This corresponds to a tilt amplitude of  $\delta = 0.37 \text{ rad}$ . The rf-dressing field along the  $z$  direction has a Rabi frequency  $\Omega_{\text{rf}}/2\pi \approx 357 \text{ kHz}$  and the rf-field frequency is  $\omega_{\text{rf}}/2\pi = 2.55 \text{ MHz}$ . The measured radial, axial and the azimuthal trapping frequencies in a tilted ring trap are 85.3(4) Hz, 46.2(3) Hz, and 9.17(3) Hz respectively. Following the method described in the previous chapter, we accelerate BECs at  $2\pi 50 \text{ rad/s}^2$  up to an angular speed of  $2\pi 10 \text{ rad/s}$  in 0.2 s. The centrifugal expansion on the atoms during the acceleration causes the cloud radius to increase from  $436(2) \mu\text{m}$  in a static ring to  $443.4(4) \mu\text{m}$  at  $2\pi 10 \text{ rad/s}$ . We measure a small drop in the azimuthal trapping frequency due to the outward expansion, from the 9.17(3) Hz to 7.76(1) Hz in the final moving trap [107].

### 7.4 Atom optics with ultracold thermal atoms

To perform the momentum spread manipulation, we launch the atoms into the waveguide by ramping down  $\delta$  from 0.37 rad to 0 in 50 ms. We then image the cloud after a variable expansion time in the waveguide. The expansion slope is calculated by fitting the  $1/e^2$  half-width azimuthal size of the cloud versus the waveguide expansion time ( $t_e$ ) to the function:

$$\Delta l(t) = \sqrt{\Delta l_0^2 + v^2(t - t_0)^2} \quad (7.1)$$

where  $\Delta l_0$  is the size after the lens is switched off,  $v$  is the expansion slope, and  $t_0$  is the time the cloud takes to reach the focus. The one-dimensional temperature along the azimuthal direction is calculated using the relation  $1/2mv^2 = k_B T$ . We start by studying

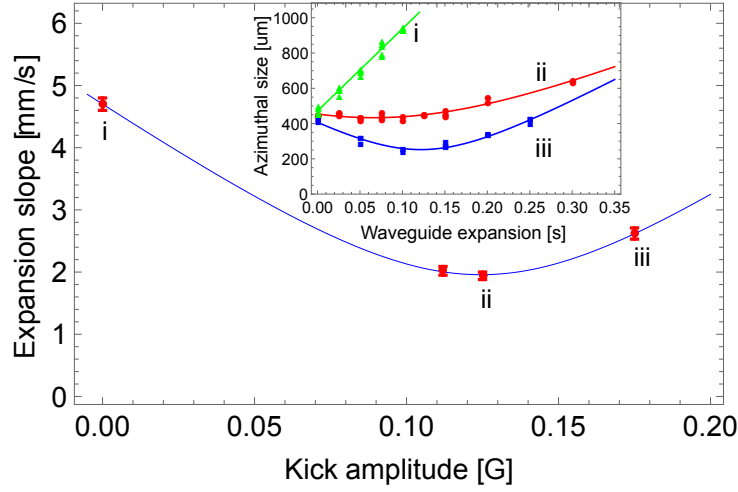


Figure 7.4: Azimuthal expansion slopes of ultracold thermal atoms as a function of the kick pulse amplitude. Inset shows the azimuthal size versus the waveguide expansion time for different pulse amplitudes, labelled as i) 0 G (triangle) – diverging, ii) 0.125 G (circle) – collimated, and iii) 0.175 G (square) – focused atomic beam.

the dependence of the expansion slope of the ultracold atoms on the kick pulse amplitude and keeping the pulse duration fixed. At this optimization stage, we launch  $6 \times 10^4$  atoms at  $116^{+5}_{-5}$  nK into a flat ring waveguide, followed by a free expansion of  $\Delta t_0 = 66$  ms in the waveguide. Fig. 7.4 shows the expansion slope of the atom clouds for different kick pulse amplitudes for a fixed pulse duration of  $\Delta t_L = 17$  ms. The audio-frequency fields amplitude and polarization can be switched on (off) in a timescale of less than a millisecond, generating a well-defined kick pulse. We find a minimum expansion slope of  $2.0(1)$  mm/s for 0.125 G ( $\delta = 0.09$  rad) kick pulse amplitude, corresponding to a temperature of  $22^{+2}_{-2}$  nK. The temperatures measured via the expansion in the waveguide agrees well with that of the time-of-flight method.

## 7.5 Atom optics with Bose-condensed atoms

### 7.5.1 Collimation of the guided matterwaves

Here I will describe the BEC collimation results. Fig. 7.6 shows the azimuthal evolution of the thermal and Bose condensed atoms as the cloud travels around the ring waveguide, with and without the delta-kick pulse. Before we start the measurements, the cloud is allowed to expand in the waveguide for  $\Delta t_0 = 135$  ms for both the kicked and no-kick case. It is a long expansion compared to the azimuthal trapping period of

20.4 ms (azimuthal trapping period at the end of acceleration). For the no-kick case, we fit the cloud azimuthal size versus the expansion time to a straight line since the atoms follow linear momentum relation after a long free expansion. The fitted expansion slopes are 3.4(3) mm/s for the thermal cloud (empty circles in Fig. 7.6) and 3.0(3) mm/s (empty squares in Fig. 7.6) for the BEC. These expansion slopes correspond to kinetic temperatures of  $60_{-11}^{+12}$  nK for the thermal cloud and  $48_{-8}^{+8}$  nK for the BEC. In a different experiment, a kick pulse was switched on for a duration  $\Delta t_L = 17$  ms, and  $\delta = 0.07$  rad. Fig. 7.6) shows the BEC and thermal cloud expansion in the waveguide after the pulse is turned off. For the BECs, we fit its azimuthal size to a straight line and the thermal sizes were fit to Equ. 7.1. With the kick pulse, we find expansion slopes of 1.7(1) mm/s and 0.56(3) mm/s for the thermal cloud and BEC, respectively. These expansion slopes translate to kinetic temperatures of  $1.6_{-0.2}^{+0.2}$  nK for the BEC and  $16_{-1}^{+2}$  nK for the thermal cloud. Fig. 7.5 shows the absorption images of atom clouds for different waveguide expansion times, with and without the kick potential applied.

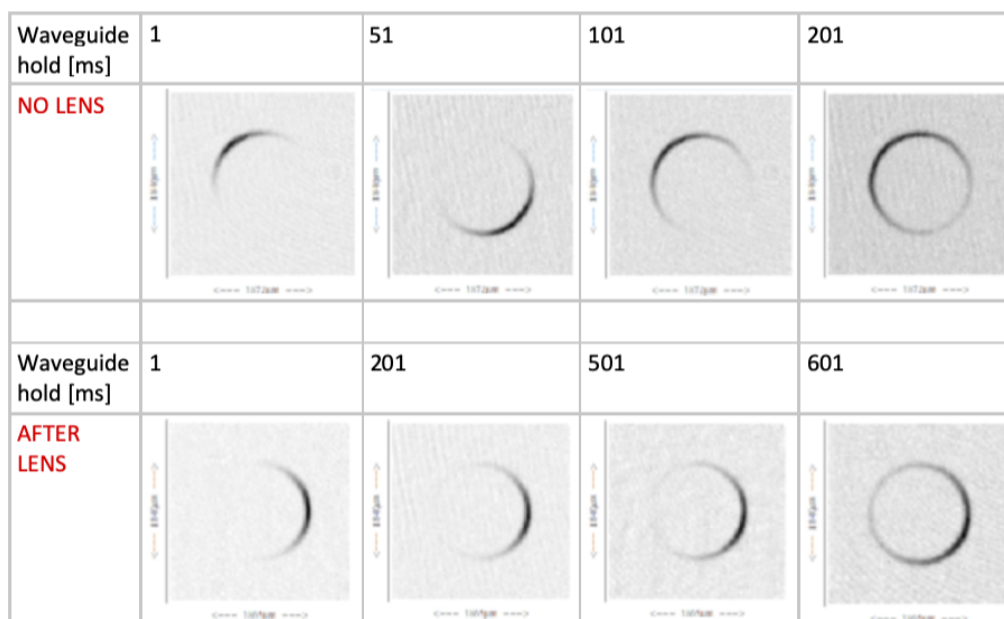


Figure 7.5: Absorption images of the ultracold atom clouds after the collimation pulse is applied, for different waveguide expansion times. The images were taken after a time-of-flight of 5.3 ms.

Comparing with the no-kick case, this corresponds to a reduction in the effective temperature of the BEC by a factor of about 30. For the thermal cloud, the temperature drops by about a factor of 4. We measure the center-of-mass angular speed of the cloud after the kick pulse to be  $2\pi \times 10.07(1)$  rad/s, while the targeted value was  $2\pi \times 10$  rad/s. Along the radial direction, the ground state harmonic oscillator energy is 2 nK ( $1/2 \hbar\omega_r$ ) and we measure  $33_{-9.5}^{+10.4}$  nK the condensate chemical potential from

the free fall radial expansion. It clearly indicates that we are working with BECs in the 3D regime. We observe a small variation in the atom cloud radius  $R$  as it travels around the waveguide after the kick pulse is switched off.  $R$  drops by  $\sim 2\%$  up to 0.2s and then reaches a steady value of  $R = 512(2)\mu\text{m}$ , and the estimated value due to the centrifugal expansion of the waveguide is  $511.3\mu\text{m}$ .

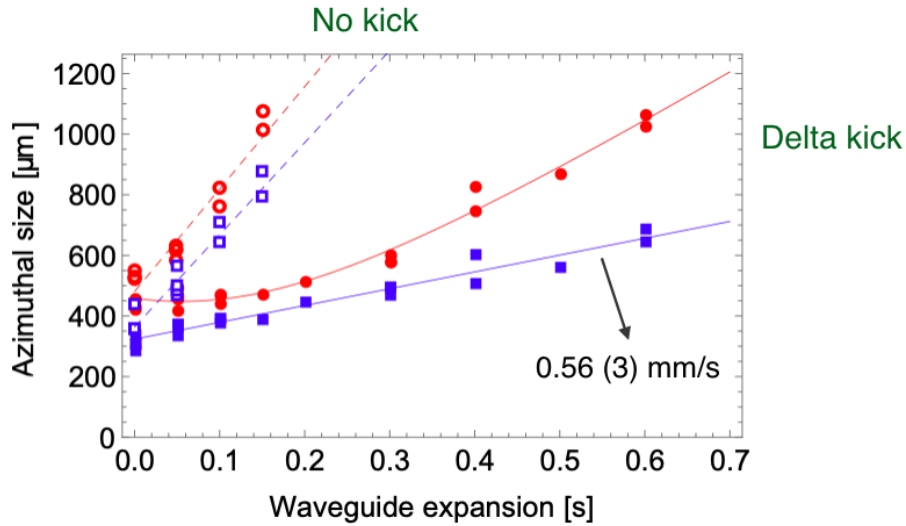


Figure 7.6: BEC collimation in the ring waveguide. The cloud is travelling at an angular speed of  $2\pi \times 10$  rad/s in a waveguide of perimeter 3.05 mm. The dashed lines show the no-kick expansion of thermal atoms (empty circle) and BEC (empty square). With the kick pulse, solid lines show the thermal cloud (filled circle) and BEC (filled square) expansion in the waveguide. The kick pulse is switched off at  $t = 0$ . The cloud is absorption imaged after a time-of-flight of 5.3 ms for the all the data points.

## 7.5.2 Focusing the guided matterwaves

Next, I studied focusing of BECs propagating around the waveguide. The experimental sequence is similar to the collimation case and the difference is only in the kick pulse parameters. BECs containing  $2 \times 10^4$  atoms are accelerated up to an angular speed of  $2\pi 10$  rad/s and launched into the ring waveguide. Before switching on the lens, the clouds expands freely along the azimuthal direction for  $\Delta t_0 = 50$  ms. A kick pulse is then switched on at  $\delta = 0.28$  rad and  $\Delta t_L = 20.4$  ms. Fig.7.7 shows the absorption images of BECs for different waveguide expansion times after the kick pulse is switched off. We define the focusing time ( $\Delta t_F$ ) as the time it takes from the pulse application to the cloud reaching its smallest size. From Fig.7.8, it is clear that the BEC takes longer to reach the focus than the thermal cloud (see Fig.7.8). It is due to the different quadrupole

shape oscillation frequency for the thermal cloud and BEC [108, 109]. In a very elongated trap, the theoretical ratio of the BEC and thermal quadrupole oscillation frequency is  $\omega_{\text{BEC}}/\omega_{\text{th}} = 1.3$  [109]. It is therefore not surprising that the thermal cloud focuses first and then the BEC. We calculate the ratio between the focusing times of the BEC and thermal cloud and it is about 1.5. The radial size of the thermal cloud and BEC goes up by about a factor of two, comparing the size at the focus and size right after lens potential is switched off.

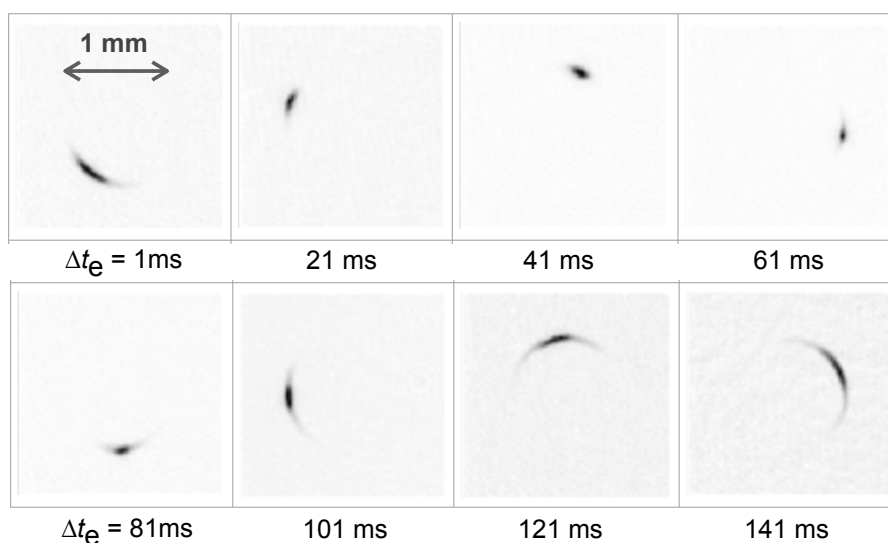


Figure 7.7: BEC focusing in the ring waveguide. Absorption images of the atom clouds after a focusing pulse is applied, for different waveguide expansion times. The images were taken after a time-of-flight of 5.3 ms.

We define the aspect ratio ( $\lambda$ ) in the ring waveguide as the ratio of radial size ( $l_\rho$ ) divided by the azimuthal size ( $l_\phi$ ),  $\lambda = l_\rho/l_\phi$ . Fig. 7.8 shows the change in  $\lambda$  for the BEC and thermal cloud after a kick pulse.  $\lambda_{\text{BEC}}$  changes from 0.05 to 0.75, on the other hand, for the thermal cloud,  $\lambda_{\text{th}}$  changes from 0.21 to 0.6. We have not measured any atom number loss during the focusing sequence, the calculated three-body loss rate is very low considering our experiment timescale<sup>1</sup>. We again observe a change in cloud radius as it travels around the waveguide after a kick pulse. In this case, R first increases up to the focusing time, by  $\sim 25\%$  and then drops to the steady value, likely due to any radial misalignment of the cloud and lens potential minimum.

In summary, I have shown matterwave optics with BECs and ultracold thermal atoms propagating freely in a ring waveguide. I achieved a final kinetic temperature of  $1.6^{+0.2}_{-0.2}$  nK for the BEC and  $16^{+2}_{-1}$  nK for the thermal atoms, respectively. The atomic

<sup>1</sup>For  $10^3$  BEC, three-body loss rate of the order of  $2 \times 10^{-3} \text{ s}^{-1}$ . The radial, axial and the azimuthal trapping frequencies are 85.3 Hz, 46.2 Hz and 9.2 Hz, respectively.



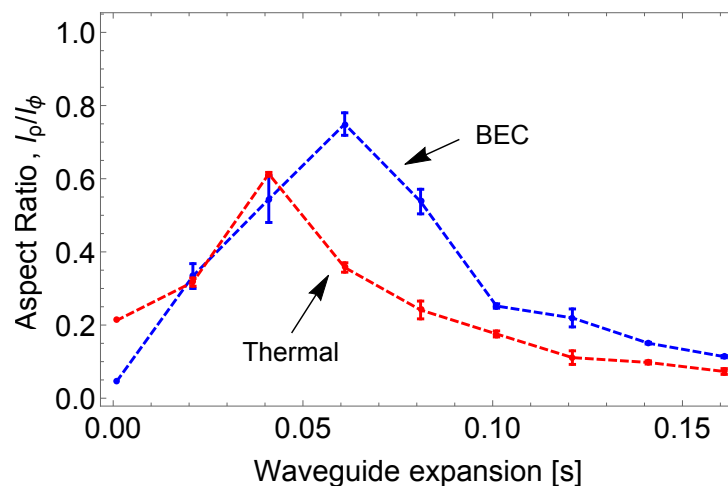


Figure 7.8: Aspect ratio of the BEC and thermal atoms as a function of the waveguide expansion time, after the focusing pulse is switched off. The red and blue dashed lines are shown as a guide.

cloud propagates for up to six round trips and the final BEC spread is only one-third and thermal atoms fill one-fifth of the ring waveguide. In addition, I studied focusing of BECs moving at similar speeds as in the collimation case. A factor of 15 increase in the aspect ratio was achieved for the BEC and a factor of 3 for the thermal cloud, respectively. The atom optics results presented will be crucial in drastically improving the interaction times and the interference fringe contrast in trapped atom interferometry applications.

### Angular speed after the lens

Fig. 7.9 shows the angular position of BECs after the collimation delta-kick pulse. We stop the acceleration at  $2\pi \times 10$  rad/s and then launch the atoms into a horizontal ring waveguide. The red dashed line is a straight line fit to the data points, and we find an angular speed of  $2\pi \times 10.07$  (1) rad/s. For each waveguide expansion, there are few data points and the error in the angular position is same as of the plotted point size. The shot to shot angular position stability of the cloud in the ring waveguide is 27 mrad (not visible on the scale of the Fig. 7.9).

## 7.6 A beam splitter for BECs in the ring waveguide

I realized a beam splitter for the BECs trapped in a flat ring waveguide. The beam splitter is a single beam dipole which is vertically overlapped with the ring waveguide (see

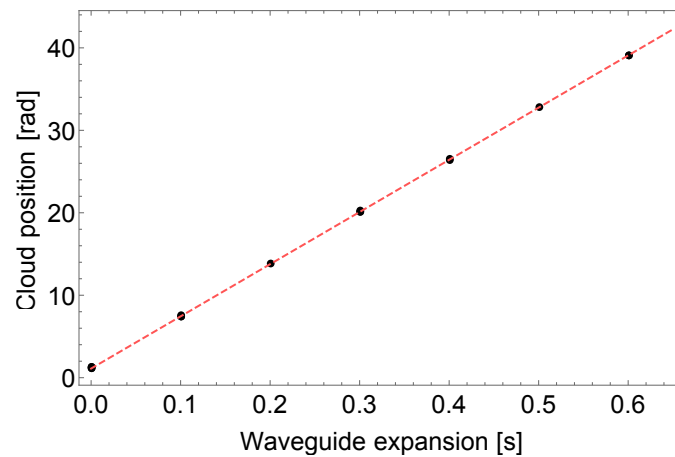


Figure 7.9: Angular position of the atom cloud against the waveguide expansion time after switching off the delta-kick pulse. The error in the position is of the order of the point size.

scheme in Fig. 7.10). After evaporating the atomic ensemble down to the BEC in crossed-beam optical dipole traps, a ring waveguide potential is switched on. Next, the power in one of the dipole beams is ramped down to zero and the BECs are held in a combined potential of ring waveguide and the single beam dipole. Finally, to split the BEC, the ring potential is moved slowly in the  $xy$  plane by the use of compensation coils. The displacement of the ring waveguide is orthogonal to the dipole beam longitudinal axis. In order to tune the relative population in the two potential wells, the ring potential was tilted using the horizontal ( $x$ ) modulation field. Fig. 7.11 shows absorption images of

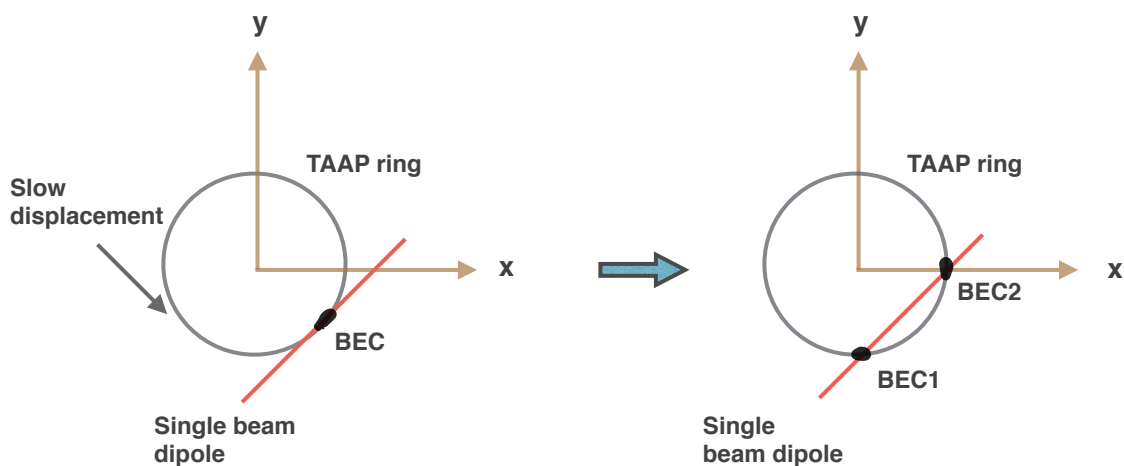


Figure 7.10: A cartoon depicting the splitting of a BEC in the ring waveguide, using a single beam dipole as a beam splitter.

BECs after they are split into two by moving ring waveguide center towards the dipole beam. The experiment begins by producing  $2.5 \times 10^5$  BEC in the crossed dipole trap. The

ring waveguide potential is then turned on, magnetic gradient at 70 Gpcm, 2.55 MHz rf-field with Rabi frequency  $\approx 357$  KHz, and 1.4 G vertical modulation field oscillating at 5.02 kHz. The ring and the crossed dipole trap are overlapped by ramping the magnetic gradient from 2 Gpcm to 70 Gpcm in 100 ms. Next, one of the dipole beams is switched off completely in 150 ms, now the atoms are held in a combined trap of ring and a single beam dipole. To split the BEC, the ring waveguide is displaced by about  $200 \mu\text{m}$  in 200 ms, using the  $xy$  compensation coils (in the same setting the compensation coils as we use to load the ring from the crossed dipole). The atoms are absorption imaged after a time-of-flight of 15.3 ms using the vertical imaging. The population in the two wells was precisely tuned by using a  $x$  modulation field (45 deg out of phase with respect to the  $z$  modulation), which was switched on together with the ring potential.

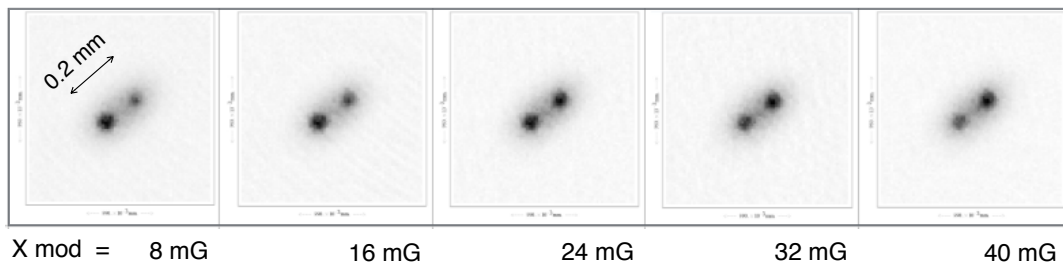


Figure 7.11: Absorption images of split BECs in a combined potential of ring waveguide and a single beam dipole, images were taken after a time-of-flight of 15 ms. The relative population in the two wells were tuned by tilting the ring potential.

## Chapter 8

# Conclusions and future work

In summary, I presented coherent manipulation of BECs and ultracold thermal atoms in TAAP ring traps and waveguides. The key results of my dissertation are summarized below, related to the guided matterwave interferometry schemes and other interesting findings.

### State-dependent manipulation in ring traps

For the guided atom interferometry using  $^{87}\text{Rb}$  clock states in tilted ring traps, I demonstrated state dependent manipulation of two spin states in a ring trap, necessary in a clock type scheme. To manipulate the states independently, the ring potential was tilted from a combination of a radial audio-frequency and RF fields. The atoms in two spin states were trapped in two arms of the ring and moved arbitrarily. The radius of the ring trap was varied from  $400\ \mu\text{m}$  to  $1.3\ \text{mm}$ , directly proportional to the sensitivity of atom interferometer. In order to perform the full interferometric sequence, coherent splitting and recombination of atom cloud is required using two-photon (RF/microwave)  $\pi/2$  pulses. These pulses act as a mirror and beam splitter for the matterwaves. To that extent, I contributed to the project – spectroscopy of the atomic energy levels in a RF dressed trap, where coherent population transfer among dressed Zeeman sublevels at the two hyperfine manifolds was achieved.

### Decoherence-free hypersonic transport of BECs

To achieve high interferometric sensitivities, it becomes necessary to either increase the closed-loop area or atoms go many round trips before the population in two states is measured. For the latter case, I demonstrated macroscopic decoherence-free transport

of BECs and ultracold thermal atoms at hypersonic speeds in a neutral-atom accelerator ring trap. BECs and ultracold atoms were transported in a 1 mm diameter ring trap for distances of up to 40 cm. BECs travelled at speeds of 16 times their Landau critical velocity with no extra heating when compared to the static trap. This became possible due to the extreme smoothness of TAAP rings, and the use of optimal control in designing the trap trajectory. With our current measurement sensitivity, the roughness in our millimeter-sized TAAP rings were found to be below 200 pK. I presented generation of ultracold atomic clouds with an angular momentum of more than  $40000 \hbar$  per atom. This is a demonstration of a novel route to prepare and manipulate high angular momentum states of ultracold Bosons.

## Atom optics with BECs in ring waveguides

To perform guided atom interferometry using atomic momentum states, it is necessary to keep the atomic wave packets compact as they propagate around the waveguide. After splitting an ultracold atom cloud using Bragg beam splitter, two clouds propagate freely in the opposite arms of the ring waveguide. The moving clouds expand along the azimuthal direction due to their finite momentum spread and eventually fill the whole waveguide. The expansion of the atomic wave packets in a curved ring potential make it difficult to apply a well-controlled Bragg pulse. Furthermore, the cloud expansion is detrimental to the interference fringe contrast and limits the number of round trips before read-out. This presents a serious limitation on the desired interferometric sensitivity. Therefore, it becomes necessary to control the expansion of the ultracold atoms in the ring. I implemented a novel way to perform atom optics with BECs and ultracold thermal atoms moving freely in the ring waveguide. BECs were accelerated in a tilted ring trap and then launched into a horizontal ring waveguide. After a long free expansion in the waveguide, an azimuthal lens (tilted waveguide) was switched on for a very short duration to either collimate or focus the atomic beam. The effective BEC temperature was reduced by a factor of 30, down to a few nanokelvin. BECs travelled for up to macroscopic distances of 20 mm and filled only one-third of the ring waveguide. I also studied focusing of travelling BECs in a ring waveguide, using a stronger lens than used in the collimation case. The collimation results presented will offer interferometer interrogation times of up to seconds. A focusing pulse will be applied near the end of the experimental sequence to enhance the interference fringe contrast.

## Upcoming studies

### Bragg guided-atom interferometry

In the next step, a Bragg beam splitter will be implemented to perform the full interferometric sequence in the ring waveguide. After loading an ultracold atomic cloud in a tilted ring trap, a Bragg beam splitter will be applied to create a coherent superposition of momentum states. At the same time, the tilt of the ring will be removed turning the potential into a flat ring waveguide. The beam splitter splits the wave-packet into two, and they are kicked in the opposite directions. The two wave packets travel with a speed given by the two-photon recoil momentum. After travelling for half the perimeter of the waveguide, another Bragg pulse will be shone to swap the population between the two states and thus cancelling any systemic unwanted phase shift. An interference fringe will be displayed when the two wave packets overlap. The crucial points of the experiment will be, 1) making sure that the atom cloud is small along the azimuthal direction and the ring curvature does not lower the Bragg diffraction efficiency, and 2) the expansion of the cloud does not cause significant reduction in the interference fringe contrast. The first point will be addressed by starting with atoms in a tilted ring (tight azimuthal confinement) and the second by using the delta-kick cooling technique after the atoms travel for quarter of the ring waveguide. Other effects will be systematically investigated as the study proceeds.

### Engineered defects in TAAP ring waveguides

We plan to engineer defects in our extremely smooth ring waveguides and traps, to study their effect on the coherent transport of matterwaves travelling at very high speeds, from subsonic to hypersonic. This will be implemented using an optical dipole potential, a far-off-resonant red-detuned dipole beam will be overlapped with the ring potential to create a potential dip in the waveguide. By tuning the size and power of the beam defect width and height can be varied, respectively. We will study the excitation generated within the matterwaves when they pass through such defects. We will also change the defect parameters, each defect will be looked at for a very broad range of speeds. This investigation will provide the much desired information to the atom-waveguide engineering community: the minimum amplitude of the defect/corrugation/roughness/perturbation present in an atom-waveguide potential to blow up (decohere) the travelling matterwaves. Also, we will be able to probe the superfluid flow much above the critical velocity.

# Bibliography

- [1] O. R. Frisch. . *Z. Phys.*, 86(42), 1933.
- [2] A. Ashkin. Acceleration and trapping of particles by radiation pressure. *Phys. Rev. Lett.*, 24:156–159, Jan 1970.
- [3] A. Ashkin. Atomic-beam deflection by resonance-radiation pressure. *Phys. Rev. Lett.*, 25:1321–1324, Nov 1970.
- [4] T W Hänsch and A L Schawlow. Cooling of gases by laser radiation. *Optics Communications*, 13(1):68–69, 1975.
- [5] A. Ashkin. Trapping of atoms by resonance radiation pressure. *Phys. Rev. Lett.*, 40:729–732, Mar 1978.
- [6] William D. Phillips and Harold Metcalf. Laser deceleration of an atomic beam. *Phys. Rev. Lett.*, 48:596–599, Mar 1982.
- [7] Steven Chu, L. Hollberg, J. E. Bjorkholm, Alex Cable, and A. Ashkin. Three-dimensional viscous confinement and cooling of atoms by resonance radiation pressure. *Phys. Rev. Lett.*, 55:48–51, Jul 1985.
- [8] Paul D. Lett, Richard N. Watts, Christoph I. Westbrook, William D. Phillips, Phillip L. Gould, and Harold J. Metcalf. Observation of atoms laser cooled below the doppler limit. *Phys. Rev. Lett.*, 61:169–172, Jul 1988.
- [9] J Dalibard and C Cohen-Tannoudji. Laser cooling below the Doppler limit by polarization gradients: simple theoretical models. *J. Opt. Soc. Am. B*, 6(11):2023–2045, November 1989.
- [10] C V Heer. Feasibility of Containment of Quantum Magnetic Dipoles. *Review of Scientific Instruments*, 34(5):532–537, 1963.
- [11] Alan L. Migdall, John V. Prodan, William D. Phillips, Thomas H. Bergeman, and Harold J. Metcalf. First observation of magnetically trapped neutral atoms. *Phys. Rev. Lett.*, 54:2596–2599, Jun 1985.

- [12] E. L. Raab, M. Prentiss, Alex Cable, Steven Chu, and D. E. Pritchard. Trapping of neutral sodium atoms with radiation pressure. *Phys. Rev. Lett.*, 59:2631–2634, Dec 1987.
- [13] Wolfgang Ketterle, Kendall B. Davis, Michael A. Joffe, Alex Martin, and David E. Pritchard. High densities of cold atoms in a dark spontaneous-force optical trap. *Phys. Rev. Lett.*, 70:2253–2256, Apr 1993.
- [14] Harald F. Hess. Evaporative cooling of magnetically trapped and compressed spin-polarized hydrogen. *Phys. Rev. B*, 34:3476–3479, Sep 1986.
- [15] Wolfgang Petrich, Michael H. Anderson, Jason R. Ensher, and Eric A. Cornell. Stable, tightly confining magnetic trap for evaporative cooling of neutral atoms. *Phys. Rev. Lett.*, 74:3352–3355, Apr 1995.
- [16] M H Anderson, J R Ensher, M R Matthews, C E Wieman, and E A Cornell. Observation of Bose-Einstein Condensation in a Dilute Atomic Vapor. *Science*, 269(5221):198–201, 1995.
- [17] K. B. Davis, M. O. Mewes, M. R. Andrews, N. J. van Druten, D. S. Durfee, D. M. Kurn, and W. Ketterle. Bose-einstein condensation in a gas of sodium atoms. *Phys. Rev. Lett.*, 75:3969–3973, Nov 1995.
- [18] C Ryu, M F Andersen, P Cladé, Vasant Natarajan, K Helmerson, and W D Phillips. Observation of Persistent Flow of a Bose-Einstein Condensate in a Toroidal Trap. *Phys. Rev. Lett.*, 99(26):260401, December 2007.
- [19] Immanuel Bloch, Jean Dalibard, and Sylvain Nascimbène. Quantum simulations with ultracold quantum gases. *Nature Physics*, 8:267, April 2012.
- [20] Alexander D. Cronin, Jörg Schmiedmayer, and David E. Pritchard. Optics and interferometry with atoms and molecules. *Rev. Mod. Phys.*, 81:1051–1129, Jul 2009.
- [21] S L Campbell, R B Hutson, G E Marti, A Goban, N Darkwah Oppong, R L McNally, L Sonderhouse, J M Robinson, W Zhang, B J Bloom, and J Ye. A Fermi-degenerate three-dimensional optical lattice clock. *Science*, 358(6359):90–94, 2017.
- [22] B J Bloom, T L Nicholson, J R Williams, S L Campbell, M Bishof, X Zhang, W Zhang, S L Bromley, and J Ye. An optical lattice clock with accuracy and stability at the  $10^{-18}$  level. *Nature*, 506:71, January 2014.
- [23] G D McDonald, C C N Kuhn, S Bennetts, J E Debs, K S Hardman, M Johnsson, J D Close, and N P Robins.  $\hbar k$  momentum separation with Bloch oscillations in an optically guided atom interferometer. *Phys. Rev. A*, 88(5):53620, November 2013.



- [24] Erika Andersson, Tommaso Calarco, Ron Folman, Mauritz Andersson, Björn Hessmo, and Jörg Schmiedmayer. Multimode interferometer for guided matter waves. *Phys. Rev. Lett.*, 88:100401, Feb 2002.
- [25] T L Gustavson, A Landragin, and M A Kasevich. Rotation sensing with a dual atom-interferometer Sagnac gyroscope. *Classical and Quantum Gravity*, 17(12):2385, 2000.
- [26] R Geiger, V Ménot, G Stern, N Zahzam, P Cheinet, B Battelier, A Villing, F Moron, M Lours, Y Bidet, A Bresson, A Landragin, and P Bouyer. Detecting inertial effects with airborne matter-wave interferometry. *Nature Communications*, 2:474, September 2011.
- [27] T Farah, C Guerlin, A Landragin, Ph. Bouyer, S Gaffet, F Pereira Dos Santos, and S Merlet. Underground operation at best sensitivity of the mobile LNE-SYRTE cold atom gravimeter. *Gyroscopy and Navigation*, 5(4):266–274, October 2014.
- [28] Brett Altschul, Quentin G Bailey, Luc Blanchet, Kai Bongs, Philippe Bouyer, Luigi Cacciapuoti, Salvatore Capozziello, Naceur Gaaloul, Domenico Giulini, Jonas Hartwig, Luciano Iess, Philippe Jetzer, Arnaud Landragin, Ernst Rasel, Serge Reynaud, Stephan Schiller, Christian Schubert, Fiodor Sorrentino, Uwe Sterr, Jay D Tasson, Guglielmo M Tino, Philip Tuckey, and Peter Wolf. Quantum tests of the Einstein Equivalence Principle with the STE-QUEST space mission. *Advances in Space Research*, 55(1):501–524, 2015.
- [29] Savas Dimopoulos, Peter W Graham, Jason M Hogan, Mark A Kasevich, and Surjeet Rajendran. Atomic gravitational wave interferometric sensor. *Phys. Rev. D*, 78(12):122002, December 2008.
- [30] G Rosi, F Sorrentino, L Cacciapuoti, M Prevedelli, and G M Tino. Precision measurement of the Newtonian gravitational constant using cold atoms. *Nature*, 510:518, June 2014.
- [31] Rym Bouchendira, Pierre Cladé, Saïda Guellati-Khélifa, François Nez, and François Biraben. New determination of the fine structure constant and test of the quantum electrodynamics. *Phys. Rev. Lett.*, 106:080801, Feb 2011.
- [32] Andreas Wicht, Joel M Hensley, Edina Sarajlic, and Steven Chu. A Preliminary Measurement of the Fine Structure Constant Based on Atom Interferometry. *Physica Scripta*, 2002(T102):82, 2002.
- [33] Alex A Zozulya and Dana Z Anderson. Principles of an atomtronic battery. *Phys. Rev. A*, 88(4):43641, October 2013.

- 
- [34] Seth C Caliga, Cameron J E Straatsma, and Dana Z Anderson. Experimental demonstration of an atomtronic battery. *New Journal of Physics*, 19(1):13036, 2017.
- [35] Seth C Caliga, Cameron J E Straatsma, and Dana Z Anderson. Transport dynamics of ultracold atoms in a triple-well transistor-like potential. *New Journal of Physics*, 18(2):25010, 2016.
- [36] K C Wright, R B Blakestad, C J Lobb, W D Phillips, and G K Campbell. Driving Phase Slips in a Superfluid Atom Circuit with a Rotating Weak Link. *Phys. Rev. Lett.*, 110(2):25302, January 2013.
- [37] Amy C Mathey and L Mathey. Realizing and optimizing an atomtronic SQUID. *New Journal of Physics*, 18(5):55016, 2016.
- [38] K Bongs, S Burger, S Dettmer, D Hellweg, J Arlt, W Ertmer, and K Sengstock. Waveguide for Bose-Einstein condensates. *Phys. Rev. A*, 63(3):31602, February 2001.
- [39] W Guerin, J.-F. Riou, J P Gaebler, V Josse, P Bouyer, and A Aspect. Guided Quasi-continuous Atom Laser. *Phys. Rev. Lett.*, 97(20):200402, November 2006.
- [40] T L Gustavson, A P Chikkatur, A E Leanhardt, A Görlitz, S Gupta, D E Pritchard, and W Ketterle. Transport of Bose-Einstein Condensates with Optical Tweezers. *Phys. Rev. Lett.*, 88(2):20401, December 2001.
- [41] M J Renn, D Montgomery, O Vdovin, D Z Anderson, C E Wieman, and E A Cornell. Laser-Guided Atoms in Hollow-Core Optical Fibers. *Phys. Rev. Lett.*, 75(18):3253–3256, October 1995.
- [42] T Takekoshi and R J Knize. Optical Guiding of Atoms through a Hollow-Core Photonic Band-Gap Fiber. *Phys. Rev. Lett.*, 98(21):210404, May 2007.
- [43] M Key, I G Hughes, W Rooijackers, B E Sauer, E A Hinds, D J Richardson, and P G Kazansky. Propagation of Cold Atoms along a Miniature Magnetic Guide. *Phys. Rev. Lett.*, 84(7):1371–1373, February 2000.
- [44] N. Dekker, C. Lee, V. Lorent, J. Thywissen, S. Smith, M. Drndić, R. Westervelt, and M. Prentiss. Guiding Neutral Atoms on a Chip. *Physical Review Letters*, 84(c):1124–1127, 2000.
- [45] A. E. Leanhardt, A. P. Chikkatur, D. Kielpinski, Y. Shin, T. L. Gustavson, W. Ketterle, and D. E. Pritchard. Propagation of bose-einstein condensates in a magnetic waveguide. *Physical Review Letters*, 89(4):040401, 3 2002.

- [46] Y. J. Wang, D. Z. Anderson, V. M. Bright, E. A. Cornell, Q. Diot, T. Kishimoto, M. Prentiss, R. A. Saravanan, S. R. Segal, and S. J. Wu. Atom michelson interferometer on a chip using a bose-einstein condensate. *Physical Review Letters*, 94:090405, 3 2005.
- [47] Jozsef Fortagh, Sebastian Kraft, Andreas Gunther, Christian Truck, Philipp Wicke, and Claus Zimmermann. Perspectives of ultracold atoms trapped in magnetic micro potentials. *Optics Communications*, 243(1-6):45–56, Dec 2004.
- [48] Xi Chen, E Torrontegui, Dionisis Stefanatos, Jr-Shin Li, and J G Muga. Optimal trajectories for efficient atomic transport without final excitation. *Phys. Rev. A*, 84(4):43415, October 2011.
- [49] G De Chiara, T Calarco, M Anderlini, S Montangero, P J Lee, B L Brown, W D Phillips, and J V Porto. Optimal control of atom transport for quantum gates in optical lattices. *Phys. Rev. A*, 77(5):52333, May 2008.
- [50] E Torrontegui, Xi Chen, M Modugno, S Schmidt, A Ruschhaupt, and J G Muga. Fast transport of Bose–Einstein condensates. *New Journal of Physics*, 14(1):13031, 2012.
- [51] Sierk Pötting, Marcus Cramer, Christian H Schwalb, Han Pu, and Pierre Meystre. Coherent acceleration of Bose-Einstein condensates. *Phys. Rev. A*, 64(2):23604, July 2001.
- [52] O Dutta, M Jääskeläinen, and P Meystre. Single-mode acceleration of matter waves in circular waveguides. *Phys. Rev. A*, 74(2):23609, August 2006.
- [53] Igor Lesanovsky and Wolf von Klitzing. Time-Averaged Adiabatic Potentials: Versatile Matter-Wave Guides and Atom Traps. *Phys. Rev. Lett.*, 99(8):83001, August 2007.
- [54] T Müller, B Zhang, R Fermani, K S Chan, M J Lim, and R Dumke. Programmable trap geometries with superconducting atom chips. *Phys. Rev. A*, 81(5):53624, May 2010.
- [55] Cecilia Muldoon, Lukas Brandt, Jian Dong, Dustin Stuart, Edouard Brainis, Matthew Himsworth, and Axel Kuhn. Control and manipulation of cold atoms in optical tweezers. *New Journal of Physics*, 14(7), 2012.
- [56] C. Ryu and M. G. Boshier. Integrated coherent matter wave circuits. *New Journal of Physics*, 17(9), 2015.

- [57] Alan Lenef, Troy D Hammond, Edward T Smith, Michael S Chapman, Richard A Rubenstein, and David E Pritchard. Rotation Sensing with an Atom Interferometer. *Phys. Rev. Lett.*, 78(5):760–763, February 1997.
- [58] Stephen Eckel, Jeffrey G. Lee, Fred Jendrzejewski, Noel Murray, Charles W. Clark, Christopher J. Lobb, William D. Phillips, Mark Edwards, and Gretchen K. Campbell. Hysteresis in a quantized superfluid /‘atomtronic/’ circuit. *Nature*, 506(7487):200–203, 02 2014.
- [59] S. Gupta, K. W. Murch, K. L. Moore, T. P. Purdy, and D. M. Stamper-Kurn. Bose-einstein condensation in a circular waveguide. *Physical Review Letters*, 95(14):143201, 9 2005.
- [60] A S Arnold, C S Garvie, and E Riis. Large magnetic storage ring for Bose-Einstein condensates. *Phys. Rev. A*, 73(4):41606, April 2006.
- [61] P Navez, S Pandey, H Mas, K Poullos, T Fernholz, and W von Klitzing. Matter-wave interferometers using TAAP rings. *New Journal of Physics*, 18(7):75014, 2016.
- [62] Thomas A Bell, Jake A P Glidden, Leif Humbert, Michael W J Bromley, Simon A Haine, Matthew J Davis, Tyler W Neely, Mark A Baker, and Halina Rubinsztein-Dunlop. Bose–Einstein condensation in large time-averaged optical ring potentials. *New Journal of Physics*, 18(3):35003, 2016.
- [63] A Turpin, J Polo, Yu. V Loiko, J Küber, F Schmaltz, T K Kalkandjiev, V Ahufinger, G Birkl, and J Mompart. Blue-detuned optical ring trap for Bose-Einstein condensates based on conical refraction. *Opt. Express*, 23(2):1638–1650, January 2015.
- [64] Daniel A Steck. Rubidium 87 D Line Data (<http://steck.us/alkalidata>), 2001.
- [65] Walther Gerlach and Otto Stern. Der experimentelle Nachweis der Richtungsquantelung im Magnetfeld. *Zeitschrift für Physik*, 9(1):349–352, December 1922.
- [66] G. Breit and I. I. Rabi. Measurement of nuclear spin. *Phys. Rev.*, 38:2082–2083, Dec 1931.
- [67] Ettore Majorana. Atomi orientati in campo magnetico variabile. *Il Nuovo Cimento (1924-1942)*, 9(2):43–50, February 1932.
- [68] Magnus Haw, Nathan Evetts, Will Gunton, Janelle Van Dongen, James L Booth, and Kirk W Madison. Magneto-optical trap loading rate dependence on trap depth and vapor density. *J. Opt. Soc. Am. B*, 29(3):475–483, March 2012.

- [69] C. Monroe, W. Swann, H. Robinson, and C. Wieman. Very cold trapped atoms in a vapor cell. *Phys. Rev. Lett.*, 65:1571–1574, Sep 1990.
- [70] Rudolf Grimm, Matthias Weidemüller, and Yurii B Ovchinnikov. Optical Dipole Traps for Neutral Atoms. volume 42 of *Advances In Atomic, Molecular, and Optical Physics*, pages 95–170. Academic Press, 2000.
- [71] Y.-J. Lin, A. R. Perry, R. L. Compton, I. B. Spielman, and J. V. Porto. Rapid production of  $^{87}\text{Rb}$  bose-einstein condensates in a combined magnetic and optical potential. *Phys. Rev. A*, 79:063631, Jun 2009.
- [72] E Hodby, G Hechenblaikner, O M Maragò, J Arlt, S Hopkins, and C J Foot. Bose-Einstein condensation in a stiff TOP trap with adjustable geometry. *Journal of Physics B: Atomic, Molecular and Optical Physics*, 33(19):4087, 2000.
- [73] Luigi Amico, Gerhard Birkel, Malcolm Boshier, and Leong-Chuan Kwek. Focus on atomtronics-enabled quantum technologies. *New Journal of Physics*, 19(2):20201, 2017.
- [74] G A Sinuco-León and B M Garraway. Addressed qubit manipulation in radio-frequency dressed lattices. *New Journal of Physics*, 18(3):35009, March 2016.
- [75] Lev Davidovich Zener. *Phys. Z. Sowjetunion*, 2:46–51, 1932.
- [76] Clarence Zener and Ralph Howard Fowler. Non-adiabatic crossing of energy levels. *Proceedings of the Royal Society of London. Series A, Containing Papers of a Mathematical and Physical Character*, 137(833):696–702, 1932.
- [77] N. V. Vitanov and K.-A. Suominen. Time-dependent control of ultracold atoms in magnetic traps. *Phys. Rev. A*, 56:R4377–R4380, Dec 1997.
- [78] Claude Cohen-Tannoudji and David Guéry-Odelin. *Advances in Atomic Physics*. WORLD SCIENTIFIC, 2011.
- [79] Ph W Courteille, B Deh, J Fortágh, A Günther, S Kraft, C Marzok, S Slama, and C Zimmermann. Highly versatile atomic micro traps generated by multifrequency magnetic field modulation. *Journal of Physics B: Atomic, Molecular and Optical Physics*, 39(5):1055, 2006.
- [80] T Schumm, S Hofferberth, L M Andersson, S Wildermuth, S Groth, I Bar-Joseph, J Schmiedmayer, and P Krüger. Matter-wave interferometry in a double well on an atom chip. *Nature Physics*, 1:57, September 2005.

- [81] Kathryn A. Burrows, H el ene Perrin, and Barry M. Garraway. Nonadiabatic losses from radio-frequency-dressed cold-atom traps: Beyond the Landau-Zener model. *Phys. Rev. A*, 96:023429, Aug 2017.
- [82] Vanderlei Bagnato, David E. Pritchard, and Daniel Kleppner. Bose-Einstein condensation in an external potential. *Phys. Rev. A*, 35:4354–4358, May 1987.
- [83] Wesley E Brittin. Statistical Mechanics. Kerson Huang. Wiley, New York, 1963. xiv + 470 pp. Illus. 10.75. *Science*, 142(3592):568, 1963.
- [84] E. G. M. van Kempen, S. J. J. M. F. Kokkelmans, D. J. Heinzen, and B. J. Verhaar. Interisotope determination of ultracold rubidium interactions from three high-precision experiments. *Phys. Rev. Lett.*, 88:093201, Feb 2002.
- [85] J. L. Roberts, N. R. Claussen, James P. Burke, Chris H. Greene, E. A. Cornell, and C. E. Wieman. Resonant magnetic field control of elastic scattering in cold  $^{85}\text{Rb}$ . *Phys. Rev. Lett.*, 81:5109–5112, Dec 1998.
- [86] N. N. Bogolyubov. On the theory of superfluidity. *J. Phys.(USSR)*, 11:23–32, 1947. [Izv. Akad. Nauk Ser. Fiz.11,77(1947)].
- [87] M. Pappa. Imaging Bose-Einstein condensates at ultra-low atom numbers and time averaged adiabatic potentials. *PhD Thesis, University of Crete*, 2011.
- [88] Daniel Sahagun, Vasiliki Bolpasi, and Wolf von Klitzing. A simple and highly reliable laser system with microwave generated repumping light for cold atom experiments. *Optics Communications*, 290:110 – 114, 2013.
- [89] L. E. Erickson and A. Szabo. Spectral narrowing of dye laser output by injection of monochromatic radiation into the laser cavity. *Applied Physics Letters*, 18(10):433–435, 1971.
- [90] G. M. Kavoulakis and C. J. Pethick. Quasi-one-dimensional character of sound propagation in elongated Bose-Einstein condensed clouds. *Phys. Rev. A*, 58:1563–1566, Aug 1998.
- [91] J. H. M uller, O. Morsch, D. Ciampini, M. Anderlini, R. Mannella, and E. Arimondo. Atomic micromotion and geometric forces in a triaxial magnetic trap. *Phys. Rev. Lett.*, 85:4454–4457, Nov 2000.
- [92] O. Carnal and J. Mlynek. Young’s double-slit experiment with atoms: A simple atom interferometer. *Phys. Rev. Lett.*, 66:2689–2692, May 1991.
- [93] David W. Keith, Christopher R. Ekstrom, Quentin A. Turchette, and David E. Pritchard. An interferometer for atoms. *Phys. Rev. Lett.*, 66:2693–2696, May 1991.

- [94] C S Adams, M Sigel, and J Mlynek. Atom optics. *Physics Reports*, 240(3):143–210, 1994.
- [95] Mark Kasevich and Steven Chu. Atomic interferometry using stimulated raman transitions. *Phys. Rev. Lett.*, 67:181–184, Jul 1991.
- [96] F. Riehle, Th. Kisters, A. Witte, J. Helmcke, and Ch. J. Bordé. Optical ramsey spectroscopy in a rotating frame: Sagnac effect in a matter-wave interferometer. *Phys. Rev. Lett.*, 67:177–180, Jul 1991.
- [97] David M. Giltner, Roger W. McGowan, and Siu Au Lee. Atom interferometer based on bragg scattering from standing light waves. *Phys. Rev. Lett.*, 75:2638–2641, Oct 1995.
- [98] Saijun Wu, Edward Su, and Mara Prentiss. Demonstration of an area-enclosing guided-atom interferometer for rotation sensing. *Phys. Rev. Lett.*, 99:173201, Oct 2007.
- [99] T. L. Gustavson, P. Bouyer, and M. A. Kasevich. Precision rotation measurements with an atom interferometer gyroscope. *Phys. Rev. Lett.*, 78:2046–2049, Mar 1997.
- [100] B E Sherlock, M Gildemeister, E Owen, E Nugent, and C J Foot. Time-averaged adiabatic ring potential for ultracold atoms. *Phys. Rev. A*, 83(4):43408, April 2011.
- [101] Qing-Qing Hu, Yu-Kun Luo, Ai-Ai Jia, Chun-Hua Wei, Shu-Hua Yan, and Jun Yang. Scheme for suppressing atom expansion induced contrast loss in atom interferometers. *Optics Communications*, 390:111–116, 2017.
- [102] Hubert Ammann and Nelson Christensen. Delta kick cooling: A new method for cooling atoms. *Phys. Rev. Lett.*, 78:2088–2091, Mar 1997.
- [103] S Chu, J E Bjorkholm, A Ashkin, J P Gordon, and L W Hollberg. Proposal for optically cooling atoms to temperatures of the order of  $10^{-6}$  K. *Opt. Lett.*, 11(2):73–75, February 1986.
- [104] Tim Kovachy, Jason M. Hogan, Alex Sugarbaker, Susannah M. Dickerson, Christine A. Donnelly, Chris Overstreet, and Mark A. Kasevich. Matter wave lensing to picokelvin temperatures. *Phys. Rev. Lett.*, 114:143004, Apr 2015.
- [105] H. Müntinga, H. Ahlers, M. Krutzik, A. Wenzlawski, S. Arnold, D. Becker, K. Bongs, H. Dittus, H. Duncker, N. Gaaloul, C. Gherasim, E. Giese, C. Grzeschik, T. W. Hänsch, O. Hellmig, W. Herr, S. Herrmann, E. Kajari, S. Kleinert, C. Lämmerzahl, W. Lewoczko-Adamczyk, J. Malcolm, N. Meyer, R. Nolte, A. Peters, M. Popp, J. Reichel, A. Roura, J. Rudolph, M. Schiemangk, M. Schneider, S. T.

- Seidel, K. Sengstock, V. Tamma, T. Valenzuela, A. Vogel, R. Walser, T. Wendrich, P. Windpassinger, W. Zeller, T. van Zoest, W. Ertmer, W. P. Schleich, and E. M. Rasel. Interferometry with bose-einstein condensates in microgravity. *Phys. Rev. Lett.*, 110:093602, Feb 2013.
- [106] Susannah M. Dickerson, Jason M. Hogan, Alex Sugarbaker, David M. S. Johnson, and Mark A. Kasevich. Multiaxis inertial sensing with long-time point source atom interferometry. *Phys. Rev. Lett.*, 111:083001, Aug 2013.
- [107] Saurabh Pandey, Hector Mas, Giannis Drougakis, Premjith Thekkepatt, Vasiliki Bolpasi, Georgios Vasilakis, Konstantinos Poullos, and Wolf von Klitzing. Hypersonic Bose–Einstein condensates in accelerator rings. *Nature*, 2019.
- [108] Yu. Kagan, E. L. Surkov, and G. V. Shlyapnikov. Evolution of a bose gas in anisotropic time-dependent traps. *Phys. Rev. A*, 55:R18–R21, Jan 1997.
- [109] Y. Castin and R. Dum. Bose-einstein condensates in time dependent traps. *Phys. Rev. Lett.*, 77:5315–5319, Dec 1996.